2015

Radio frequency and capacitive sensors for dielectric characterization of low-conductivity media

Robert Thomas Sheldon
Iowa State University

Recommended Citation

Sheldon, Robert Thomas, "Radio frequency and capacitive sensors for dielectric characterization of low-conductivity media" (2015). *Graduate Theses and Dissertations*. 14862.
https://lib.dr.iastate.edu/etd/14862

Radio frequency and capacitive sensors for dielectric characterization of low-conductivity media

by

Robert T. Sheldon

A dissertation submitted to the graduate faculty
in partial fulfillment of the requirements for the degree of
DOCTOR OF PHILOSOPHY

Major: Electrical Engineering

Program of Study Committee:
Nicola Bowler, Major Professor
Degang Chen
Vinay Dayal
Stephen D. Holland
Jiming Song

Iowa State University
Ames, Iowa
2015

To my grandfather, Thomas F. Skoniecke, Sr.,

whose immense wisdom, kindness and generosity will never be forgotten.

TABLE OF CONTENTS

LIST OF TABLES

LIST OF FIGURES

ABSTRACT

Low-conductivity media are found in a vast number of applications, for example as electrical insulation or as the matrix polymer in high strength-to-weight ratio structural composites. In some applications, these materials are subjected to extreme environmental, thermal, and mechanical conditions that can affect the material's desired performance. In a more general sense, a medium may be comprised of one or more layers with unknown material properties that may affect the desired performance of the entire structure. It is often, therefore, of great import to be able to characterize the material properties of these media for the purpose of estimating their future performance in a certain application.

Low-conductivity media, or dielectrics, are poor electrical conductors and permit electromagnetic waves and static electric fields to pass through with minimal attenuation. The amount of electrical energy that may be stored (and lost) in these fields depends directly upon the material property, permittivity, which is generally complex, frequency-dependent and has a measurable effect on sensors designed to characterize dielectric media. In this work, two different types of dielectric sensors: radio frequency resonant antennas and lower-frequency (< 1 MHz) capacitive sensors, are designed for permittivity characterization in their respective frequency regimes.

In the first part of this work, the capability of characterizing multilayer dielectric structures is studied using a patch antenna, a type of antenna that is primarily designed for data communications in the microwave bands but has application in the field of nondestructive evaluation as well. Each configuration of a patch antenna has a single lowest resonant (dominant mode) frequency that is dependent upon the antenna's substrate material and geometry as well as the permittivity and geometry of exterior materials. Here, an extant forward model is validated using well-characterized microwave samples and a new method of resonant frequency and quality factor determination from measured data is presented. Excellent agreement between calculated and measured values of sensor resonant frequency was obtained for the samples studied. Agreement between calculated and measured quality factor was good in some cases but incurred the particular challenge of accurately quantifying multiple contributions to loss from the sensor structure itself, which at times dominates the contribution due to the sample material.

Two later chapters describe the development of capacitive sensors to quantify the low-frequency changes in material permittivity due to environmental aging mechanisms. One embodiment involves the application of coplanar concentric interdigital electrode sensors for the purpose of investigating polymer-matrix degradation in glass-fiber composites due to isothermal aging. Samples of bismaleimide-matrix glass-fiber composites were aged at several high temperatures to induce thermal degradation and capacitive sensors were used to measure the sensor capacitance and dissipation factor, parameters that are directly proportional to the real and imaginary components of complex permittivity, respectively. It was shown that real permittivity and dissipation factor decreased with increasing aging temperature, a trend that was common to both interdigital sensor measurements and standard parallel plate electrode measurements. The second piece of work involves the development of cylindrical interdigital electrode sensors to characterize complex permittivity changes in wire insulation due to aging-related degradation. The sensor was proven effective in detecting changes in irradiated nuclear power plant wiring insulation and in aircraft wiring insulation due to liquid chemical immersion. In all three cases, the results indicate a clear correlation of measured capacitance and dissipation factor with increased degradation.

CHAPTER 1. GENERAL INTRODUCTION

1.1 Research question

The research herein is divided into two parts, both with the common goal of characterizing low-conductivity media. The first part has the aim of designing and validating a potentially-portable nondestructive evaluation (NDE) sensor capable of measuring changes in complex permittivity in the X-band (8-12 GHz) of one layer of a single- or multilayer structure, provided all other permittivity and all layer thicknesses are known. The approach is to use a theoretical model, previously developed for standard communications bands (1-4 GHz) operation, to design and optimize a physical X-band operational sensor that can characterize low-conductivity media in its near field by measuring changes to its resonant frequency and quality factor.

The goal of the second part of this research is to design NDE capacitive sensors for effective detection and characterization of aging-related dielectric changes in the polymeric insulation of aviation and nuclear power plant control cables, as well as in low-conductivity structural polymer-matrix composites. In both types of applications here mentioned, the approach is to develop capacitive sensors that are capable of interrogating samples from their exterior surface and observe capacitance and dissipation factor changes as a function of thermal, radiation, and liquid chemical aging.

1.2 Literature survey

1.2.1 Radio frequency sensing

Radio frequencies are broadly defined as the range of oscillating electromagnetic signals between 3 kHz and 300 GHz. Within this range, many different applications are found. For example, amplitude-modulated (AM) radio stations in the Americas operate between generally

540 kHz and 1.710 MHz; frequency-modulated (FM) radio stations operate between 88 MHz and 108 MHz; cellular devices operate generally between 400 MHz and 2.6 GHz; microwave ovens operate at 2.45 GHz, close to a dielectric relaxation frequency of water; and radar systems operate throughout nearly the entire RF range. Radio frequencies are often divided into low frequencies and high frequencies, with the high frequencies known as microwaves, which generally fit the range between 300 MHz and 300 GHz. Low frequencies, below ∼1 MHz, say, are useful in general circuit design where connecting wires and traces are viewed as simple short circuits, spaces between them are viewed as open circuits, and Ohm's law relating resistance, voltage and current is well-obeyed, provided that the circuit traces and components are much smaller than the wavelength corresponding to the operating frequency of the circuit. For measuring sample permittivity, this makes measurements using resistor-inductor-capacitor (RLC) component resonance methods or devices such as parallel plate electrodes and inductance-capacitance-resistance (LCR) meters relatively simple, and can provide reliable dielectric spectroscopy data up to the 1 MHz range [1].

Where microwave frequencies are of interest in characterizing a dielectric sample, more complex methods must be utilized. This is due to the fact that the operating wavelengths involved are often on the same order as the physical dimensions of the cables, sensors and test-pieces. The cables and sensors begin to act more like transmission lines, generally at frequencies of about 100 MHz, where the composition of the conductors, insulation, and geometry all have an effect on the measurable quantities. Microwaves cannot simply be transmitted down a length of wire as a low-frequency current, their electromagnetic fields must be guided down a path with specific properties to reach a destination point with minimal attenuation.

One type of transmission line that can guide microwaves toward a sample for dielectric characterization is a waveguide. A standard waveguide is a hollow rectangular or coaxial cylindrical conductor with dimensions that permit specific frequencies to propagate from end to end unattenuated. In [2] a circular coaxial waveguide is used to hold a disc-shaped sample, shown in Figure 1.1, and a microwave pulse is transmitted toward the sample. The reflection and transmission coefficients are measured via a time-domain approach and the complex permittivity and permeability values of the sample are obtained. In [3], a flanged waveguide, Figure 1.2,

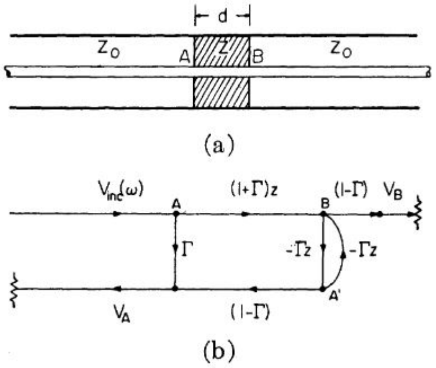

Figure 1.1 Cross-section view of a circular coaxial waveguide design (a) and signal flow graph (b) for complex dielectric and magnetic characterization. The sample, with thickness d is placed in the center of the waveguide, and the reflection and transmission coefficients are measured [2].

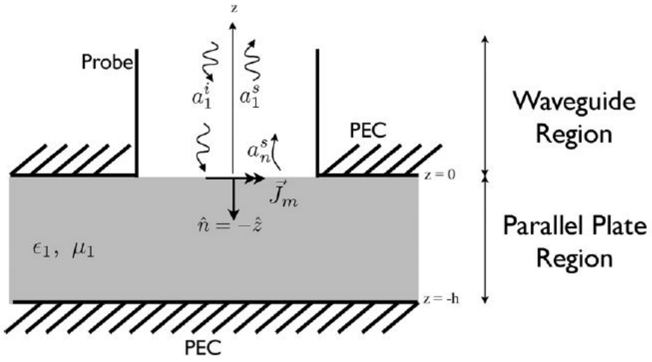

Figure 1.2 Cross-section view of a flanged waveguide in contact with a groundplane-backed dielectric sample. Measured reflection coefficients are used to determine the complex permittivity [3].

a waveguide with a flanged termination is used to make one-sided dielectric measurements of a dielectric sample backed by a perfect electrical conductor (PEC). This setup has the advantage of not requiring a piece of a sample to be specially shaped for insertion into a waveguide.

Another type of microwave dielectric characterization device is a cavity resonator. Similar to a waveguide, a cavity is designed to confine microwave energy with the exception that only standing waves rather than travelling waves are physically permitted. The wavelength of the standing wave is dependent upon the material within the cavity, thus the resonant frequency of the cavity is tuned by a sample material placed inside. In [4], a circular cavity is developed to

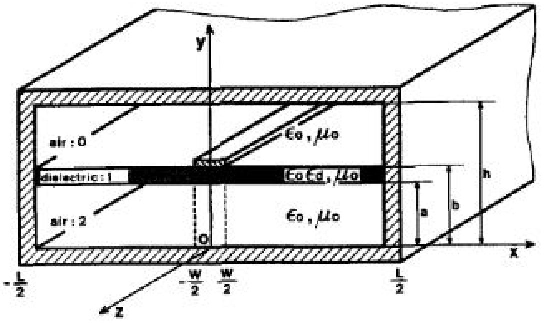

Figure 1.3 Isometric view of a microstrip transmission line protected in a shielded box. Above the strip is placed a dielectric sample (not pictured), which creates a measurable discontinuity in the characteristic impedance of the microstrip [6].

determine the complex permittivity of disc-shaped low-loss media samples by measuring both the resonant frequency and quality factor (Q-factor), which a measure of energy storage relative to energy loss. A cavity resonator for rod-shaped or liquid specimens was developed in [5] by use of perturbation theory with excellent agreement found between theory and experimental results.

Microstrip lines are another type of microwave transmission line designed to guide microwave energy between points of interest. Comprised of a conductive strip above a groundplane with a dielectric substrate supporting the strip, microwave energy travels partially through the substrate region between the strip and groundplane and partially in the air above the strip. In [6], a testing setup is developed that places a dielectric sample above the strip, creating a characteristic impedance discontinuity, which alters the reflection and transmission coefficients that yield the sample permittivity. Figure 1.3 shows the setup used in the microstrip characterization setup.

Finally, microwaves can be transmitted into free space by way of antennas, which can also be used to characterize dielectric samples. An antenna, put simply, is a structure that acts as a transition between a transmission line (such as a waveguide) and free space for directional or omnidirectional transmission. In [7], a pair of highly-directive horn antennas act as a transmitting and receiving antenna at 35 GHz, with either an isotropic or anisotropic dielectric sample placed in between, as shown in Figure 1.4. In that work, a single antenna

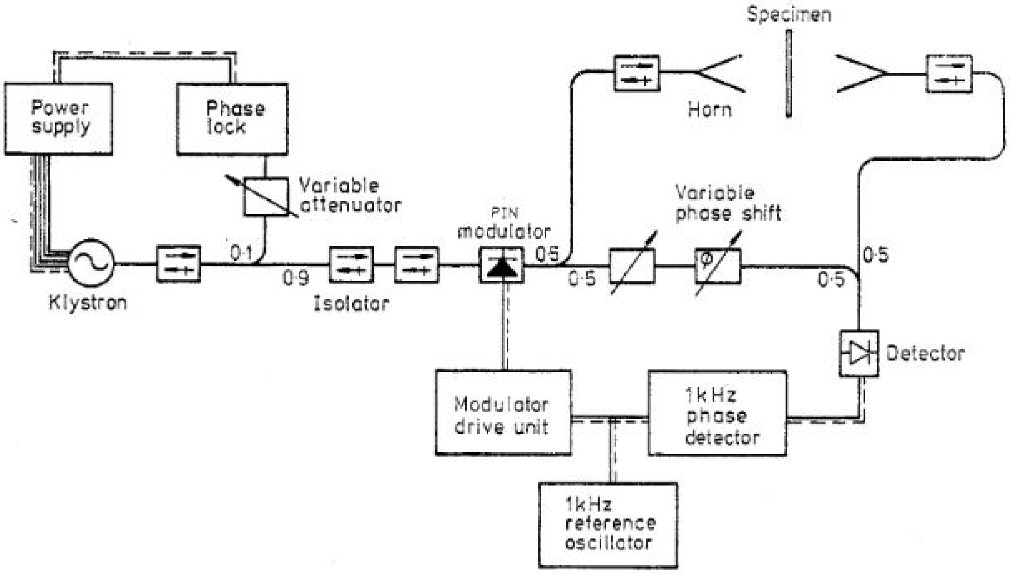

Figure 1.4 System schematic of a through-transmission microwave dielectric measurement setup. Two horn antennas are used to transmit and receive microwave signals, and reflection and transmission coefficients are used to extract complex permittivity values [7].

is also used for reflection-only measurements. A pair of antennas is used in [8] in conjunction with a rotating sample to determine the Brewster angle, the incident angle at which reflection is zero or minimal, which is a simple function of the sample permittivity for low-loss samples.

One type of antenna that can perform reflection measurements (only one measurement port is needed) for samples placed in its near-field is a patch antenna. The patch antenna has both resonator cavity and microstrip properties that set it apart from the other methods described above. The measurement premise is similar to that for cavity measurements, where resonant frequency and Q-factor are the two parameters used to characterize low-conductivity media. This is the measurement method chosen in this work and is described in detail in Chapters 2 and 3.

1.2.2 Capacitive sensing

Where radio frequencies are not a necessary testing band, or are prohibitively expensive for the application at hand due to the high cost of RF testing equipment, capacitive sensing offers the dual benefits of relatively low cost equipment and a linear relationship between relative permittivity of a sample and the measured capacitance. The basic measurement operation of a capacitive sensor is shown in Figure 1.5, where a voltage source V provides an alternating voltage differential between the source electrode and the receiver electrode [9]. An ammeter measures the responding current I flowing through the circuit. A time-harmonic phase difference angle ϕ is observed between the voltage and current, and an impedance is calculated as

$$Z = \frac{|V|}{|I|}(\cos\phi + j\sin\phi) = R + j(X_L - X_C), \tag{1.1}$$

where j is the imaginary unit, X_C is the capacitive reactance and X_L is the inductive reactance that is negligible for low-frequency capacitive circuits. The capacitance C is then calculated from the capacitive reactance as

$$C = \frac{1}{2\pi f X_C}, \tag{1.2}$$

where f is the operating frequency. The magnitude of the capacitance largely depends on the electrode surface area, the spacing between the electrodes, and, of particular interest for materials characterization, the permittivity of the dielectric material between the electrodes.

A parallel plate capacitor produces a largely uniform electric field with field lines parallel to each other and perpendicular to the electrode surface. A one-sided capacitive sensor generally has electrodes on the same plane, however, with an electric field that fringes outward and is most useful in penetrating a dielectric sample, as shown in Figure 1.6. An analytical formula for capacitance per unit length of the structure shown in Figure 1.6 is given in [10]. The two-electrode structure is expanded into an array of interdigital electrodes in [11] and [12] to improve the signal-to-noise ratio and measurable capacitance for flat sample measurements.

For samples of cylindrical geometry, such as insulated wires, a two-electrode, semi-analytical model was developed in [13] and [14] to calculate the capacitance of the electrodes due to changes in a solid dielectric cylinder and dielectric cylinder with a conductive core, respectively. This design was improved in [15] with an arrangement of interdigital electrodes around a dielectric-coated conductive cylinder. The handheld, practical clamp electrode applicator designed in that work forms the basis for Chapter 5 of this dissertation.

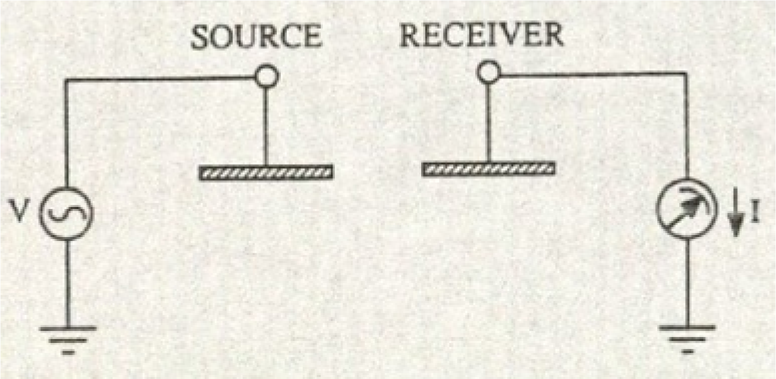

Figure 1.5 Schematic representation of a capacitive sensing circuit, with voltage source V providing an alternating voltage between the Source and Receiver electrodes, and ammeter I measuring the responding alternating current [9]

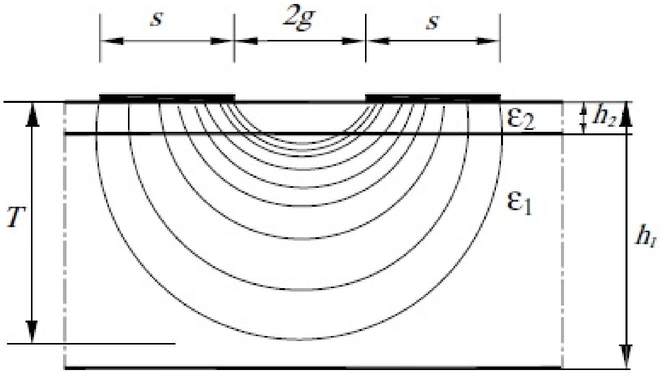

Figure 1.6 Cross-section view of a capacitive sensor in contact with a two layer dielectric sample, showing the fringing electric field penetrating the sample [10]

Planar samples with anisotropic material composition, such as glass-fiber polymer-matrix composites, are the focus of electrode designs in [16], where the measured capacitance is not influenced by orientation of the electrodes relative to the anisotropic sample. This simple two-electrode arrangement is shown in Figure 1.7 with a a honeycomb/glass-fiber sandwich panel, an example of anisotropic, low-conductivity media. This rotationally independent design was improved in [17], again increasing the measured sensor capacitance, with the expansion to an array of interdigital electrodes. This design and its employment to show its capabilities for material characterization are described in Chapter 4.

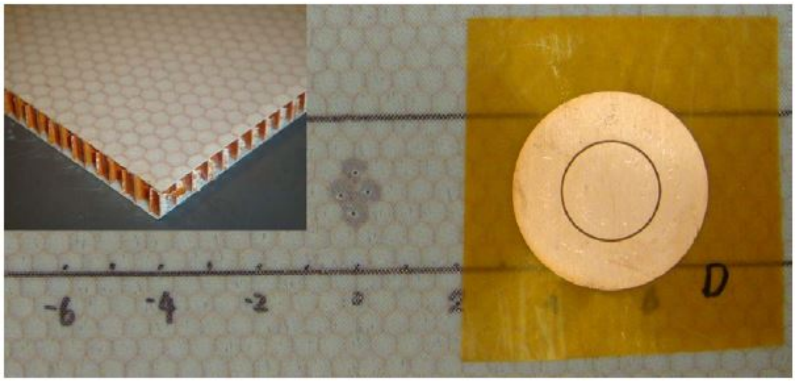

Figure 1.7 Isometric view of a honeycomb/glass-fiber sandwich panel (left) and top view of a concentric two-electrode capacitive sensor (right) with top view of the panel in the background [16].

1.3 Thesis structure

The research presented in this dissertation is divided between two sensing approaches that have the common theme of dielectric characterization of low-conductivity media. Radio frequency sensing is discussed in Chapters 2 and 3, while capacitive sensing is discussed in Chapters 4 and 5.

1.4 References

[1] M. N. Afsar, J. R. Birch and R. N. Clarke, “The Measurement of the Properties of Materials”, *Proc. IEEE*, Vol. 74, No. 1, pp. 183-199, Jan. 1986.

[2] A. M. Nicolson and G. F. Ross, “Measurement of the Intrinsic Properties of Materials by Time-Domain Techniques”, *IEEE Trans. Instr. Meas.*, Vol. 19, No. 4, pp. 377-382, Nov. 1970.

[3] G. D. Dester, E. J. Rothwell and M. J. Havrilla, “An Extrapolation Method for Improving Waveguide Probe Material Characterization Accuracy”, *IEEE Microwave and Wireless Components Lett.*, Vol. 20, No. 5, pp. 298-300, May 2010.

[4] E. Ni and U. Stumper, “Permittivity measurements using a frequency-tuned microwave TE_{01} cavity resonator”, *Proc. IEE*, Vol. 132, Part H, No. 1, pp. 27-32, Feb. 1985.

[5] B. Terselius and B. Ranby, “Cavity Perturbation Measurements of the Dielectric Properties of Vulcanizing Rubber and Polyethylene Compounds”, *J. Microw. Power*, Vol. 13, No. 4, pp. 327-335, 1978.

[6] P. Queffelec, P. Gelin, J. Gieraltowski and J. Loäec, “A Microstrip Device for the Broad Band Simultaneous Measurement of Complex Permeability and Permittivity”, *IEEE Trans. Magn.*, Vol. 30, No. 2, pp.224-231, Mar. 1994.

[7] R. J. Cook and C. B. Rosenberg, "Measurement of the complex refractive index of isotropic and anisotropic materials at 35 GHz using a free space microwave bridge", *J. Phys. D: Appl. Phys.*, Vol. 12, pp. 1643-1652, 1979.

[8] C. K. Campbell, "Free-Space Permittivity Measurements on Dielectric Materials at Millimeter Wavelengths", *IEEE Trans. Instr. Meas.*, Vol. 27, No. 1, Mar. 1978.

[9] M. Gimple and B. A. Auld, "Position and Sample Feature Sensing with Capacitive Array Probes", *Review of Progress in QNDE*, edited by D. O. Thompson and D. E. Chimenti, pp. 509-513, 1987.

[10] A. A. Nassr, W. H. Ahmed, and W. W. El-Dakhakhni, "Coplanar capacitance sensors for detecting water intrusion in composite structures", *Meas. Sci. Technol.*, Vol. 19, pp. 075702(7pp), 2008.

[11] A. V. Mamishev, K. Sundara-Rajan, F. Yang, Y. Du, and M. Zahn, "Interdigital sensors and transducers", *Proc. IEEE*, Vol. 92, pp. 808-845, 2004.

[12] R. Igreja and C. J. Dias, "Analytical evaluation of the interdigital electrodes capacitance for a multi-layered structure", *Sensor Actuat. A-Phys.*, Vol. 12, pp. 291-301, 2004.

[13] T. Chen, N. Bowler and J. R. Bowler, "Analysis of Arc-Electrode Capacitive Sensors for Characterization of Dielectric Cylindrical Rods", *IEEE Trans. Instr. Meas.*, Vol. 61, No. 1, pp. 233-240, 2012.

[14] T. Chen and N. Bowler, "Analysis of a capacitve sensor for the evaluation of circular cylinders with a conductive core", *Meas. Sci. Technol.*, Vol. 23, 045102(10pp), 2012.

[15] R. T. Sheldon and N. Bowler, "An Interdigital Capacitive Sensor for Nondestructive Evaluation of Wire Insulation", *IEEE Sensors J.*, Vol. 14, No. 4, pp. 961-970, Apr. 2014.

[16] T. Chen and N. Bowler, "Analysis of a Concentric Coplanar Capacitive Sensor for Nondestructive Evaluation of Multi-layered Dielectric Structures", *IEEE Trans. Dielectr. Electr. Insul.*, Vol. 17, No. 4, pp. 1307-1318, Aug. 2010.

[17] R. T. Sheldon and N. Bowler, “Dielectrometry Sensors for NDE of Glass-Fiber Polymer-Matrix Composites”, *Mater. Eval.*, Vol. 72, No. 11, pp. 1421-1428, Nov. 2014.

CHAPTER 2. PATCH ANTENNA SENSOR MODEL

2.1 Introduction

In many military aerospace applications, it is desired to know the radar cross-section (RCS) of a particular aircraft. Physical RCS measurements can be obtained in large anechoic chambers or outdoor test ranges, but this is often impractical and expensive [1]. RCS can be determined using finite element simulations, but this requires data on the material properties of the outer layers of the aircraft. Even slight imperfections in the material properties of the outer surfaces can be detectable and may influence the RCS. If the material properties of the outer surfaces can be physically characterized with efficient and low-cost methods, the data can be used with positional information to model RCS, or may simply be used for detection of problem regions.

To minimize radar reflections, many aircraft are not constructed with metallic outer surfaces, but rather low-conductivity, or dielectric, multilayer media that may have microwave absorbing properties, structural properties, or thermal protection properties. Problems in these layers may be structural (e.g. disbonds, inclusions, and voids) or unexpected radio frequency (RF) behavior arising from undesirable dielectric properties. Conventional nondestructive evaluation techniques, such as tap tests, ultrasonic tests, and X-ray scans are widely accepted for characterization of structural problems, but they generally fall short of being able to characterize RF responses.

One type of sensor to determine dielectric properties at radio frequencies is a flanged waveguide [2]. This is a simple waveguide with one end terminated in a flange that is pressed into contact with a sample. The two components of the measured complex reflection coefficient can then be used to determine the two components of complex permittivity of the sample. If complex permeability is also to be determined, then a second waveguide is needed [3]. Thus one independent reflection measurement yields two material parameters and two measurements potentially yield four parameters of a single sample layer.

Another approach to determine unknown dielectric properties is to examine the resonating characteristics of microwave resonators [4]. Specifically, the resonant frequency and quality factor of a microstrip patch antenna shift when a sample is placed in its near-field. These two measurable quantities permit the determination of the two components of the sample complex permittivity [5]. In this chapter, a patch antenna model is examined to characterize theoretical shifts in resonant frequency and quality factor due to a multilayer dielectric sample placed in its vicinity. In the following chapter, design parameters are selected such that the sensor operates in the X-band (8-12 GHz) and measurements are performed to determine the actual resonant parameters and to determine the unknown permittivity values of a sample layer.

2.2 Patch geometry

The patch sensor is comprised of a conductive patch of width W in the x-direction, length L in the y-direction, where $L \geq W$, and thickness t placed above a groundplane (ideally of infinite area) with a substrate of height h_1 and complex permittivity ϵ_1 placed between the patch and groundplane, as shown in Figure 2.1. Above the patch may be placed $N-1$ complex dielectric layers, each with height h_n, with Layer 2 being the first layer above the patch and layer N being the final layer. If Layer N is a halfspace, then $h_N \to \infty$. In this model, all dielectric layers are assumed to have infinite dimensions in the xy-plane. The patch is fed by a cylindrical probe of diameter d_0 at an offset distance of y_0 from the edge of the patch along the length L.

Because of the finite thickness of the patch conductor, where charge accumulates on the finite thickness edge of the patch, the sensor performs as though the patch width W (and length L) appears to be wider than its physical width and should be replaced in all following equations as $W + \Delta W$ [7], where

$$\Delta W = \begin{cases} \dfrac{1.25t}{\pi}\left[1+\ln\left(\dfrac{4\pi W}{t}\right)\right], & \dfrac{W}{h_1} \leq \dfrac{1}{2\pi} \\ \dfrac{1.25t}{\pi}\left[1+\ln\left(\dfrac{2h_1}{t}\right)\right], & \dfrac{W}{h_1} > \dfrac{1}{2\pi}. \end{cases} \tag{2.1}$$

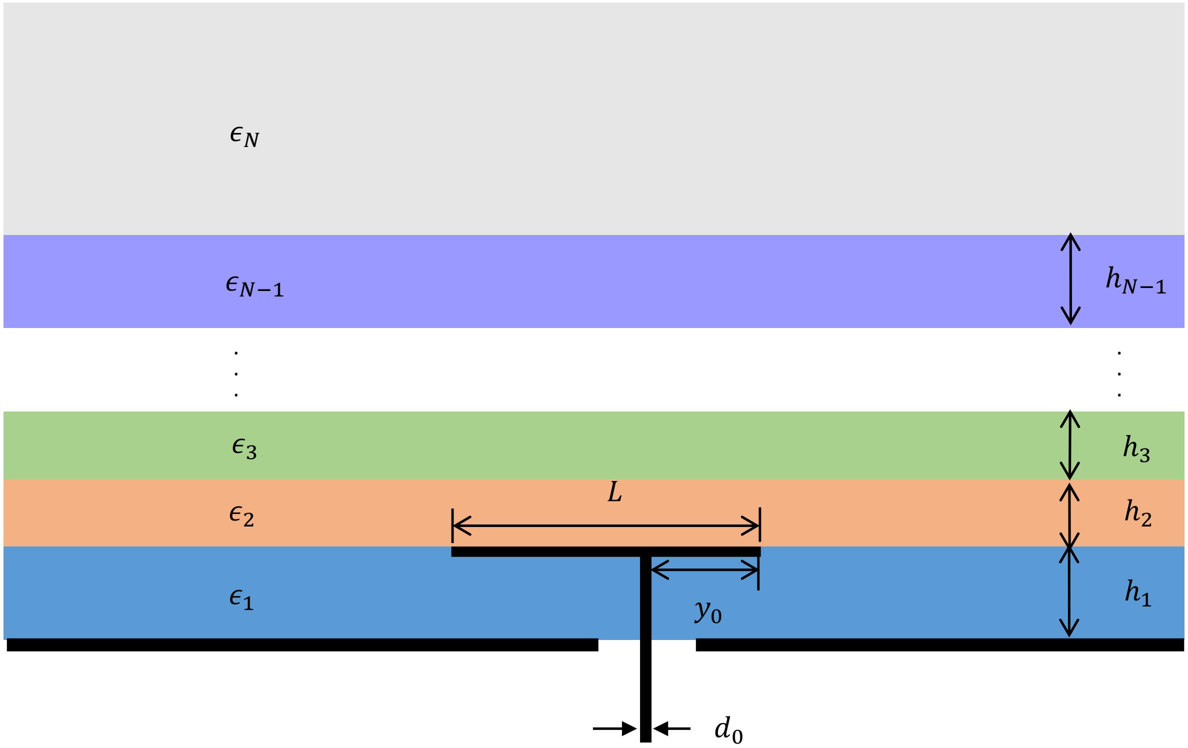

Figure 2.1 Cross-section view of the patch antenna with its substrate represented by Layer 1 and dielectric samples represented by Layers 2 through N. All layers have a height h_n and complex permittivity ϵ_n. The patch is fed by a cylindrical probe of diameter d_0 at distance y_0 from the edge of the patch along the length L.

A similar expression also exists for ΔL by replacing W in the above equation with L.

2.3 Patch antenna operation

The patch antenna, being a rectangular or square conductive sheet separated from an infinitely large groundplane by an infinitely wide dielectric layer, is simply a truncated microstrip. Whereas a microstrip is a transmission line designed to guide microwave energy, via travelling electromagnetic waves, from one location to another, the finite length of the patch antenna results in a standing electromagnetic wave that forms in the substrate region between the patch and groundplane. The inverse of the natural wavelength of the standing wave is proportional to the resonant frequency of the patch. Besides the length of the patch, the width, substrate parameters, and the parameters of the layers exterior to the patch all have an influence on its inherent resonant frequency, which will be discussed further on.

Because the patch is a truncated piece of microstrip transmission line, the patch has some transmission line properties that affect its performance. However, the behavior of the standing waves that form in the rectangular prism region formed beneath the patch mimics properties of a rectangular microwave cavity. Both properties are utilized in this work to calculate the resonant frequency of the patch.

2.3.1 Resonant cavity properties

One aspect of patch antenna operation is that a patch antenna behaves in a similar fashion to a rectangular microwave cavity. A microwave cavity, in general, is any type of structure that confines electromagnetic fields to the volume interior to the cavity, which causes standing waves to form at specific resonant frequencies that depend upon the containment structure geometry and material properties. One type of ideal containment structure that behaves as a resonator is a hollow, rectangular box with all six walls comprised of perfect electrical conductor (PEC). In the case of the patch antennna, the containment structure may be idealized as two PEC walls (the patch and the groundplane) and four perfect magnetic conductor (PMC) walls with a dielectric material filling the space inside the box (and does not extend outside the box). PEC (PMC) boundary conditions in electromagnetic theory are characterized by vanishing tangential electric (magnetic) field at the boundary. The difference in behavior of these two structures is simply the boundary conditions.

To solve for the time-harmonic electromagnetic wave solution in any source-free and lossless region, Maxwell's equations describing the electric and magnetic fields for such a region must first be defined, and are given as

$$\nabla \cdot \mathbf{D} = 0 \qquad \text{Gauss's law} \tag{2.2}$$

$$\nabla \times \mathbf{E} = -j\omega\mathbf{B} \qquad \text{Faraday's law of induction} \tag{2.3}$$

$$\nabla \cdot \mathbf{B} = 0 \qquad \text{Gauss's law for magnetism} \tag{2.4}$$

$$\nabla \times \mathbf{H} = j\omega\mathbf{D} \qquad \text{Ampère's circuital law} \tag{2.5}$$

where $\mathbf{E}$ is the electric field intensity, $\mathbf{D} = \epsilon\mathbf{E}$ is the electric flux density, $\mathbf{H}$ is the magnetic field intensity, $\mathbf{B} = \mu\mathbf{H}$ is the magnetic flux density, ϵ is the electric permittivity, μ is the magnetic permeability, ω is the angular frequency, and $j = \sqrt{-1}$ is the imaginary unit. Before proceeding, it is beneficial to recognize that, due to the region being source-free, both $\mathbf{D}$ and $\mathbf{B}$ lack divergence and, therefore, each can be represented as the curl of another vector field. These are given as

$$\mathbf{D}_{\mathrm{F}} = -\nabla \times \mathbf{F} \tag{2.6}$$

$$\mathbf{B}_{\mathrm{A}} = \nabla \times \mathbf{A}, \tag{2.7}$$

where $\mathbf{F}$ is the electric vector potential and $\mathbf{A}$ is the magnetic vector potential, which are both circulating fields, and the subscripts $_{\mathrm{F}}$ and $_{\mathrm{A}}$ indicate the fields due to the respective vector potentials. The total electric and magnetic field intensities are derived from the vector potentials in [6] as

$$\mathbf{E} = -j\omega\mathbf{A} - j\frac{1}{\omega\mu\epsilon}\nabla(\nabla \cdot \mathbf{A}) - \frac{1}{\epsilon}\nabla \times \mathbf{F} \tag{2.8}$$

$$\mathbf{H} = -j\omega\mathbf{F} - j\frac{1}{\omega\mu\epsilon}\nabla(\nabla \cdot \mathbf{F}) + \frac{1}{\mu}\nabla \times \mathbf{A}. \tag{2.9}$$

It is apparent from these relations that $\mathbf{E}$ and $\mathbf{H}$ are each dependent upon both $\mathbf{F}$ and $\mathbf{A}$. However, some simplification can be performed depending on the operating mode of the cavity.

A variety of electromagnetic field configurations may exist that satisfy both Maxwell's equations and the given boundary conditions, but the most common configurations (or modes) have certain field components transverse to the direction of wave propagation. These are transverse electric (TE), transverse magnetic (TM) and transverse electromagnetic (TEM). In the case of a cavity, which has no direction of propagation, a surface normal direction must be chosen to reference the transverse components; here, the z-direction is chosen as it is the direction normal to a physical patch antenna sensor. For a patch-style resonant cavity with the z-direction normal to the patch surface, the dominant mode (or the mode supporting the lowest possible resonant frequency) is the TM^z mode, which requires that $H_z = 0$. To achieve $H_z = 0$, only A_z must be nonzero, which, when plugged into (2.8) and (2.9) yields the electric and magnetic field intensity components [17]:

$$\begin{aligned} E_x &= -j\frac{1}{\omega\mu\epsilon}\frac{\partial^2 A_z}{\partial x \partial z} \qquad & H_x &= \frac{1}{\mu}\frac{\partial A_z}{\partial y} \\ E_y &= -j\frac{1}{\omega\mu\epsilon}\frac{\partial^2 A_z}{\partial y \partial z} \qquad & H_y &= -\frac{1}{\mu}\frac{\partial A_z}{\partial x} \\ E_z &= -j\frac{1}{\omega\mu\epsilon}\left(\frac{\partial^2}{\partial z^2}+k\right)A_z \qquad & H_z &= 0 \end{aligned} \tag{2.10}$$

The Helmholtz wave equation is then simplified and given as

$$\nabla^2 A_z + k^2 A_z = 0, \tag{2.11}$$

where k is the operating wavenumber and is subject to the constraint condition

$$k^2 = k_x^2 + k_y^2 + k_z^2 = \omega^2\mu\epsilon. \tag{2.12}$$

Equation (2.11) is solved in [6] for a rectangular cavity using a separation of variables method to yield:

$$A_z = \left[B_1\cos(k_x x) + C_1\sin(k_x x)\right]\left[B_2\cos(k_y y) + C_2\sin(k_y y)\right]\left[B_3\cos(k_z z) + C_3\sin(k_z z)\right]. \tag{2.13}$$

The coefficients B and C are found by enforcing two PEC boundary conditions (the top and bottom electrical conductors) and four PMC boundary conditions (the four dielectric sides of the box). The six boundary conditions are given in [17] as:

$$E_x\Big|_{z=0} = E_x\Big|_{z=h_1} = 0 \tag{2.14}$$

$$H_x\Big|_{y=0} = H_x\Big|_{y=L} = 0 \tag{2.15}$$

$$H_y\Big|_{x=0} = H_y\Big|_{x=W} = 0. \tag{2.16}$$

The application of the above boundary conditions finds that $C_1 = C_2 = C_3 = 0$, simplifying A_z to

$$A_z = A_{mnp}\cos(k_x x)\cos(k_y y)\cos(k_z z), \tag{2.17}$$

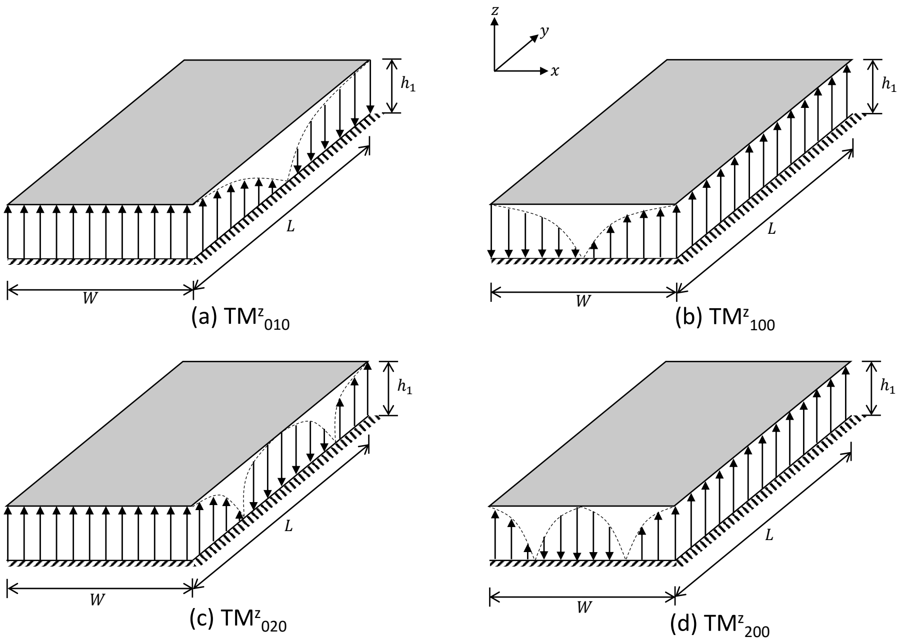

(a) TM$^z_{010}$ (b) TM$^z_{100}$ (c) TM$^z_{020}$ (d) TM$^z_{200}$

Figure 2.2 Rectangular cavity modal electric field pattern between the patch and the groundplane for dominant transverse-magnetic modes with no magnetic field in the z-direction (TM^z). Assuming $L > W > h_1$, TM$^z_{010}$, (a), is the dominant mode. If $L > W > L/2 > h_1$, TM$^z_{100}$, (b), is the next higher-order mode, otherwise if $L > L/2 > W > h_1$, TM$^z_{020}$, (c), will follow the dominant mode. However, if $L > W/2 > L/2 > h_1$, then TM$^z_{200}$, (d), will follow the dominant mode.

where

$$k_x = \frac{m\pi}{W}, \qquad m \in \mathbb{N} \tag{2.18}$$

$$k_y = \frac{n\pi}{L}, \qquad n \in \mathbb{N} \tag{2.19}$$

$$k_z = \frac{p\pi}{h_1}, \qquad p \in \mathbb{N}. \tag{2.20}$$

Using the constraint equation in (2.12), the resonant frequency for this cavity structure is found to be

$$f_{r,mnp} = \frac{1}{2\pi\sqrt{\mu\epsilon}}\sqrt{\left(\frac{m\pi}{W}\right)^2 + \left(\frac{n\pi}{L}\right)^2 + \left(\frac{p\pi}{h_1}\right)^2}, \tag{2.21}$$

where, in this case, $\epsilon = \epsilon_{r1}\epsilon_0$ and $m = n = p \neq 0$.

2.3.2 Microstrip properties

Whereas a microwave cavity is designed to resonate at specific frequencies by the formation of standing waves, a patch antenna also behaves similarly to a microstrip line, which is designed to guide traveling electromagnetic waves between components and devices. This is due to the fact that the patch antenna does not actually have perfect boundary conditions on the four side walls formed in the substrate beneath the patch (treated as PMC boundaries in the section above). In reality, the electric field extends into the air (or sample, as in this work) before returning through the substrate and terminating on the groundplane some distance away from the region covered by the patch. This has the effect of modifying the apparent dimensions of the patch when computing its resonant properties. It is also this "fringing" field that is responsible for the radiation of energy from the patch antenna, when the fields are alternating with time.

A microstrip is simply a piece of transmission line, with an infinitely long conductor line of width W placed above a groundplane of infinite area and separated from the groundplane by a substrate of height h and relative permittivity ϵ_r. As with any transmission line, the main parameter of interest is the characteristic impedance, which is a ratio of the voltage and current amplitudes of an electromagnetic wave that is travelling down the line. A schematic representation of a section of general transmission line is shown in Figure 2.3, where R is the per unit length resistance of the conductors, L is the per unit length inductance of the conductors, G is the per unit length conductance of the substrate, and C is the per unit length capacitance of the line. Using a pair of differential equations known as the *telegrapher's equations*, the voltage and current functions are solved for, and their ratio is the characteristic impedance [18], given in time-harmonic form as

$$Z_0 = \sqrt{\frac{R + j\omega L}{G + j\omega C}}. \tag{2.22}$$

If the line is lossless, then $R = 0$ and $G = 0$, so $Z_0 = \sqrt{L/C}$. Therefore, the line inductance and capacitance must be determined to compute the characteristic impedance of any transmission line.

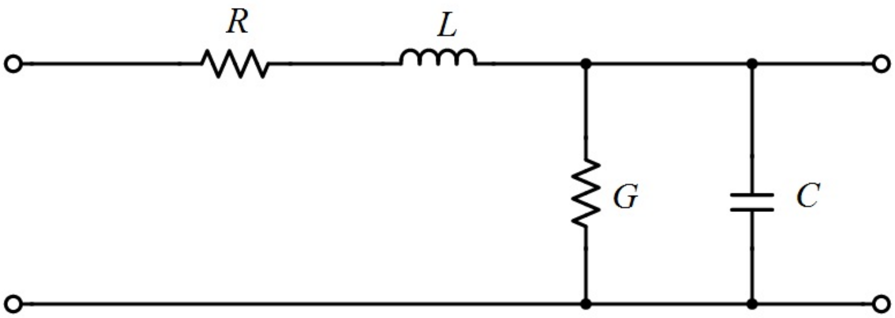

Figure 2.3 Schematic representation of a general transmission line, where R is the conductor resistance per unit length, L is the conductor inductance per unit length, G is the dielectric conductance per unit length, and C is the dielectric capacitance per unit length.

The primary mode of operation of a microstrip is ideally a TEM mode (electric and magnetic field are both transverse to the direction of propagation), but since they actually exist in both the air and substrate, the microstrip can truly only operate as quasi-TEM. For a TEM approximation, the strip can be assumed to be surrounded entirely by an effective dielectric material that has a permittivity value between that of air and the substrate. One popular method of computing this effective permittivity and directly approximating the characteristic impedance of a microstrip was first formulated by Wheeler [11], where a conformal mapping approach was used to determine the effective filling fraction of the substrate, which is used to determine the weight of contribution of the substrate permittivity to the effective permittivity. Using a simplified version of Wheeler's original expressions, the low-frequency characteristic impedance of a microstrip is approximated as follows [6]:

$$Z_0 = \begin{cases} \frac{60}{\sqrt{\epsilon_{r,eff}}} \ln\left(\frac{8h}{W} + \frac{W}{4h}\right), & \frac{W}{h} \leq 1 \\ \frac{120\pi}{\sqrt{\epsilon_{r,eff}}} \left[\frac{W}{h} + 1.393 + 0.667 \ln\left(\frac{W}{h} + 1.444\right)\right]^{-1}, & \frac{W}{h} > 1 \end{cases} \tag{2.23}$$

where

$$\epsilon_{r,eff} = \begin{cases} \frac{\epsilon_r + 1}{2} + \frac{\epsilon_r - 1}{2}\left[\left(1 + 12\frac{h}{W}\right)^{-1/2} + 0.04\left(1 - \frac{W}{h}\right)^2\right], & \frac{W}{h} \leq 1 \\ \frac{\epsilon_r + 1}{2} + \frac{\epsilon_r - 1}{2}\left(1 + 12\frac{h}{W}\right)^{-1/2} & \frac{W}{h} > 1. \end{cases} \tag{2.24}$$

2.4 Resonant frequency model

In this work, the resonant frequency of a patch antenna is modeled using the Modified Wolff Model, which is based upon the computation of the total patch capacitance using a variational method [8]. The region beneath the patch, in the substrate between the patch and groundplane, is assumed to form a cavity where the dominant wave mode is the transverse magnetic, or TM^z (i.e. no magnetic field in the z-direction, the direction of propagation). The resonant frequency of the mn-th mode is defined as

$$f_{mn} = \Re\left[\frac{c}{2\pi\sqrt{\epsilon_{r,dyn}}}k_{mn}\right], \tag{2.25}$$

where c is the speed of light, k_{mn} is the mn-th wavenumber, $\epsilon_{r,dyn}$ is the complex relative dynamic permittivity ($\epsilon_{r,dyn} = \epsilon'_{r,dyn} - j\epsilon''_{r,dyn}$), m is the mode number along the patch width W, and n is the mode number along the patch length L. The mn-th wavenumber is defined as

$$k_{mn} = \sqrt{\left(\frac{m\pi}{W_{eff}}\right)^2 + \left(\frac{n\pi}{L_{eff}}\right)^2} \tag{2.26}$$

where W_{eff} and L_{eff} are the effective width and length of the patch, respectively, due to fringing and will be defined further on.

In this model there are assumed to be N dielectric layers, each with complex permittivity ϵ_{rk} and height h_k, with index $k = 1$ indicating the patch substrate and $k = N$ indicating the final halfspace layer with $h_N \to \infty$. It should be noted here that because complex permittivity values are permissible inputs to the system, all capacitances C, admittances Y, and impedances Z will be assumed to be complex, and the traditional complex asterisk notation (*), in order to eliminate redundancy and improve equation clarity, will be dropped. Where necessary, the real part of a complex variable will be designated with $\Re()$ or primed notation, and the imaginary part will be designated with $\Im()$ or double primed notation. The complex dynamic permittivity of the patch, including all N layers, is defined as

$$\epsilon_{r,dyn} = \frac{C_{dyn}(\epsilon_{r1}...\epsilon_{rN})}{C_{dyn}(\epsilon_{r1}...\epsilon_{rN} = 1)}, \tag{2.27}$$

where $C_{dyn}(\epsilon_{r1}...\epsilon_{rN})$ is the total dynamic capacitance with all dielectric layers included and $C_{dyn}(\epsilon_{r1}...\epsilon_{rN} = 1)$ is the total dynamic capacitance with all layers replaced with air.

Two references will now be defined for continued use in this section: static and dynamic. The term *static* here refers to operation of the patch antenna sensor at zero frequency—that is the electric field in the substrate is uniform. *Dynamic* refers to the electric field variation caused by the operation of the patch at a certain frequency. Thus a capacitance measurement will have different results in the static and dynamic regimes due to the variation in electric field distributions. The total dynamic capacitance is defined as

$$C_{dyn}(\epsilon_{r1}...\epsilon_{rN}) = C_{0,dyn}(\epsilon_{r1}) + 2C_{W,dyn}(\epsilon_{r1}...\epsilon_{rN}) + 2C_{L,dyn}(\epsilon_{r1}...\epsilon_{rN}), \tag{2.28}$$

where $C_{0,dyn}(\epsilon_{r1})$ is the central dynamic capacitance of the patch due to the substrate only, and $C_{W,dyn}(\epsilon_{r1}...\epsilon_{rN})$ and $C_{L,dyn}(\epsilon_{r1}...\epsilon_{rN})$ are the dynamic fringing capacitances along both edges of width W and length L, respectively, due to all layer permittivities. The central dynamic capacitance is obtained from

$$C_{0,dyn}(\epsilon_{r1}) = \frac{C_{0,stat}(\epsilon_{r1})}{\gamma_m \gamma_n}, \tag{2.29}$$

where

$$C_{0,stat}(\epsilon_{r1}) = \epsilon_0 \epsilon_{r1} \frac{WL}{h_1} \tag{2.30}$$

$$\gamma_i = \begin{cases} 1 & i = 0 \\ 2 & i \neq 0 \qquad i = m, n. \end{cases} \tag{2.31}$$

The dynamic fringing capacitances are obtained by

$$C_{W,dyn}(\epsilon_{r1}...\epsilon_{rN}) = \frac{C_{W,stat}(\epsilon_{r1}...\epsilon_{rN})}{\gamma_m} \tag{2.32}$$

and

$$C_{L,dyn}(\epsilon_{r1}...\epsilon_{rN}) = \frac{C_{L,stat}(\epsilon_{r1}...\epsilon_{rN})}{\gamma_n} \tag{2.33}$$

The static fringe capacitances are then found by subtracting the central static capacitance from the total static capacitance:

$$C_{W,stat}(\epsilon_{r1}...\epsilon_{rN}) = \frac{1}{2}\left[C_W(\epsilon_{r1}...\epsilon_{rN})L - C_{0,stat}(\epsilon_{r1})\right] \tag{2.34}$$

$$C_{L,stat}(\epsilon_{r1}...\epsilon_{rN}) = \frac{1}{2}\left[C_L(\epsilon_{r1}...\epsilon_{rN})W - C_{0,stat}(\epsilon_{r1})\right] \tag{2.35}$$

where C_W and C_L are the total static capacitances per unit length for microstrips of width W and L, respectively. It should be mentioned here that, from this point onward, only equations related to the patch width W will be given for brevity since all equations involving W and L are of the same form.

The total static capacitance per unit length is computed via a variational method developed in [9] where a charge density distribution $f_W(x)$ across the surface of the width dimension of the patch is assumed. A variety of distributions can be assumed, but the two distributions investigated by Yamashita are a first-order and a third-order approximation. The first-order approximation assumes a distribution of the form

$$f_W(x) = \begin{cases} |x| & -\frac{W}{2} \leq x \leq \frac{W}{2} \\ 0 & \text{otherwise.} \end{cases} \tag{2.36}$$

Using the Fourier transform[1] of $f_W(x)$

$$\tilde{f}_W(\beta) = \int_{-\infty}^{\infty} f_W(x) e^{j\beta x} dx, \tag{2.37}$$

the transform has the form

$$\frac{\tilde{f}_W(\beta)}{Q} = 2\,\mathrm{sinc}\left(\frac{\beta W}{2}\right) - \mathrm{sinc}^2\left(\frac{\beta W}{4}\right), \tag{2.38}$$

where Q is the total charge per unit length. The third-order charge distribution is approximated as

$$f_W(x) = \begin{cases} 1 + A\left|\frac{2x}{W}\right|^3 & -\frac{W}{2} \leq x \leq \frac{W}{2} \\ 0 & \text{otherwise.} \end{cases} \tag{2.39}$$

If $A = 1$, the Fourier transform has the form

$$\frac{\tilde{f}_W(\beta)}{Q} = \frac{8}{5}\,\mathrm{sinc}\left(\frac{\beta W}{2}\right) + \frac{12}{5}\left(\frac{\beta W}{2}\right)^{-2}\left[\cos\left(\frac{\beta W}{2}\right) - 2\,\mathrm{sinc}\left(\frac{\beta W}{2}\right) + \mathrm{sinc}^2\left(\frac{\beta W}{4}\right)\right]. \tag{2.40}$$

From Figure 2.4(b), it may be seen that the Fourier transform of the third-order distribution function converges slightly faster than that of the first-order. This choice will speed up computation, but if that is not a concern, either distribution will give very similar results when integrated. The third-order function will be used here in all further computations.

---

[1] Traditional Fourier transform is defined with $-j\beta x$ while Yamashita uses $+j\beta x$

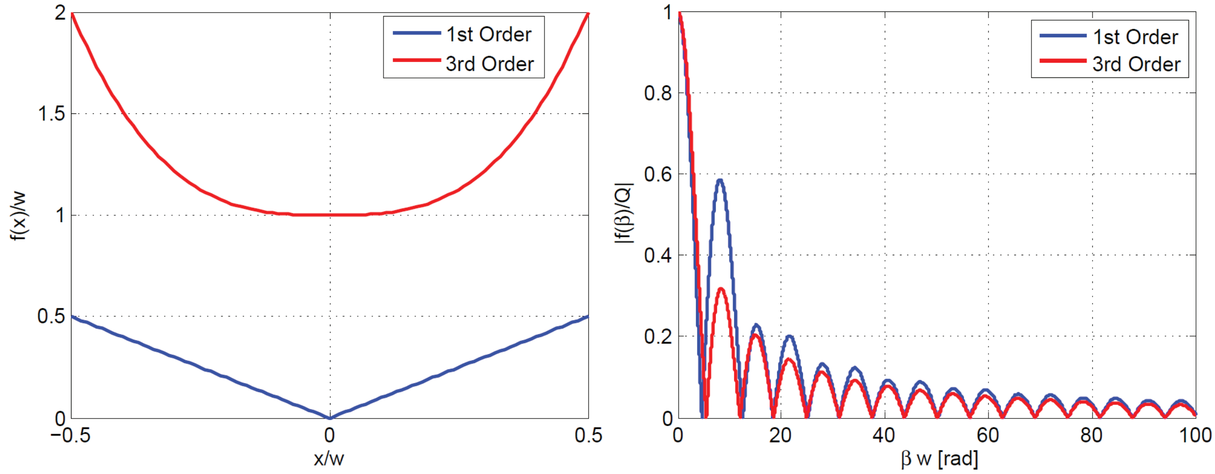

(a) (b)

Figure 2.4 Plots of the calculated analytical (a) charge distribution test functions and (b) the Fourier spectrum of the distributions. In this plot, $W = 10$ mm.

The total static capacitance per unit length is then computed as

$$\frac{1}{C_W} = \frac{1}{\pi\epsilon_0}\int_0^{\infty}\left(\frac{\tilde{f}_W(\beta)}{Q}\right)^2 \frac{1}{\beta Y(\beta)} d\beta \tag{2.41}$$

where $Y(\beta)$ is the normalized admittance function, which is very important in this research as it contains the height and complex permittivity information for every layer. The normalized admittance function is calculated as the sum of the normalized admittance contributed by both the substrate and the material above the patch, the kth layer of which is calculated in an iterative procedure given by

$$Y_k(\beta) = \begin{cases} \epsilon_{r1}\coth(\beta h_1), & k = 1 \\ \epsilon_{rk}\dfrac{Y_{k+1}(\beta) + \epsilon_{rk}\tanh(\beta h_k)}{\epsilon_{rk} + Y_{k+1}(\beta)\tanh(\beta h_k)}, & k = 2, 3, ..., N-1 \\ \epsilon_{rN}, & k = N \end{cases} \tag{2.42}$$

The total normalized admittance is then computed as $Y(\beta) = Y_1(\beta) + Y_2(\beta)$. Thus, in a simple case where a single dielectric layer is above the patch followed by a halfspace media, the total normalized admittance is given as

$$Y(\beta) = \epsilon_{r1}\coth(\beta h_1) + \epsilon_{r2}\left[\frac{\epsilon_{r3} + \epsilon_{r2}\tanh(\beta h_2)}{\epsilon_{r2} + \epsilon_{r3}\tanh(\beta h_2)}\right]. \tag{2.43}$$

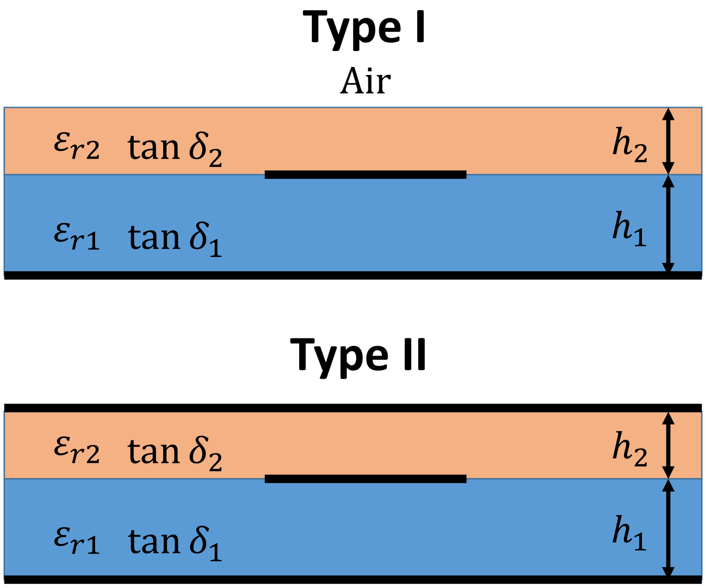

Figure 2.5 Two fundamental layer arrangements above a patch antenna. Type I shows a single dielectric layer above the patch with an open air background. Type II shows a single dielectric layer backed by a PEC groundplane.

If layer N has a finite thickness and is bounded by a PEC plane, $Y_N(\beta)$ in (2.42) can be replaced with $Y_N(\beta) = \epsilon_{rN} \coth(\beta h_N)$. Two fundamental cases are shown in Figure 2.5.

The effective width W_{eff} and length L_{eff} in (2.26) represent the apparent patch dimensions due to both fringing fields and the inhomogeneity in the dielectric materials surrounding the patch. The effective length is defined as

$$L_{eff} = L + \frac{W_{eq} - W}{2} \frac{\epsilon_{r,eff}(W) + 0.3}{\epsilon_{r,eff}(W) - 0.258}, \tag{2.44}$$

where W_{eq} is the equivalent width of the patch due solely to the influence of fringing electric fields [10] and is defined as

$$W_{eq} = \frac{\eta_0 h_1}{Z'_W \sqrt{\epsilon'_{r,eff}(W)}}. \tag{2.45}$$

The static effective relative permittivity $\epsilon_{r,eff}(W)$ represents a homogeneous dielectric medium surrounding the patch and is defined as the ratio of the static capacitance in (2.41) with the substrate and dielectric layers to that with only air, and includes a patch conductor thickness t correction [8], such that

$$\epsilon_{r,eff}(W) = \frac{C_W}{C_{0,W}} - \frac{\epsilon_{r,eq} - 1}{4.6} \frac{t/h_1}{\sqrt{W/h_1}}, \tag{2.46}$$

where $\epsilon_{r,eq}$ is the equivalent relative permittivity of the homogeneous effective medium collapsed into a single dielectric layer bounded by air. The thickness correction is due to charge accumulation on the finite thickness edge leading to more electric field lines originating from this edge than in the ideal zero-thickness case, thus the patch appears wider and alters the apparent effective permittivity, which must be corrected. The equivalent permittivity is generally a complex value where the real and imaginary parts are defined as

$$\epsilon'_{r,eq}(W) = \frac{\Re\left[C_W/C_{0,W}\right] - 1}{q} + 1 \tag{2.47}$$

$$\epsilon''_{r,eq}(W) = \frac{\Im\left[C_W/C_{0,W}\right]}{q}, \tag{2.48}$$

where q is the filling fraction of the substrate representing how much field energy is contained between the patch and groundplane, defined as

$$q = \frac{1}{2}(p+1) \tag{2.49}$$

and

$$p = \begin{cases} \left(1 + 12\frac{h_1}{W}\right)^{-1/2}, & W/h_1 > 1 \\ \left(1 + 12\frac{h_1}{W}\right)^{-1/2} + 0.04\left(1 - \frac{W}{h_1}\right)^2, & W/h_1 \leq 1 \end{cases} \tag{2.50}$$

When W/h_1 is very large, q approaches a value of 1, meaning all electrical energy is confined to the substrate region. Conversely, when W/h_1 is very small, q approaches a value of 0.5, meaning the electric field energy is equally split between the substrate and air.

The characteristic impedance Z_W in (2.45) is the voltage-to-current amplitude ratio of an electromagnetic wave propagating down a microstrip. A variety of closed-form expressions, such as those given by Wheeler [11] and Hammerstad-Jensen [12], exist for rapid and accurate computation of the characteristic impedance. However, the characteristic impedance may be calculated using the static line capacitance in (2.41) [8], such that

$$Z_W = \frac{1}{c\,C_{0,W}\sqrt{\epsilon_{r,eff}(W)}}. \tag{2.51}$$

2.5 Q-factor model

One figure-of-merit when describing an electrical circuit is the ratio between resistive and reactive components. When describing a resonator, this ratio, the quality factor (Q-factor), indicates how well-damped the oscillations are per cycle. A higher Q-factor (> 0.5) indicates underdamping, or lower energy lost to the circuit per cycle, while lower Q-factor (< 0.5) indicates overdamping and lack of oscillations.

The ratio definition of Q-factor depends upon whether the circuit is structured as a series or parallel circuit, since both circuits behave as the inverse of the other. For example, a series RLC resonator (an inductance L, a capacitance C, and resistance R in series) will have a minimum impedance at the resonant frequency as both reactive components have resonated each other out to form a short circuit, leaving only the R component. A parallel RLC resonator will achieve a maximum impedance at resonance as both reactive components have resonated each other out to form an open circuit. Thus the theoretical circuit Q-factor for both orientations is defined using circuit elements as:

$$Q = \begin{cases} \frac{\omega_0 L}{R} = \frac{1}{\omega_0 RC}, & \text{series} \\ \frac{R}{\omega_0 L} = \omega_0 RC, & \text{parallel} \end{cases} \tag{2.52}$$

Equivalent circuit components for a patch antenna sensor form a parallel RLC circuit, which means that the measured input resistance achieves a maximum and the input reactance equals zero at resonance.

As the Q-factor is a ratio of resistive and reactive impedances, there are a variety of material and geometrical contributions that affect its value. For a patch antenna, there are four main contributions which are derived from the losses in the patch circuit:

- Conductor loss Q-factor (Q_c)—The conductors comprising the patch and groundplane cause energy loss to the circuit that depend upon the frequency, conductivity, and effective permittivity of the patch.

- Dielectric loss Q-factor (Q_d)—The dielectric layers comprising the substrate and sample are, in general, complex and the imaginary component of the effective permittivity acts to decrease Q_d.

- Radiation loss Q-factor (Q_r)—The patch is an antenna designed to radiate energy from the circuit, which manifests as a loss to the circuit. This is generally the largest contributor to the total Q-factor of the patch.
- Surface wave loss Q-factor (Q_{sw})—The patch antenna excites some surface waves at the interface between the substrate and air and are viewed as a loss by the system.

Each Q-factor loss contribution coexists in parallel with the other, leading to a total Q-factor Q_t defined as:

$$\frac{1}{Q_t} = \frac{1}{Q_c} + \frac{1}{Q_d} + \frac{1}{Q_r} + \frac{1}{Q_{sw}} \tag{2.53}$$

In this work, Q_d contains the information about the complex permittivity of a test sample in close proximity to the patch antenna sensor and, as such, is of primary focus in relation to determining imaginary permittivity of a test sample. First, however, the forward Q-factor model will be presented by detailing the components of each loss contribution.

2.5.1 Conductor loss Q-factor Q_c

The Q-factor of the patch antenna due to conductor losses in the patch and groundplane may be expressed as

$$Q_c = \frac{\pi f_r \sqrt{\epsilon'_{r,av}}}{c\alpha_c}, \tag{2.54}$$

where α_c is the loss coefficient due to the conductors and $\epsilon'_{r,av}$ is the real part of the average static effective permittivity of the patch [13], defined

$$\epsilon_{r,av} = \frac{1}{2}\left[\epsilon_{r,eff}(W) + \epsilon_{r,eff}(L)\right]. \tag{2.55}$$

The terms $\epsilon_{r,eff}()$ appearing in (2.55) are given by (2.46). The loss coefficient in dB per unit length is given as

$$\alpha_c = \frac{8.686\pi f_r \sqrt{\epsilon'_{r,av}}}{c} \frac{\Delta Z}{Z_0}, \tag{2.56}$$

where Z_0 is the average characteristic impedance of an air-filled patch, given by $Z_0 = \frac{2}{c(C_{0,W}+C_{0,L})}$, and ΔZ is the fractional change in characteristic impedance due to the operating skin depth δ_s corrections to the patch width, height, and thickness [14]:

$$\Delta Z = Z_0(\delta_s) - Z_0. \tag{2.57}$$

These corrections amount to replacing W (or L), h_1 and t in (2.41) with $W - \delta_s$, $h_1 + \delta_s$ and $t - \delta_s$, respectively. The skin depth δ_s is the depth into a lossy medium at which the propagating electric field amplitude (or induced current density amplitude) has decayed to $1/e$ (or about 37 %) of its incident value. The depth is defined in non-permeable materials as

$$\delta_s = \frac{1}{\sqrt{\pi f_r \mu_0 \sigma}}, \tag{2.58}$$

where σ is the conductivity of the patch conductors.

Inserting (2.56), converted to nepers per unit length by the relation 1 Np = 8.686 dB, into (2.54), the expression for Q_c simplifies to

$$Q_c = \frac{Z_0}{\Delta Z}. \tag{2.59}$$

An example calculation for Q_c is plotted in Figure 2.6 with varying substrate height and conductor thickness. From this figure, it is apparent that conductor loss (inverse of Q_c) increases with thinner conductors and becomes less pronounced with thinner substrates. This can be explained physically by the simple fact that conductors with smaller cross-sectional area exhibit more resistance to current flow, so the loss increases. Also, when the resonant frequency increases, the skin depth decreases, which increases the effective patch width and decreases the effective substrate height. This dual action increases the patch capacitance, which decreases the characteristic impedance change ΔZ. Although the loss coefficient α_c is proportional to resonant frequency as in (2.56), this frequency dependence is canceled out in the equation for Q_c, leaving only the ΔZ dependence on frequency. Therefore, Q_c increases with increasing resonant frequency.

If a sample layer is backed by a metal backplane, then one more correction that needs to be made in (2.57) for ΔZ is to increase the sample height layer, or layers, by δ_s to take account of the skin depth in the sample backplane [14].

2.5.2 Dielectric loss Q-factor Q_d

The Q-factor of the patch antenna due to dielectric losses in the substrate and sample layers is defined as

$$Q_d = \frac{\pi f_r \sqrt{\epsilon'_{r,eff}}}{c\alpha_d}, \tag{2.60}$$

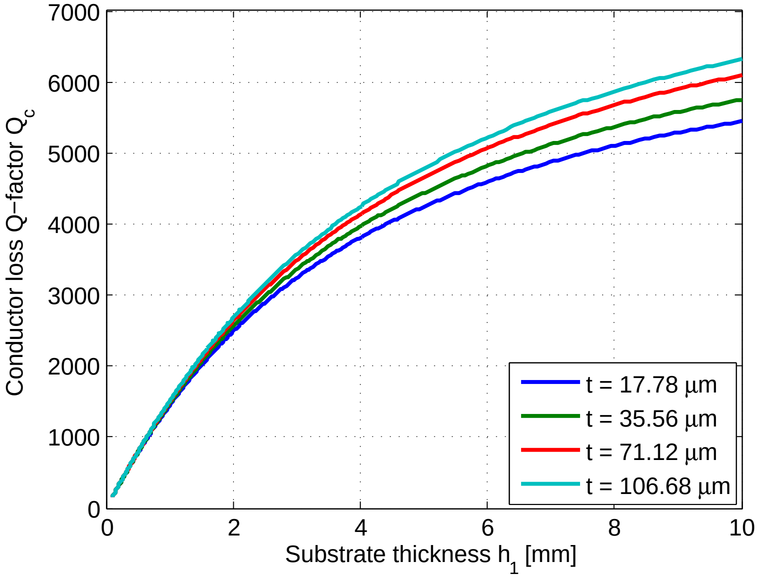

Figure 2.6 Calculated conductor loss Q-factor Q_c as a function of changes in substrate height h_1 and patch thickness t using (2.59). The thicknesses given are those most commonly used in PCB manufacturing and are more often written, from smallest to largest, in ounces of copper (per square foot): 0.5 oz, 1 oz, 2 oz and 3 oz. The patch parameters used here are: $W = L = 10$ mm, $h_1 = 1$ mm, and $\sigma = 58$ MS/m.

where α_d is the dielectric loss coefficient, given in dB per unit length as [16]

$$\alpha_d = \frac{8.686\pi f_r \sqrt{\epsilon'_{r,eff}}}{c} \frac{\epsilon'_{r,eq}(\epsilon'_{r,eff} - 1)}{\epsilon'_{r,eff}(\epsilon'_{r,eq} - 1)} \tan\delta_{eq}, \tag{2.61}$$

where $\epsilon'_{r,eq}$ is the equivalent real permittivity of a single layer between the patch and groundplane in air and $\tan\delta_{eq}$ is the equivalent loss tangent (or dissipation factor) of the single layer. An example of the loss coefficient behavior is plotted in Figure 2.7. The equivalent loss tangent of the single layer is defined as

$$\tan\delta_{eq} = \frac{\epsilon''_{r,eq}}{\epsilon'_{r,eq}} = \frac{\epsilon''_{r,eff}}{\epsilon'_{r,eff} + q - 1}. \tag{2.62}$$

When (2.47), (2.48) and (2.62) are substituted into (2.60), the quality factor due to dielectric loss reduces to

$$Q_d = \frac{1}{\tan\delta_{eff}}, \tag{2.63}$$

where $\tan\delta_{eff} = \epsilon''_{r,eff}/\epsilon'_{r,eff}$. Thus, for increasing lossiness of substrate or sample layers, the effective loss tangent increases and the dielectric Q-factor decreases. When Q_d decreases to

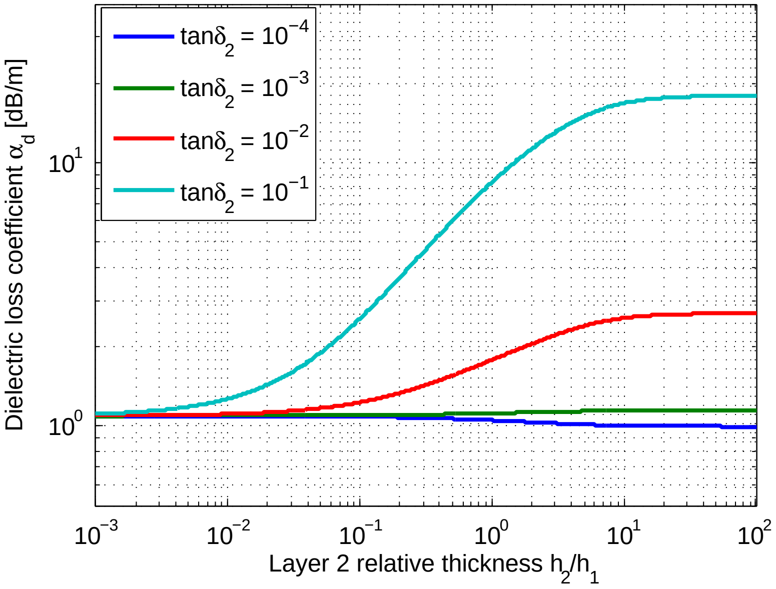

Figure 2.7 Calculated dielectric loss coefficient α_d as a function of changes in Layer 2 height h_s and loss tangent $\tan\delta_2$ using (2.61). The patch parameters used here are: $W = L = 10$ mm, $h_1 = 1$ mm, $\epsilon_{r1} = 2$, $\tan\delta_1 = 0.001$, and $t = 35.56$ µm.

an order of magnitude approaching that of the dominant radiation loss Q_r, it will begin to dominate the loss contributions and significantly reduce the total Q-factor. It is also obvious from (2.63) that Q_d is independent of frequency, if dispersion is negligible in both the patch substrate and sample superstrate(s).

An example plot of Q_d as a function of sample layer height and loss tangent is given in Figure 2.8. From this figure, it may be seen that as the sample loss tangent increases by orders of magnitude, for very thick layers Q_d drops significantly under circumstances in which the loss tangent of the sample superstrate is higher than that of the patch substrate. This is not very noticeable for thin layers, but Q_d changes rapidly with layers on the same order of thickness as the substrate before approaching limiting values at approximately ten times the substrate thickness.

2.5.3 Radiation loss Q-factor Q_r

Since the primary purpose of an antenna is to radiate energy away from the transmitting system, the radiated proportion of the total energy should be expected to be quite high rel-

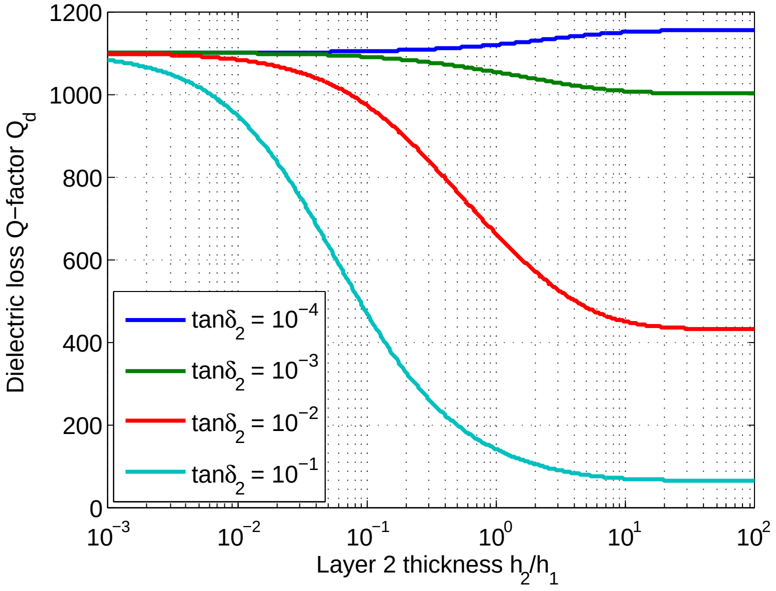

Figure 2.8 Calculated dielectric loss Q-factor Q_d due to changes in substrate height h_1 and Layer 2 loss tangent $\tan\delta_2$ using (2.63). The patch parameters used here are: $W = L = 10$ mm, $h_1 = 1$ mm, $\epsilon_{r1} = 2$, $\tan\delta_1 = 0.001$, and $t = 35.56$ µm.

ative to the other mechanisms discussed above. Although the patch antenna is modeled as a cavity, where there are no radiation losses and only a purely imaginary input impedance, the true radiation loss effect can be modeled as a shunt conductance G_r between the patch and groundplane, defined as

$$G_r = \frac{I(X)}{\pi\eta_0}, \tag{2.64}$$

where

$$I(X) = \int_0^\pi F(X,\theta)\sin^2\theta d\theta = \int_0^\pi \left[\frac{\sin\left(\frac{X}{2}\cos\theta\right)}{\cos\theta}\right]^2 \sin^3\theta d\theta, \tag{2.65}$$

$F(X,\theta)$ is the far-field pattern of the electric field (E_ϕ-component), and $X = 2\pi f W_{eq}/c$. Essentially, the rectangular region bounded by the width-side edge of the patch and the groundplane is assumed to be a radiating aperture, or slot, of width W_{eq} in the midst of a groundplane, where the aperture is assumed to have a uniform electric field distribution per unit length [15]. According to [17], (2.65) has closed-form solution:

$$I(X) = \cos X + X\,\mathrm{Si}(X) + \mathrm{sinc}\,X - 2, \tag{2.66}$$

where $\mathrm{Si}(X)$ is the sine integral,

$$\mathrm{Si}(X) = \int_0^X \frac{\sin t}{t} dt = \int_0^X \operatorname{sinc} t dt. \tag{2.67}$$

However, numerical computation of the sine integral in programs such as MATLAB may be slow, so [19] provides an approximation for G_r that is much faster:

$$G_r = \begin{cases} \frac{W_{eq}^2}{90\lambda_0^2}, & W_{eq} < 0.35\lambda_0 \\ \frac{W_{eq}}{120\lambda_0} - \frac{1}{60\pi^2}, & 0.35\lambda_0 \leq W_{eq} < 2\lambda_0 \\ \frac{W_{eq}}{120\lambda_0} & W_{eq} \geq 2\lambda_0, \end{cases} \tag{2.68}$$

where λ_0 is the free-space resonant wavelength, $\lambda_0 = c/f_r$. Computation speed of the sine integral may also be improved by using a series expansion, such that

$$\mathrm{Si}(X) = \sum_{n=0}^{\infty} (-1)^n \frac{X^{2n+1}}{(2n+1)(2n+1)!}, \tag{2.69}$$

where the finite number of summation terms required for an accurate approximation depends upon the size of X [20].

The Q-factor due to radiation loss is then defined as

$$Q_r = \frac{\pi}{4G_r Z_W}, \tag{2.70}$$

where Z_W is the characteristic impedance of the patch antenna sensor from the width side, given in (2.51). From this relationship, it may be seen that a number of contributing factors will increase Q_r (i.e. reduce radiation losses): decreasing W, decreasing h_1, increasing $\epsilon_{r,eff}$, and decreasing resonant frequency f_r. If metal backs a sample layer, then Z_W will decrease, which increases Q_r. This makes intuitive sense as a conductor positioned in the vicinity of the patch antenna sensor acts to reduce its radiating capability.

Figure 2.9 plots the radiation losses as a function of sample permittivity and height. For very small sample layers, the Q-factor approaches the value for that in air, but as the height increases, the radiation decreases. The same effect occurs with increasing permittivity. This is due to the strong contrast with air, the latter being more conducive to radiation.

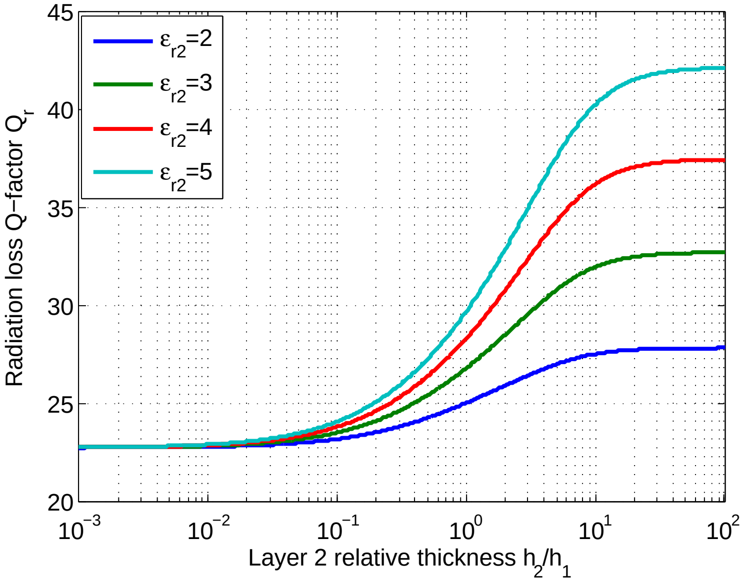

Figure 2.9 Calculated radiation loss Q-factor Q_r due to changes in Layer 2 height and permittivity using (2.70). The patch parameters used here are: $W = L = 10$ mm, $h_1 = 1$ mm, $\epsilon_{r1} = 2$, $\tan\delta_1 = 0.001$, and $t = 35.56$ µm.

2.5.4 Surface wave loss Q-factor Q_{sw}

Since the patch is located at the interface between two different dielectric media, it excites electromagnetic surface waves that propagate along the substrate-air or substrate-sample interface. The surface waves do not radiate out into free space and, therefore, detract from the intended efficiency of the antenna. This means that surface waves are a loss mechanism that are separate from, but related to, the total radiated power. According to [21], it is important to compute this loss because it “constitutes a significant loss (generally a greater loss than either dielectric or conductor loss)” and its power can “diffract from substrate edges or other discontinuities to degrade sidelobe levels or polarisation purity.”

The Q-factor of the patch antenna sensor due to surface-wave loss is given in [19] as

$$Q_{sw} = Q_r \frac{P_{sp}}{P_{sw}}, \tag{2.71}$$

where P_{sp} is the power radiated into the space beyond the substrate and patch and P_{sw} is the power radiated as surface waves along the substrate interface. The space-wave power is defined in [21] as

$$P_{sp} = -\Re\left[\int_S E_{xx} J_x dS\right] \tag{2.72}$$

$$\simeq \frac{\eta_0 k_0^2 (k_0 h_1)^2}{3\pi}\left[1 - \frac{1}{\epsilon'_{r,eq}(W)} + \frac{2}{5\epsilon'^2_{r,eq}(W)}\right],$$

where J_x is an x-directed infinitesimal current source, located at $(0, 0, h_1)$, E_{xx} is the resulting electric field located on the substrate surface at (x, y, h_1), and $k_0 = 2\pi/\lambda_0$ is the resonant wavenumber in air.

The surface-wave power is similarly calculated as

$$P_{sp} = -\Re\left[\int_S \mathrm{Res}(E_{xx}) J_x dS\right] \tag{2.73}$$

$$= \frac{\eta_0 k_0^2}{4}\frac{\epsilon'_{r,eq}(W)(x_p^2 - 1)}{\epsilon'_{r,eq}(W)\left[\frac{1}{\sqrt{x_p^2-1}} + \frac{\sqrt{x_p^2-1}}{\epsilon'_{r,eq}(W)-x_p^2}\right] + \left[1 + \frac{\epsilon'^2_{r,eq}(W)(x_p^2-1)}{\epsilon'_{r,eq}(W)-x_p^2}\right](k_0 h_1)},$$

where $\mathrm{Res}(E_{xx})$ is the residue of the electric field at a pole created by a TM-component of the Green's function in [21], and x_p is the normalized root of the propagation constant causing the pole [22], given by

$$x_p = 1 + \frac{-\epsilon'^2_{r,eq}(W) + \alpha_0\alpha_1 + \epsilon'_{r,eq}(W)\sqrt{\epsilon'^2_{r,eq}(W) - 2\alpha_0\alpha_1 + \alpha_0^2}}{\epsilon'^2_{r,eq}(W) - \alpha_1^2} \tag{2.74}$$

$$\alpha_0 = s\tan(k_0 h_1 s) \tag{2.75}$$

$$\alpha_1 = -\frac{1}{s}\left[\tan(k_0 h_1 s) + \frac{k_0 h_1 s}{\cos^2(k_0 h_1 s)}\right] \tag{2.76}$$

$$s = \sqrt{\epsilon'_{r,eq}(W) - 1}, \tag{2.77}$$

which is an exact solution for all possible values of the equivalent permittivity. For lower permittivity values (approximately $\epsilon_r < 10$), a simpler approximation for the surface-wave

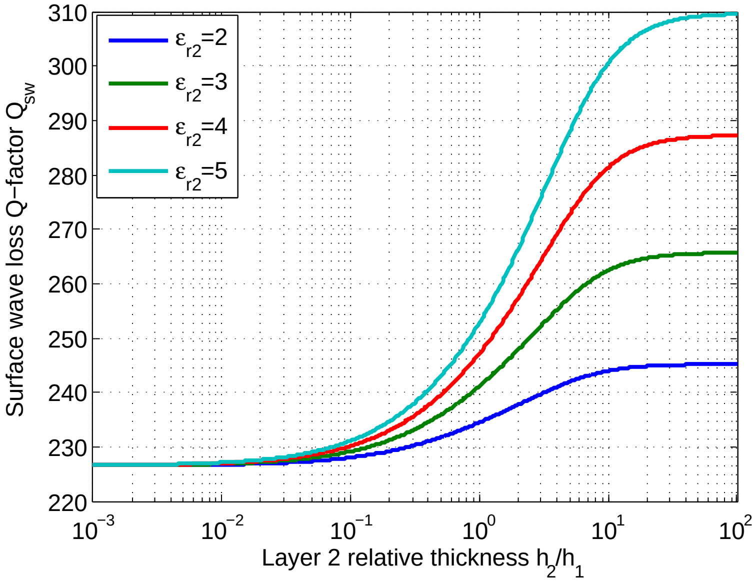

Figure 2.10 Calculated surface-wave loss Q-factor Q_{sw} due to changes in substrate height and permittivity using (2.71). The patch parameters used here are: $W = L = 10$ mm, $h_1 = 1$ mm, $\epsilon_{r1} = 2$, $\tan\delta_1 = 0.001$, and $t = 35.56$ µm.

power is given in [21] as

$$P_{sw} \simeq \frac{\eta_0 k_0^2}{4} \frac{[\epsilon'_{r,eq}(W) - 1]^3 (k_0 h_1)^3}{\epsilon'^3_{r,eq}(W)}. \tag{2.78}$$

Figure 2.10 plots the surface wave loss as a function of sample layer height and permittivity. The behavior essentially matches that of Q_r but is a fraction of its loss. Compared to Q_c and Q_d shown in the previous subsections, Q_{sw} is much more significant and is the second-most significant loss behind Q_r, but this is only true for the specific examples given. Factors that will increase Q_{sw} (decrease surface wave loss) are: increased Q_r, decreased substrate height h_1, decreased resonant frequency, and decreased substrate or sample permittivity.

2.5.5 Total losses Q-factor Q_t

As shown in 2.53, the total Q-factor is a parallel combination of the four main loss contributions. The radiation loss will usually dominate, followed by surface wave loss, conductor loss and dielectric loss, the order of which depends upon the patch and sample geometry and dielectric materials. The total loss Q-factor Q_t will always be lower than than Q_r due to the parallel effect of the other losses. For example, if $Q_r = 20$, $Q_{sw} = 400$, $Q_c = 1000$ and $Q_d = 2000$, then

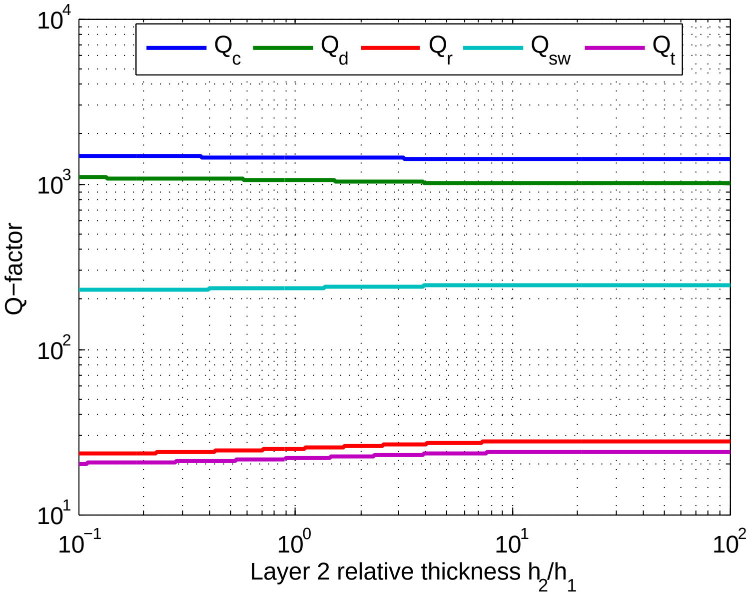

Figure 2.11 Calculated contributions to the total Q-factor Q_t as a function of sample layer height h_2. The parameters used in this example are: $W = L = 10$ mm, $h_1 = 1$ mm, $\epsilon_{r1} = \epsilon_{r2} = 2$, $\tan\delta_1 = \tan\delta_2 = 0.001$, and $t = 35.56$ µm.

$Q_t = 18.5$, just slightly less than Q_r. Generally, Q_t lies between 0.5 and Q_r for a resonating patch antenna sensor.

Figures 2.11, 2.12 and 2.13 show the loss component contributions to the total Q-factor as a function of sample layer height, permittivity and loss tangent, respectively, for one example set of geometrical and dielectric parameters. In Figure 2.11, there is very little variation in Q_t as a function of the thickness of Layer 2, mainly due to the low contrast between the substrate and the sample permittivity. In Figure 2.12, there is a noticeable increase in Q_t with increasing sample permittivity, but the effect is not very strong due to the small sample thickness. In Figure 2.13, the most interesting observation is that as loss tangent increases toward unity, Q_d competes with Q_r for dominance, and therefore Q_t becomes heavily influenced by Q_d. Another observation is the additional inflections of Q_c, Q_r and Q_{sw} as the loss tangent approaches unit—this is due to the now-significant influence of the imaginary permittivity on the resonant frequency, as given in 2.25.

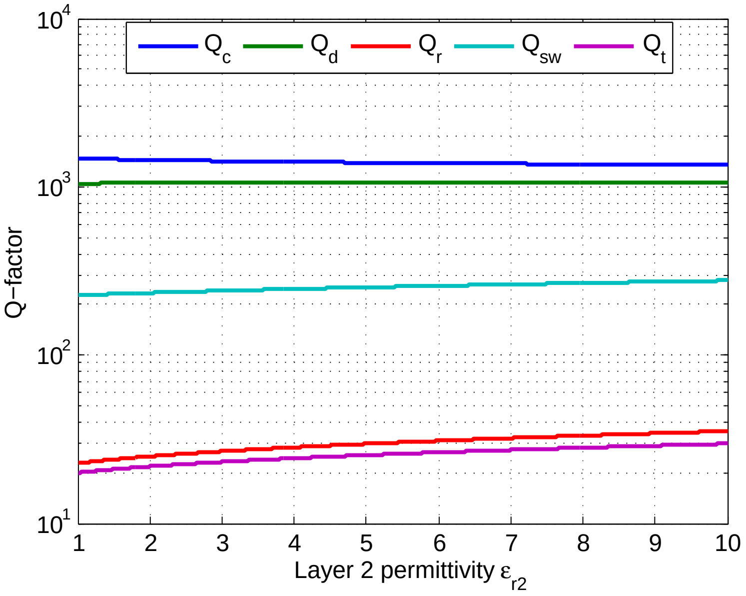

Figure 2.12 Calculated contributions to the total Q-factor Q_t as a function of sample layer permittivity ϵ_{r2}. The patch parameters used in this example are: $W = L = 10$ mm, $h_1 = 1$ mm, $\epsilon_{r1} = 2$, $\tan\delta_1 = \tan\delta_2 = 0.001$, and $t = 35.56$ µm.

2.6 Conclusion

In this chapter a detailed model from literature for calculating the resonant frequency and Q-factor of a patch antenna sensor as a function of the parameters of one or more sample layers was presented. The loss contributions to the total Q-factor were analyzed and examples were given to aid understanding of the various loss mechanisms. In the next chapter, the model described here will be used to design a physical patch antenna sensor for X-band operation and nondestructive evaluation of actual low-conductivity samples.

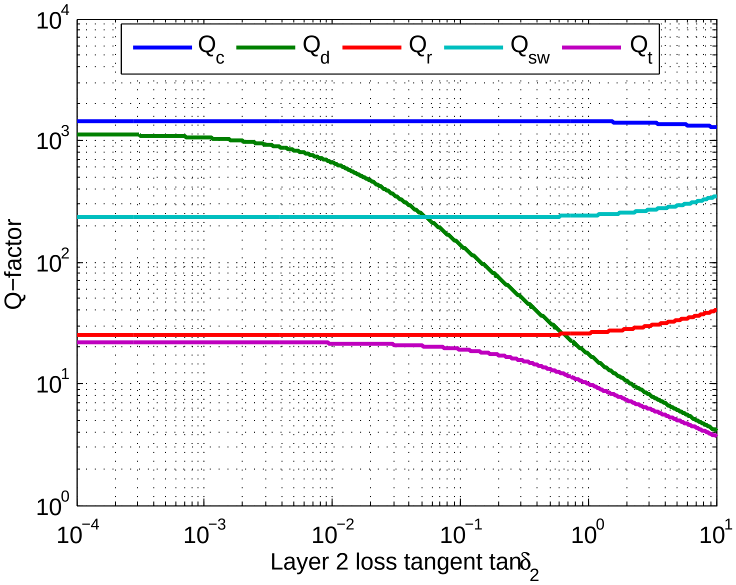

Figure 2.13 Calculated contributions to the total Q-factor Q_t as a function of sample layer loss tangent $\tan\delta_2$. The patch parameters used in this example are: $W = L = 10$ mm, $h_1 = 1$ mm, $\epsilon_{r1} = \epsilon_{r2} = 2$, $\tan\delta_1 = 0.001$, and $t = 35.56$ µm.

2.7 References

[1] R. B. Dybal, “Radar Cross Section Measurements”, *Proc. IEEE*, Vol. 75, No. 4, pp. 498-516, Apr. 1987.

[2] G. D. Dester, E. J. Rothwell and M. J. Havrilla, “An Extrapolation Method for Improving Waveguide Probe Material Characterization Accuracy”, *IEEE Microwave and Wireless Components Lett.*, Vol. 20, No. 5, pp. 298-300, May 2010.

[3] G. D. Dester, E. J. Rothwell and M. J. Havrilla, “Two-Iris Method for the Electromagnetic Characterization of Conductor-Backed Absorbing Materials Using an Open-Ended Waveguide Probe”, *IEEE Trans. Instrum. Meas.*, Vol. 60, No. 4, pp. 1037-1044, Apr. 2012.

[4] J. Mazierska, J. Krupka, M. Bialkowski and M. V. Jacob, “Microwave Resonators and Their Use as Measurement Instruments and Sensors”, *Proc. 3rd IEEE Int. Workshop Electron. Design*, Pages: 5, 2009.

[5] A. K. Verma, Nasimuddin and A. S. Omar, “Microstrip resonator sensors for determination of complex permittivity of materials in sheet, liquid and paste forms”, *IEEE Proc.-Microw. Antennas. Propag.*, Vol. 152, No. 1, pp. 47-54, Feb. 2005.

[6] C. A. Balanis, *Advanced Engineering Electromagnetics*, New York, NY, USA: John Wiley & Sons, 1989.

[7] I. J. Bahl and R. Garg, “Simple and Accurate Formulas for a Microstrip with Finite Strip Thickness”, *Proc. IEEE*, Vol. 65, No. 11, pp. 1611-1612, Nov. 1977.

[8] A. K. Verma and Z. Rostamy, “Resonant Frequency of Uncovered and Covered Rectangular Microstrip Patch Using Modified Wolff Model”, *IEEE Trans. Microw. Theory Techn.*, Vol. 41, No. 1, pp. 109-116, Jan. 1993.

[9] E. Yamashita, “Variational Methods for the Analysis of Microstrip-Like Transmission Lines”, *IEEE Trans. Microw. Theory Techn.*, Vol. 16, No. 8, pp. 529-535, Aug. 1968.

[10] R. Garg and S. A. Long, “Resonant Frequency of Electrically Thick Rectangular Microstrip Antennas”, *Electron. Lett.*, Vol. 23, No. 21, pp. 1149-1150, Oct. 1987.

[11] H. A. Wheeler, “Transmission-Line Properties of Parallel Strips Separated by a Dielectric Sheet”, *IEEE Trans. Microw. Theory Techn.*, Vol. 13, No. 2, pp. 172-185, Mar. 1965.

[12] E. Hammerstad and Ø. Jensen, “Accurate Models for Microstrip Computer-Aided Design”, *1980 MTT-S International Symposium Digest*, pp. 407-409, Washington, DC, USA, 28-30 May 1980.

[13] A. K. Verma, Nasimuddin, V. Tyagi and D. Chakraverty, “Input Impedance of Probe-fed Multilayer Rectangular Microstrip Patch Antenna using the Modified Wolff Model”, *Microw. Opt. Techn. Let.*, Vol. 31, No. 3, Nov. 2001.

[14] A. K. Verma and A. Bhupal, “Conductor Loss of Multilayer Microstrip Line Using the Single-Layer Reduction Formulation”, *Microw. Opt. Techn. Let.*, Vol. 19, No. 1, pp. 20-24, Sep. 1998.

[15] R. Garg, P. Bhartia, I. Bahl and A. Ittipiboon, *Microstrip antenna design handbook*, Norwood, MA, USA: Artech House, 2001.

[16] A. K. Verma and A. Bhupal, “Dielectric Loss of Multilayer Microstrip Line”, *Microw. Opt. Techn. Let.*, Vol. 17, No. 6, pp. 368-370, Apr. 1998.

[17] C. A. Balanis, *Antenna Theory: Analysis and Design*, 3rd ed., Hoboken, NJ, USA: Wiley Interscience, 2005.

[18] M. N. O. Sadiku, *Elements of Electromagnetics*, 5th ed., Oxford University Press, 2010.

[19] A. K. Verma and Nasimuddin, “Determination of Dielectric Constant and Loss-Tangent of Substrate Sheet Using Microstrip Patch Resonator”, *Microw. Opt. Techn. Let.*, Vol. 35, No. 2, pp. 175-179, Nov. 2002.

[20] J. Havil, *Gamma: Exploring Euler’s Constant*, Princeton University Press, Princeton, New Jersey, USA, 2003.

[21] D. M. Pozar, “Rigorous Closed-form Expressions for the Surface Wave Loss of Printed Antennas”, *Electron. Lett.*, Vol. 26, No. 13, pp. 954-956, Jun. 1990.

[22] P. Perlmutter, S. Shtrikman and D. Treves, “Electric Surface Current Model for the Analysis of Microstrip Antennas with Application to Rectangular Elements”, *IEEE Trans. Antennas Propag.*, Vol. 33, No. 3, pp. 301-311, Mar. 1985.

CHAPTER 3. PATCH ANTENNA SENSOR DESIGN AND LABORATORY MEASUREMENTS

3.1 Introduction

In the previous chapter, a model was presented that takes the parameters of a patch antenna sensor and sample parameters, including complex permittivity, as inputs and computes the expected resonant frequency. Some example calculations were plotted for generic patch designs and the expected results were discussed. In this chapter, a physical patch antenna sensor is designed based upon specified criteria, signal feeding issues are discussed, an unconventional method of measuring the resonant frequency is discussed and developed, a physical antenna is realized and tested with a variety of well-characterized microwave materials to validate the model and design, and future work is proposed, including a potential permittivity inversion scheme.

3.2 Patch design parameters

The physical patch design presented in this chapter was the guided by two main criteria. Simulations employing the model presented in Chapter 2 and finite element simulations using Ansys HFSS were used to guide the selection of appropriate materials and dimensions in the process of designing the patch. The two main criteria guiding the patch design were:

- *Resonant frequency of the sensor should fall within the X-band (8-12 GHz).* Given that any sample placed near the sensor will reduce its natural (isolated) resonant frequency, this means that the air resonant frequency should be as near to the high end of the X-band (i.e. 12 GHz) as possible so that, for many samples, the resonant frequency of the sensor will stay within the band limits. This also means that some materials with relatively high permittivity ($\epsilon_r > 10$, approximately) may cause the resonant frequency of the patch to shift into the C-band (4-8 GHz)—this is a limitation on the types of materials that can be characterized accurately with any particular patch.

- *Patch dimensions should be relatively small.* A single patch is useful in that it can be scanned over a sample surface with a resultant resolution that depends upon the step size of the scanning instrument. One drawback of scanning with a single patch is, however, the time required and dependence upon mechanical methods to move the patch. A linear array of patches could reduce the need for physical patch movement in one dimension, with the drawback being that the lateral resolution is then limited by the inter-patch spacing and patch size. Given that the desired resonant frequency of the isolated patch is around 12 GHz, based on the first criterion given above, and that the patch antenna is a half-wave resonator, one can expect the patch width/length dimension to be around 12.5 mm in free space. The presence of the substrate and distance from the groundplane will act to reduce the wavelength and the required patch dimensions.

One choice that was made initially was the substrate material and height, so as to leave only the patch width/length dimension for tuning. For highest possible resonant frequencies, the substrate permittivity should be as low as possible. Since air ($\epsilon_r = 1$) is impractical and foams ($1 < \epsilon_r < 2$) are not rigid enough to support a thin conductive patch, a rigid, low-loss substrate with low permittivity was preferred. Although Taconic TLY-5 is not the lowest possible permittivity substrate, it was chosen for the final patch design as it is a rigid and durable woven glass-fiber laminate with real permittivity $\epsilon_r = 2.20$ and loss tangent $\tan\delta = 0.0009$ at 10 GHz. In terms of substrate height, a thicker substrate decreases the resonant frequency, which forces the patch dimensions to decrease to maintain a high resonant frequency. However, there are practical problems associated with reducing the patch dimensions, such as how to accurately feed an extremely small patch. On the other hand, a very thin substrate would force the patch dimensions to be much larger than desired, if the resonant frequency is to remain at around 12 GHz. In the end, a standard microwave substrate height was chosen: 1.143 mm (45 mil). A standard copper thickness of 35.56 μm (1 oz) was also chosen, as it was

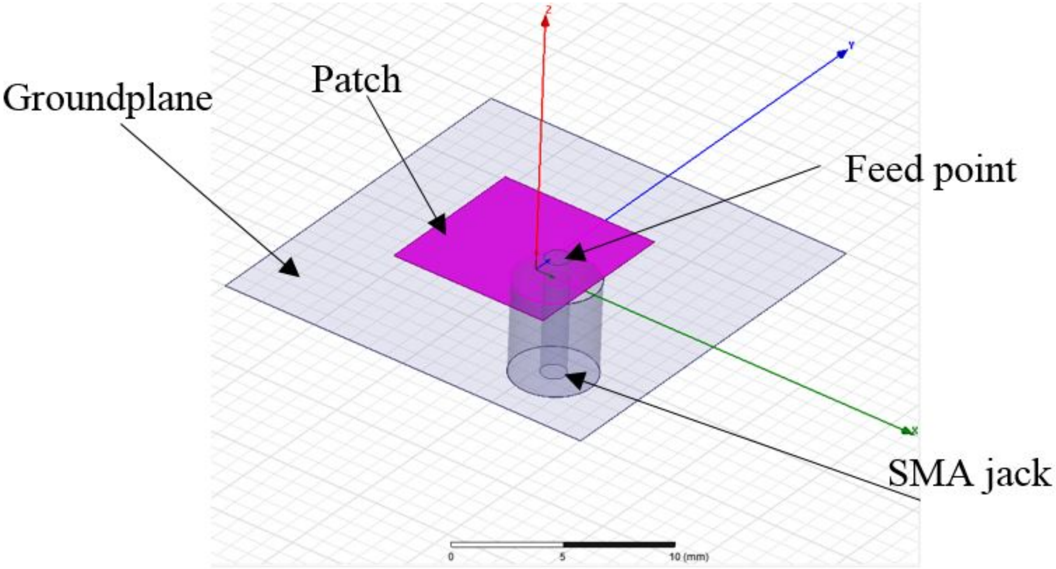

Figure 3.1 Initial HFSS simulation setup showing the basic component locations.

presumed thick enough to maintain durability during contact measurements and did not force the sample to liftoff too far from the substrate.

Based upon an initial HFSS simulation of various patch dimensions and feeding locations, the setup of which is shown in Figure 3.1, the patch width/length that provided the minimum reflection and highest frequency using the substrate parameters described above was $W = L = 7.5$ mm with a probe feed inset distance from the edge of 2.15 mm. A square patch was chosen for simplicity, there being no particular advantage in a rectangular patch for this application. In the simulation, an SMA connector feed was designed with standard materials and dimensions. However, as will be discussed in the next section, it was found that the minimum in the reflection coefficient $|S_{11}|$ is not a true determinant of resonant frequency due to the feeding structure influence on input impedance.

3.3 Resonant frequency measurements

For experimental measurement of the patch antenna sensor parameters in a laboratory or field environment, a vector network analyzer (VNA) is used. The VNA computes the scattering parameters (S-parameters), which are ratios of reflected and transmitted voltage amplitudes at network ports. Since the patch antenna sensor is a one-port network, the only measurable

S-parameter is the S_{11} parameter, which is also the input reflection coefficient when viewed from the source cable toward the antenna port. The S_{11} parameter is defined as

$$S_{11}(f) = \Gamma_{in}(f) = \frac{Z_{in}(f) - Z_c}{Z_{in}(f) + Z_c}, \tag{3.1}$$

where Z_{in} is the input impedance of the antenna and Z_c is the characteristic impedance of the measurement cable (typically 50 Ω). The ratio in (3.1) is often expressed in units of decibels (dB) such that

$$S_{11,\mathrm{dB}}(f) = 20 \log \left| \frac{Z_{in}(f) - Z_c}{Z_{in}(f) + Z_c} \right|, \tag{3.2}$$

where the coefficient 20 (as opposed to 10) converts a voltage ratio to a power ratio ($P \sim V^2$) by a logarithm property. From (3.1) and (3.2), it is apparent that minimum reflection occurs when $Z_{in} = Z_c$, resulting in a reflection of zero (or tending to $-\infty$ dB). This condition will occur at, or near, the resonant frequency since the input impedance of the antenna will dramatically change near this frequency. Specifically, at resonance, the input resistance will be maximum and the input reactance will be zero (realistically, near zero). Therefore, the measured resonant frequency is defined in this research as

$$f_r = f[R_{in} = max(R_{in})] \tag{3.3}$$

Far from the resonant frequency, the input resistance will be near zero, but at resonance the input resistance will not necessarily be Z_c, which means that somewhere near the resonant frequency there will be a matched load and maximum power transfer, which is measurable on the VNA as $\min[|S_{11}(f)|]$.

Conversely, if the VNA provides only S-parameters and the input impedance is desired, (3.1) can be rearranged to yield

$$Z_{\mathrm{in}} = Z_{11} = Z_c \frac{1 + S_{11}}{1 - S_{11}}, \tag{3.4}$$

which is valid if a one-port network is in use.

3.3.1 Input impedance model

The input impedance is a complex quantity that is decomposed into real and imaginary components as $Z_{in}(f) = R_{in}(f) + jX_{in}(f)$, where $R_{in}(f)$ is the resistance (proportional to energy lost to the circuit), $X_{in}(f)$ is the reactance (proportional to energy stored in the circuit) and j is the imaginary unit. The resistance arises from various sources of loss in an antenna circuit—conductor losses, dielectric losses, radiation losses, surface wave losses, etc.—while the reactance arises from competing sources of electric and magnetic energy, such as inductance and capacitance of the various structures in the circuit. At resonance the resistance will rise to a maximum due to maximum radiation while the reactance will, ideally, drop to zero since all energy is being lost at that frequency.

In [1] the input impedance for a patch antenna sensor is defined as

$$Z_{in}(f) = \frac{R_{res}}{1 + Q_t^2 \left(\frac{f}{f_r} - \frac{f_r}{f}\right)^2} + j \left[X_L(f) - \frac{R_{res} Q_t \left(\frac{f}{f_r} - \frac{f_r}{f}\right)}{1 + Q_t^2 \left(\frac{f}{f_r} - \frac{f_r}{f}\right)^2} \right], \tag{3.5}$$

where R_{res} is the maximum resistance that occurs at the resonant frequency f_r, X_L is the inductive reactance due to the feeding probe, and Q_t is the total quality (Q-) factor of the patch, which contains the loss sources mentioned above and was described in greater detail in Section 2.5[1]. This equation is essentially a transfer function for a parallel RLC circuit. The maximum resistance is defined as

$$R_{res} = R_{edge} \cos^2\left(\frac{\pi y_0}{L}\right) = \frac{Q_t h_1}{\pi f_r \epsilon'_{r,dyn} \epsilon_0 W L} \cos^2\left(\frac{\pi y_0}{L}\right), \tag{3.6}$$

where R_{edge} is the input resistance if the patch is fed from its edge, y_0 is the feedpoint distance from the edge along the length L, assuming the feedpoint is centered along the width W, and $\epsilon'_{r,dyn}$ is the real dynamic permittivity of the system, including the substrate and all sample layers, discussed in the previous chapter. A top view of the patch showing the feeding location is shown in Figure 3.2.

The feeding probe inductive reactance is defined as

$$X_L(f) = \frac{\eta_0 f h_1}{c} \ln\left(\frac{c}{\pi f d_0 \sqrt{\epsilon'_{req}}}\right), \tag{3.7}$$

where $\eta_0 = \sqrt{\mu_0/\epsilon_0} \approx 120\pi\ \Omega$ is the characteristic impedance of free space, d_0 is the diameter of the feed probe, and ϵ'_{req} is the real static equivalent permittivity between the patch and the

---

[1] The inverse of Q_t yields the effective loss tangent of the entire system.

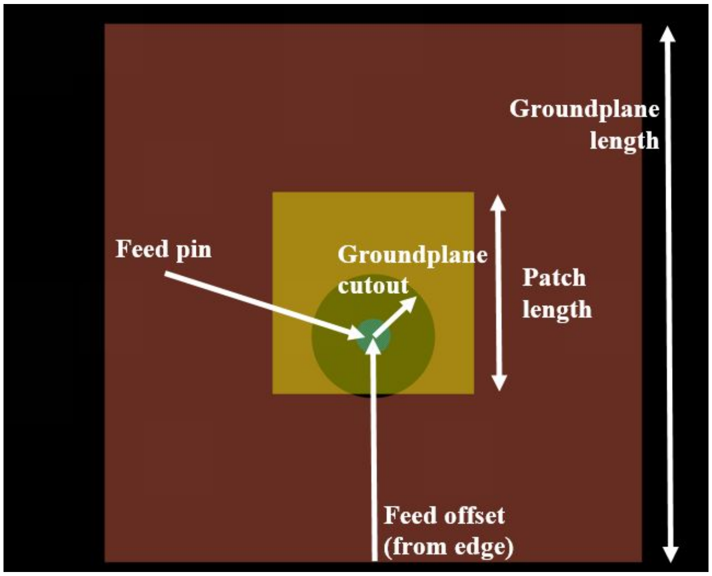

Figure 3.2 Top view of a patch fabrication design showing the feed offset from the edge, feed pin, and groundplane cutout radius.

groundplane, a function of the substrate and layer permittivities, which will be discussed in the next section.

As can be seen in (3.5), at the resonant frequency $f = f_r$, the input impedance simplifies to $Z_{in} = R_{res} + jX_L$. Ideally, Z_{in} should be purely real at resonance, however, the necessary presence of the probe feed contributes some inductive reactance irrespective of the resonant frequency. Thus, S_{11} may not be at a minimum at exactly the resonant frequency, which leaves the resistance being the better indicator of the true resonant frequency. These effects are illustrated in Figures 3.3 and 3.4. A method for finding the true resonant frequency and Q-factor will be presented in Section 3.4.2.

3.4 Experimental validation

In this section, final patch antenna sensor designs are presented for optimization via experimental decision, a method for determining true resonant frequency and Q-factor is presented, the final optimized designed is tested on a variety of materials to validate the model, and results are discussed.

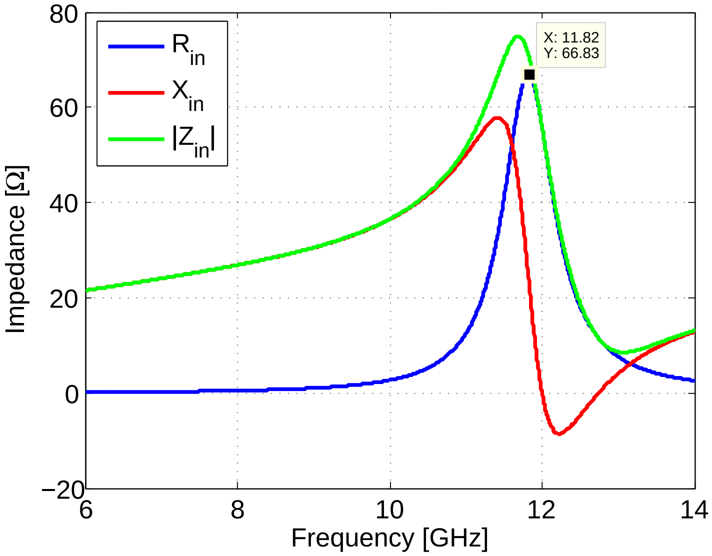

Figure 3.3 Calculated input impedance of a patch antenna sensor. The resistive component reaches a maximum, and the rate of change of the reactance is maximal, at the true resonant frequency. Ideally, the reactance is zero at resonance, but the feed structure contributes some significant inductive reactance that positively offsets the reactance curve from the $X_{in} = 0$ line. The parameters used in this example are $W = L = 7.5$ mm, $\epsilon_{r1} = 2.2$, $h_1 = 1.143$ mm, $\tan\delta_1 = 0.0009$, $d_0 = 1.27$ mm and $y_0 = 2.15$ mm.

3.4.1 Final design parameters

The final design parameters for the patch antenna sensor are given in Table 3.1. As discussed in Section 3.2, the feed offset from the edge that produced the best reflection results according to that calculation was 2.15 mm. However, using the input impedance model above for calculating the optimal feed offset to achieve a resonance resistance of 50 Ω, the optimal offset was determined as 2.885 mm. Another system variable was the effect of the ground-plane cutout radius, which was found to reduce the resonant frequency as the cutout radius increased. The radius needed to be larger than the feeding pin radius to prevent short circuits, and since the minimum manufacturer circular etching tolerance was 0.8 mm, this was chosen as one possible cutout radius. Another was approximately twice the radius of the feeding pin, or 1.2 mm. A matrix of the four potential feeding parameters is given in Table 3.2.

On all four fabricated patch antenna sensors, a circular hole with radius 0.635 mm was drilled through the substrate and patch layers at the specified feedpoint location. A 50 Ω SMA

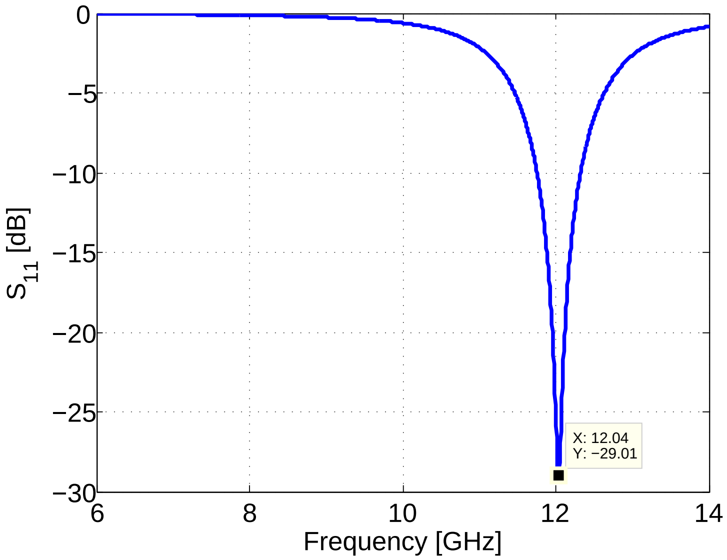

Figure 3.4 Calculated reflection coefficient of the patch antenna sensor showing minimal reflection at a frequency near, but not equal to, the true resonant frequency. This offset is due to the feed inductive reactance. The parameters used in this example are $W = L = 7.5$ mm, $\epsilon_{r1} = 2.2$, $h_1 = 1.143$ mm, $\tan\delta_1 = 0.0009$, $d_0 = 1.27$ mm and $y_0 = 2.15$ mm.

female jack with protruding feeding pin, as shown in Figure 3.5, was then connected to the sensor, with the pin soldered to the patch layer and the outer connector casing soldered to the groundplane layer. Prior to soldering the pin to the patch, the top portion of the pin was removed and filed away to be just below the surface of the patch once fully inserted. After soldering the patch connection, a fine-grit sandpaper was used to file away the majority of the protruding solder to yield a flat surface with minimal profile. The solder profile was checked under microscope and had a thickness of less than 20 μm. A photo of the final patch connection is shown in Figure 3.6.

3.4.2 Determining true resonant frequency and Q-factor

As mentioned in Section 3.3.1, finding the minimum in S_{11} is not the true locator of the natural resonant frequency due to the series addition of the feeding inductance to the parallel RLC circuit of the patch antenna sensor itself. The minimum in S_{11} is simply the point of maximum power transfer and is the point at which the sensor is most efficiently operated as

Table 3.1 Final patch parameters.

Parameter	**Dimension**	**Units**
Patch width W	7.5	mm
Patch length L	7.5	mm
Patch thickness t	35.56	µm
Patch conductivity σ	58	MS/m
Groundplane width/length	20	mm
Substrate height h_1 1.143	mm	
Substrate permittivity ϵ'_{r1}	2.20	
Substrate loss tangent $\tan\delta_1$	0.0009	
Feeding pin radius	0.635	mm
Air resonant frequency f_r	11.82	GHz
Air Q-factor Q_t	14.55	

Table 3.2 Final feed offset and groundplane cutout radius dimensions, each with two options for a total of four combinations.

Parameter	**Option 1**	**Option 2**
Feed offset (mm)	2.15	2.885
Groundplane cutout radius (mm)	0.8	1.2

an antenna for long range energy transmission. This also means that the looking for the -3 dB (half-power) points on the S_{11} plot is not a good indicator of the sensor's bandwidth or Q-factor. According to (3.5), the real part R_{in} has three parameters: magnitude R_{res}, resonant frequency f_r and Q-factor Q_t, where R_{res} is achieved at f_r. This means that searching for the maximum in R_{in} is the best indicator of the true resonant frequency. The imaginary part X_{in} also contains these same parameters, where, in this case, the imaginary part of the RLC circuit goes to zero at f_r. The drawback here, though, is that the total imaginary part does not go to zero at resonance because of X_L. Finding the inflection point in $X_{in}(f)$ could also reveal where f_r occurs.

Measured Q-factor for a parallel RLC circuit is generally determined from

$$Q = \frac{f_r}{\Delta f}, \tag{3.8}$$

which is also known as the fractional bandwidth. The bandwidth Δf is usually the width between the half-power points on a plot of S_{11} versus frequency, however, direct use of S_{11} data interpretation has been ruled out as discussed above. The bandwidth definition itself is not

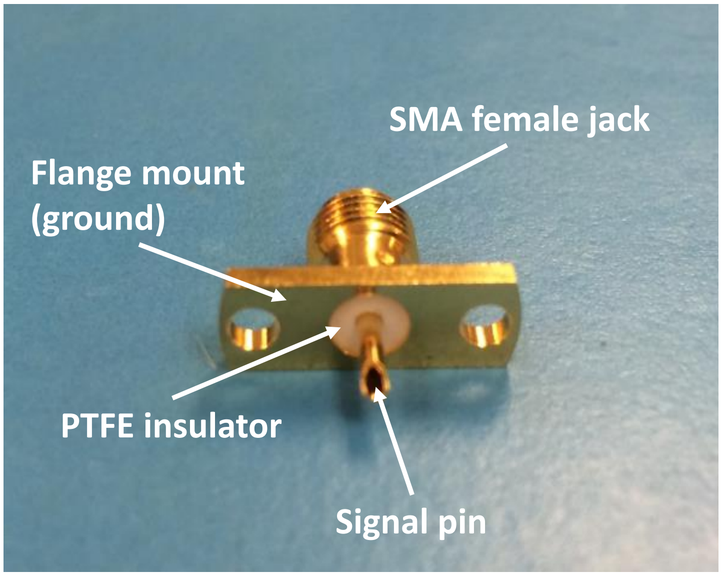

Figure 3.5 SMA jack connector used to make electrical connection between the patch antenna sensor and VNA cable. The female jack mates with the SMA cable, the flange mount is soldered to the sensor groundplane, the signal pin is fed through the substrate and soldered to the patch, with the polytetrafluoroethylene (PTFE) layer insulating the signal pin from the grounded flange mount.

well-agreed upon within the RF community and is up to interpretation depending upon design requirements. In [2] the definition of bandwidth is avoided altogether, with the defintion of Q for an antenna as

$$Q \approx \frac{\omega_r}{2R_{in}(\omega_r)} \left| \frac{d}{d\omega} Z_{in}(\omega_r) \right|, \tag{3.9}$$

where ω is the angular frequency and $R_{in}(\omega_r) = R_{res}$. This definition, however, requires information from both the real and imaginary parts of input impedance, which could lead to more uncertainty in a physical and/or noisy measurement.

Another approach is to define normalized R_{in} as a transfer function, where the bandwidth occurs between the two points on the resistance slope where the amplitude has fallen to $1/\sqrt{2} \approx 0.707$. These points correspond to half-power points when the amplitude is squared to yield the power transfer function. This definition deviates from the RLC transfer function in Section 3.3.1 since the measured Q would be higher than the Q as defined in the model. In fact, it is found from (3.5) that in order to utilize the fractional bandwidth definition of Q in (3.8), the corresponding two points on the resistance slope occur approximately where the amplitude has

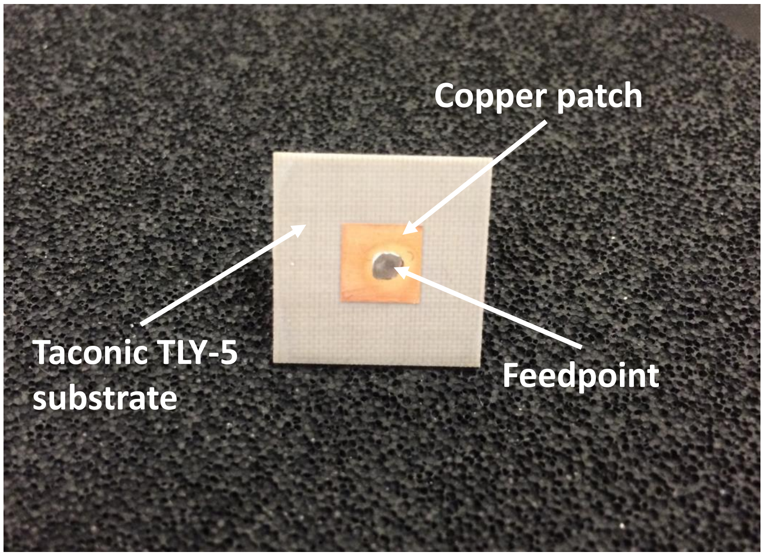

Figure 3.6 Top view of the soldered patch connection to the SMA jack. The Taconic TLY-5 substrate both structurally supports the patch above the groundplane and controls the natural resonant frequency of the sensor. The SMA signal pin feeds through the substrate and is soldered to the feedpoint of the copper patch.

fallen to half of the maximum. This scheme is also known as full width at half maximum (FWHM) in signal processing.

For example, in Figure 3.7, the resonant frequency and Q-factor of an arbitrary antenna and/or sample are calculated from the model to be 9.69 GHz and 20.47, respectively. By finding the two approximate half-maximum amplitude points that occur on either side of the resonant frequency, and by using (3.8), the measured Q-factor is computed as 20.62, a difference of only 0.73 %, where some uncertainty can be attributed to the discrete measurement resolution. This interpretation has been tested and found to hold with numerous other simulated patch and sample configurations. Therefore, a good approximation of Q in (3.8) is given here as

$$Q = \frac{f_r}{f_+|_{(R_{in}=0.5R_{res})} - f_-|_{(R_{in}=0.5R_{res})}}. \tag{3.10}$$

The determination of resonant frequency and Q-factor from actual measured data requires further algorithmic processing due to factors such as noise, peak skewness or ill-formation, and the presence of higher order resonances and feedpoint resonances. The latter is exhibited in

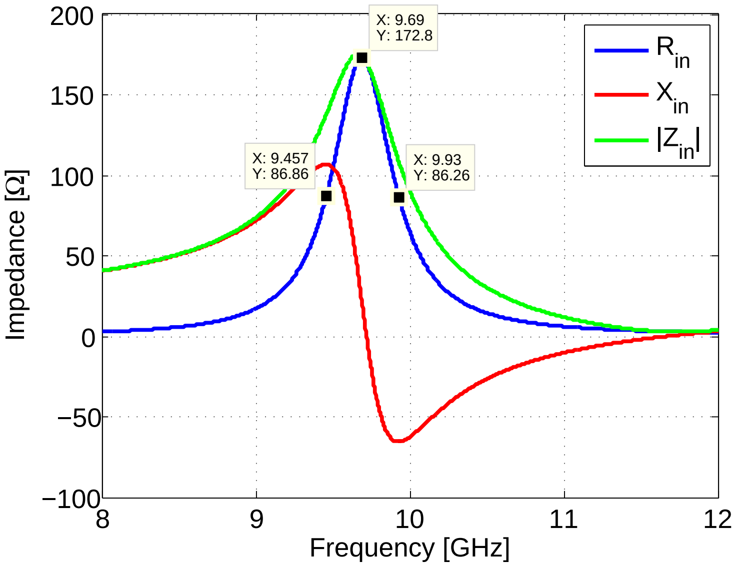

Figure 3.7 Calculated input impedance for an arbitrary patch antenna sensor showing the resonant frequency at 9.69 GHz, maximum resistance at resonance, and approximate half-maximum amplitude points.

Figure 3.8, where the presence of a high-resistance resonance is readily visible and contrasts sharply with the resonant frequency of the patch sensor due to a sample. The feedpoint resonance occurs due to the interaction between the inductive feeding pin (as it is carrying a current) and the capacitive gap (because there is a voltage differential separated by a dielectric material) between the pin and the groundplane (or SMA connector jacket), essentially acting as a cylindrical resonator as apparent by the high Q-factor. The high-impedance of this peak also has a very high reflection, so it is not typically visible on S_{11} measurements, but is something that must be accounted for when attempting to automate an algorithmic search for the patch sensor resonant frequency. The feedpoint resonance peak does not shift to lower resonant frequencies with increasing sample permittivity, leading to the potential problem that high-permittivity samples can shift the patch sensor resonance such that it overlaps with this high-impedance resonance and becomes convoluted with it.

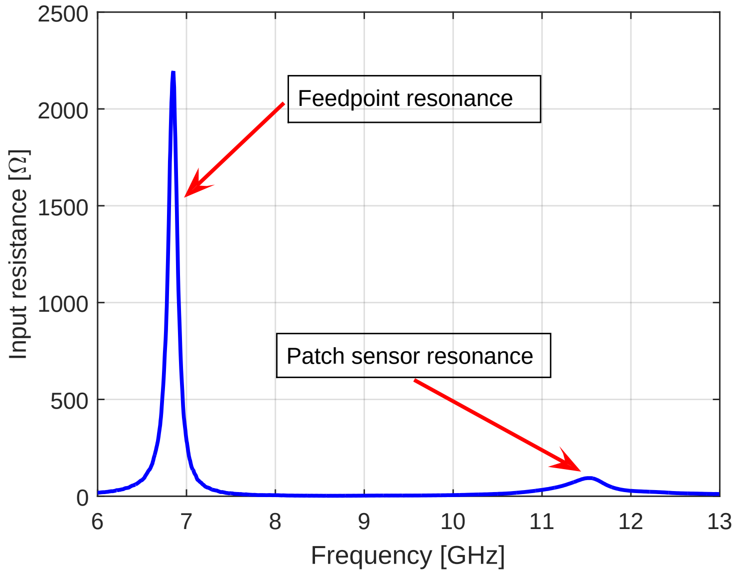

Figure 3.8 Measured input resistance showing a high-resistance resonance due to the resonation of the feedpoint and the lower-resistance patch sensor resonance due to a sample.

Noisy data and peak skewness are also problematic for data interpretation, as the input resistance, in theory, follows the smooth parallel RLC impedance distribution in (3.5), with an amplitude (R_{res}), mean (f_r) and shape factor (Q). This means that, if a parallel RLC impedance curve could be fitted to the data, especially the upper half of an observed peak in the data, the resonant frequency and Q-factor could be accurately and quickly obtained.

Before data can be fitted, however, several operations must first take place. The first is to smooth the data to prevent unwanted peaks from appearing during peak detection. The smoothing in this work was a moving average filter with a 2 % data span, which acts as a low-pass filter to remove outliers but with a small enough span to retain potential resonance peaks. The next operation is to search for these peaks, which can be done by searching for minima in the second derivative of R_{in} or by using a built-in peak-searching function, such as MATLAB's `findpeaks()` function, which quickly returns an array of indices where local maxima occur in the data. Without smoothing, the length of this array can be quite long, but with smoothing a short array of approximately 5-10 elements is returned. Next, the true resonant peak must be determined, which, for the chosen antenna, is typically the largest peak under 300 Ω, where anything larger is typically the feedpoint resonance. The true resonant frequency for a sample measurement must also be less than or equal to the measured air resonant frequency ($\approx$ 12 GHz) for the lowest order mode (or dominant mode) as higher frequency (higher order) modes can interfere with the searching algorithm. This potential interference is easily eliminated by fixing the upper limit of the applied frequency sweep to a reasonable value just beyond the expected dominant mode air resonant frequency. Finally, a window of data must be selected around the detected peak to fit the RLC curve with minimal error. In this work, a span of about 8.6 % (or 70 data points on either side of the peak, out of 1601 total points) was determined to be sufficient for a variety of samples.

In summary, the resonant frequency and Q-factor measurement procedure was performed as follows:

1. Smooth the data with a moving average filter and 2 % data point span.
2. Search for peaks, choose the largest peak under 300 Ω.
3. Select a total data span window of 8.6 %, centered around the peak index.
4. Perform RLC fitting on selected data; measured f_r and Q_t values are returned.

These parameters may be adjusted if the results do not appear close to the expected results. This is especially true for the data window span, which has a significant influence on measured Q_t, particularly when data are noisy and skewed.

3.4.3 Materials

For the purposes of validating the model and assessing the performance of the fabricated patch antenna sensor, a variety of well-characterized and uncharacterized materials were analyzed using the sensor, the measured spectrum, and the data analysis algorithm presented above. The materials with independently-measured properties, listed in Tables 3.3 and 3.4, were divided into pure sheet samples without metal backplanes and samples that included affixed copper backplanes. The uncharacterized materials, Table 3.5 had no permanent af-

Table 3.3 Rogers materials with no metal backplane. All dielectric parameters (provided by the manufacturer) are given at 10 GHz.

Material	**Thickness (mm)**	ϵ_r'	$\tan\delta$
RO3003	0.508 ± 0.03	3.00 ± 0.04	0.0010
RT/duroid 5870	1.575 ± 0.05	2.33 ± 0.02	0.0012
RT/duroid 5880	1.575 ± 0.05	2.20 ± 0.02	0.0009
TMM3	0.508 ± 0.04	3.27 ± 0.03	0.0020
TMM4	0.508 ± 0.04	4.50 ± 0.05	0.0020
TMM6	0.635 ± 0.04	6.00 ± 0.08	0.0023
TMM10	0.635 ± 0.04	9.20 ± 0.2	0.0022
TMM10i	0.635 ± 0.04	9.80 ± 0.2	0.0020

Table 3.4 Rogers materials with metal backplane composed of 35.56 μm thickness of copper. All dielectric parameters (provided by the manufacturer) are given at 10 GHz.

Material	**Thickness (mm)**	ϵ_r'	$\tan\delta$
RT/duroid 5870	1.575 ± 0.05	2.33 ± 0.02	0.0012
RT/duroid 5880	1.575 ± 0.05	2.20 ± 0.02	0.0009
TMM3	6.350 ± 0.04	3.27 ± 0.03	0.0020
TMM4	6.350 ± 0.04	4.50 ± 0.05	0.0020
TMM6	6.350 ± 0.04	6.00 ± 0.08	0.0023
TMM10	6.350 ± 0.04	9.20 ± 0.2	0.0022
TMM10i	6.350 ± 0.04	9.80 ± 0.2	0.0020

fixed backplane, but an aluminum plate was clamped in contact with the sample to act as a backplane.

The backplane and non-backplane materials in Tables 3.3 and 3.4 are the same apart from the addition of RO3003 in Table 3.3 and the different thicknesses for most of the materials. Rogers RO3000-series materials are low-loss, ceramic-filled polytetrafluoroethylene (PTFE) composites designed for microwave circuit functionality up to 77 GHz [3]. Rogers RT/duroid

Table 3.5 Uncharacterized materials and measured thicknesses. These samples do not have a metal backplane.

Material	**Thickness (mm)**
Glass-fiber composite	1.27
FR4/G-10	3.18
Nylon	3.18
Glass	1.80

5870/5880 are glass microfiber-reinforced PTFE composites with low loss up to and beyond the Ku-band (12-18 GHz) [4]. Rogers TMM-series materials are ceramic, hydrocarbon, thermoset polymer-matrix composites designed with a coefficient of thermal expansion to match that of copper [5]. For the uncharacterized materials, FR4 and nylon were chosen in order to analyze their significant lossiness at lower frequencies [6] [7]. For example, both FR4 and nylon have a loss tangent of approximately 0.02 at 1 MHz. Glass and glass-fiber composite also have a wide-range of permittivity values that are useful for an exemplar analysis of a material with unknown properties. Photos of the samples listed in Tables 3.3, 3.4 and 3.5 are shown in Figures 3.9, 3.10 and 3.11, respectively.

3.4.4 Experimental procedure

The setup for the experimental procedure is shown in Figures 3.12 and 3.13. A test fixture comprised a vertically-mobile base, metal vertical and horizontal support structure and a polycarbonate tube to hold the SMA cable between the VNA and patch antenna sensor in a fixed position during calibration and testing. The base has a hand crank to make repeatable and precise liftoff adjustments by lifting the cable test fixture above the sample. The adjustments were measured by a digital micrometer with 1 µm uncertainty. The 30-cm-long polycarbonate tube forces the cable into a straight path above the SMA/sensor connection to maintain the sensor's parallel orientation to the sample surface; nylon screws are situated around the tube to make fine tuning adjustments on the straightness of the cable. The cable is a 121.9-cm-long, 50 Ω coaxial cable capable of operation up to 18 GHz.

The VNA is an Anritsu 37347C capable of operation between 40 MHz and 20 GHz. Before measurements could begin, the VNA had to be calibrated by selecting the frequency range (1601 points across 6-13 GHz in this work) and placing open, short and broadband 50 Ω terminations at the end of the cable. A desktop computer graphical user interface (GUI) program was created using National Instruments LabVIEW to communicate with, command and transfer data from the VNA in S-parameter form, which was converted to complex impedance in the GUI.

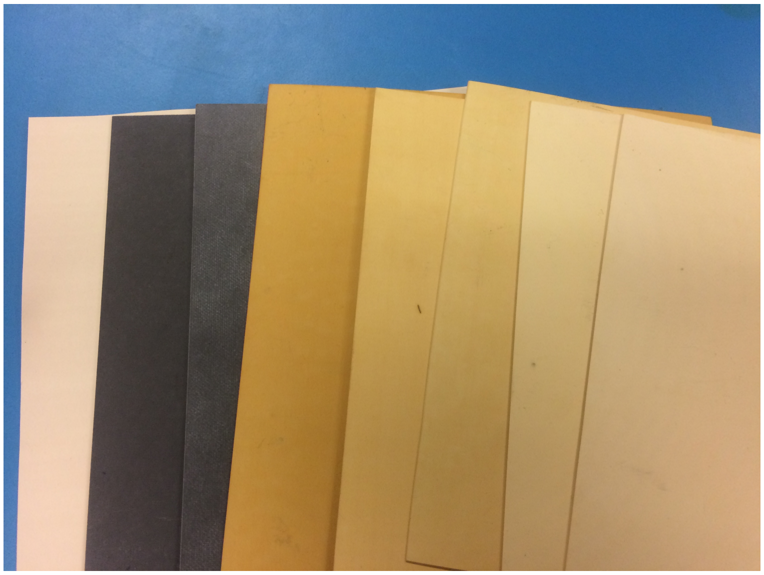

Figure 3.9 Rogers microwave materials with no metal backplane and properties listed in Table 3.4. From left to right: RO3003, RT/d5870, RT/d5880, TMM3, TMM4, TMM6, TMM10 and TMM10i.

Figure 3.10 Rogers microwave materials with metal backplane and properties listed in Table 3.4. From top left to bottom right: RT/d5870, RT/d5880, TMM3, TMM4, TMM6, TMM10 and TMM10i.

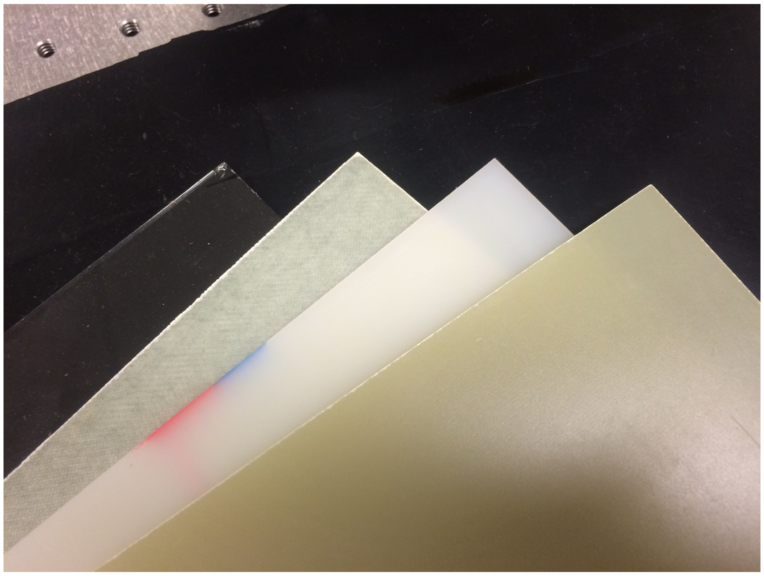

Figure 3.11 Uncharacterized materials with properties listed in Table 3.5. From left to right: glass (transparent), glass-fiber composite, nylon and FR4.

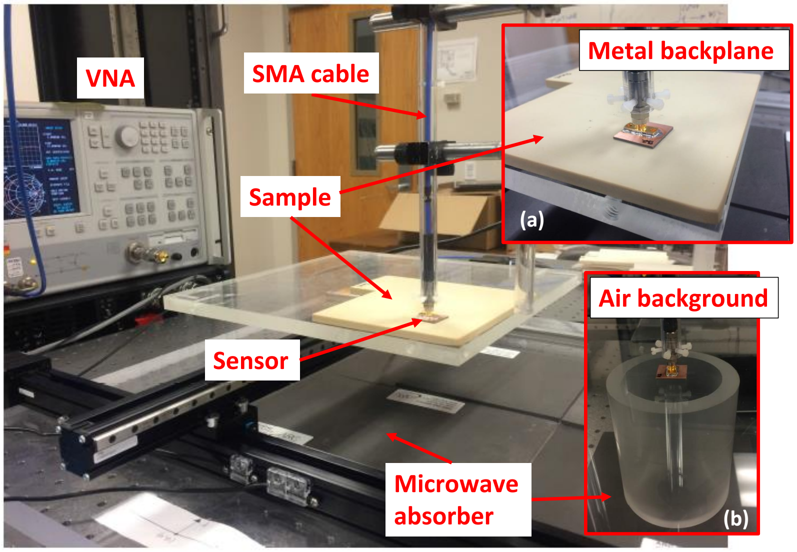

Figure 3.12 Experimental setup showing VNA, SMA cable, patch antenna sensor, sample and microwave absorbing material. Inset (a) shows the setup for samples with affixed or external metal backplanes (backplane not shown in the inset). An acrylic table supports the sample, with the metal backplane situated between the table and the sample. Inset (b) shows the setup for samples with no metal backplane. A hollow acrylic tube supports the sample and a microwave absorbing material is placed at the bottom of the cylinder to simulate an air background.

For measurements on samples with metal backplanes (either affixed or external), as shown in Figure 3.12(a), the sample was placed atop an acrylic table such that the backplane was situated between the sample and acrylic, thus restricting near-fields to the sample and away from the table. For samples without a backplane, a hollow acrylic tube supported the sample and a microwave absorbing material was placed at the opposite end of the tube. With the sensor situated above the center of the tube, the setup approximately simulated an air background, Figure 3.12(b). For contact measurements, the sensor was lowered from a small height above the sample using the hand crank on the base until the fixture encountered some slight upward resistance and no air gap was visible between the patch and sample. For measurements with a fixed liftoff between the patch and the sample, the sensor was brought from a contact position until the desired liftoff value was achieved on the micrometer, as shown in Figure 3.13.

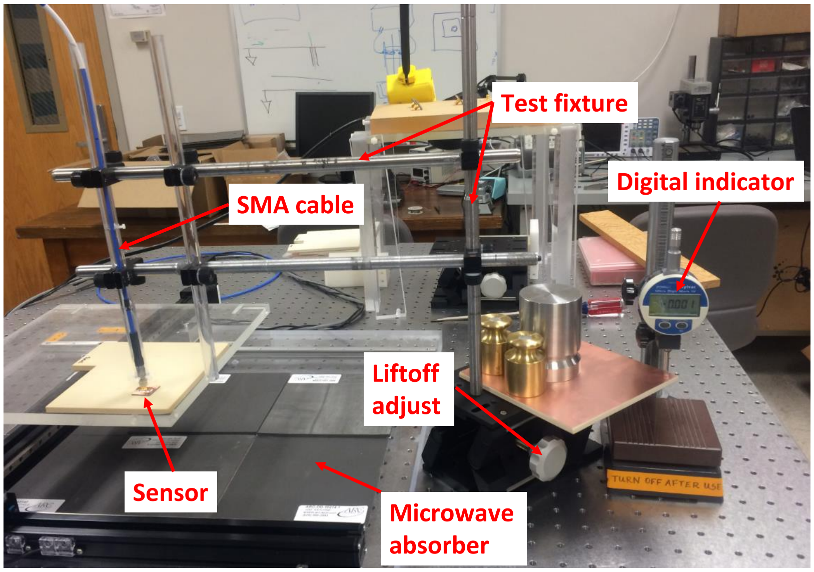

Figure 3.13 Experimental setup showing test fixture with polycarbonate tube containing SMA cable, patch antenna sensor, sample, microwave absorbing material, vertically–mobile test fixture base, liftoff adjustment crank and micrometer with digital indicator for liftofff measurement.

Multilayer combinations of the characterized materials were also analyzed using the patch sensor. For multilayer samples including the backplane, the backplane sample acted as the final layer while the non-backplane layers were placed between the backplane sample and the sensor. Multilayer samples are only constructed from compression contact, meaning there is some air between layers.

3.4.5 Results

In this section are presented the final measured resonant frequency and Q-factor results in tabulated form for all samples, in comparison with the values obtained using the model presented in Chapter 2 and values calculated using HFSS. The sensor, whose parameters are given in Table 3.2, had a feed offset of 2.15 mm from the edge and a groundplane cutout radius of 0.8 mm, as this design produced the least error with between measured and expected results.

In Tables 3.6 3.7, calculated and measured resonant frequencies and Q-factors, respectively, are given for 1-layer, 2-layer and 3-layer combinations of the air-backed materials backed by air listed in Table 3.3. Calculated and measured liftoff resonant frequencies and Q-factors for single layers of the same air-backed materials are listed in Tables 3.8 and 3.9, respectively. In Tables 3.10 and 3.11, calculated and measured resonant frequencies and Q-factors, respectively, are given for 1-layer, 2-layer and 3-layer combinations of both the backplane samples listed in Table 3.4 and the non-backplane samples listed in Table 3.3. In the case of 1-layer samples, only the backplane samples are used. For 2- and 3-layer samples, the backplane layer is one furthest from the patch while the non-backplane layers are placed between the patch and backplane layers. Calculated and measured liftoff resonant frequencies and Q-factors for single layers of the same metal-backed samples are listed in Tables 3.12 and 3.13, respectively. Measured resonant frequencies and Q-factors for uncharacterized materials are listed in Table 3.14. Percentage errors for each sample listed in all tables are given relative to the model results for the purposes of validating the model. An average absolute value percent error is given at the bottom of each table. The results are discussed in the following section.

Table 3.6 Calculated, measured and simulated resonant frequencies for the patch sensor in contact with non-backplane samples with air background. For multilayer samples, the sample materials are listed in order away from the patch surface. Mean errors listed are means of absolute values.

Material layers	f_r **model (GHz)**	f_r **meas. (GHz)**	f_r **HFSS (GHz)**	**Error meas. (%)**	**Error HFSS (%)**
Air	11.82	12.00	12.32	1.5	4.2
RO3003	11.22	11.50	11.59	2.5	3.3
RT/d5870	11.03	11.27	11.42	2.2	3.5
RT/d5880	11.09	11.34	11.52	2.3	3.9
TMM3	11.17	11.37	11.49	1.8	2.9
TMM4	10.94	10.99	11.16	0.5	2.0
TMM6	10.57	10.44	10.60	-1.2	0.3
TMM10	10.15	9.81	9.89	-3.3	-2.6
TMM10i	10.08	9.86	9.78	-2.2	-3.0
TMM10i—RT/d5870	9.80	9.52	9.39	-2.9	-4.2
TMM10—RT/d5880	9.88	9.49	9.52	-3.9	-3.6
TMM6—TMM3	10.34	10.12	10.29	-2.1	-0.5
TMM3—TMM6	10.52	10.45	10.65	-0.7	1.2
RT/d5880—TMM10	10.65	10.46	10.89	-1.8	2.3
RT/d5870—TMM10i	10.57	10.41	10.73	-1.5	1.5
TMM10i—TMM6—TMM3	9.54	8.80	8.95	-7.8	-6.2
TMM6—TMM10i—TMM3	9.66	8.85	9.12	-8.4	-5.6
TMM6—TMM4—TMM10	9.73	9.31	9.18	-4.3	-5.7
TMM4—TMM6—TMM10	9.81	9.30	9.49	-5.2	-3.3
Mean 1-layer error:				1.9	2.8
Mean 2-layer error:				2.1	2.2
Mean 3-layer error:				6.4	5.2

Table 3.7 Calculated, measured and simulated Q-factors for the patch sensor in contact with non-backplane samples with air background. For multilayer samples, the sample materials are listed in order away from the patch surface. Mean errors listed are means of absolute values.

Material layers	Q_t **model**	Q_t **meas.**	Q_t **HFSS**	**Error meas.** (%)	**Error HFSS** (%)
Air	14.55	17.64	15.00	21	3.1
RO3003	16.26	18.67	15.00	15	-7.7
RT/d5870	16.90	13.55	12.37	-20	-27
RT/d5880	16.70	15.55	12.55	-6.9	-25
TMM3	16.43	16.44	15.03	0.1	-8.5
TMM4	17.18	11.90	15.20	-31	-12
TMM6	18.54	12.50	15.13	-33	-18
TMM10	20.31	15.58	16.32	-23	-20
TMM10i	20.63	15.12	16.63	-27	-19
TMM10i—RT/d5870	22.02	13.35	14.04	-39	-36
TMM10—RT/d5880	21.59	13.67	13.93	-37	-35
TMM6—TMM3	19.47	12.57	13.94	-35	-28
TMM3—TMM6	18.72	10.12	11.60	-46	-38
RT/d5880—TMM10	18.24	6.86	3.84	-62	-79
RT/d5870—TMM10i	18.56	6.25	3.37	-66	-82
TMM10i—TMM6—TMM3	23.40	11.03	13.43	-53	-43
TMM6—TMM10i—TMM3	22.70	9.35	10.69	-59	-53
TMM6—TMM4—TMM10	22.35	8.16	9.17	-63	-59
TMM4—TMM6—TMM10	21.92	7.96	8.62	-64	-61
Mean 1-layer error:				20	16
Mean 2-layer error:				48	50
Mean 3-layer error:				60	54

Table 3.8 Calculated, measured and simulated resonant frequencies for the patch sensor at 0.75 mm liftoff distance from non-backplane samples with air background. Mean errors listed are means of absolute values.

Material layers	f_r **model (GHz)**	f_r **meas. (GHz)**	f_r **HFSS (GHz)**	**Error meas. (%)**	**Error HFSS (%)**
RO3003	11.61	11.78	12.11	1.5	4.3
RT/d5870	11.49	11.60	12.04	1.0	4.8
RT/d5880	11.51	11.66	12.06	1.3	4.8
TMM3	11.59	11.73	12.08	1.2	4.2
TMM4	11.51	11.59	11.98	0.7	4.1
TMM6	11.35	11.20	11.76	-1.3	3.6
TMM10	11.18	10.77	11.38	-3.7	1.8
TMM10i	11.15	10.91	11.30	-2.2	1.3
Mean error:				1.6	3.6

Table 3.9 Calculated, measured and simulated Q-factors for the patch sensor at 0.75 mm liftoff distance from non-backplane samples with air background. Mean errors listed are means of absolute values.

Material layers	Q_t **model**	Q_t **meas.**	Q_t **HFSS**	**Error meas. (%)**	**Error HFSS (%)**
RO3003	15.12	17.63	13.05	17	-14
RT/d5870	15.47	15.38	10.20	-0.6	-34
RT/d5880	15.40	15.35	10.56	-0.3	-31
TMM3	15.17	17.75	12.82	17	-15
TMM4	15.41	17.72	11.86	15	-23
TMM6	15.86	12.48	9.61	-21	-39
TMM10	16.40	9.39	7.42	-43	-55
TMM10i	16.49	8.43	7.15	-49	-57
Mean error:				20	34

Table 3.10 Calculated, measured and simulated resonant frequencies for the patch sensor in contact with samples with backplanes behind the layer(s). For multilayer samples, the sample materials are listed in order away from the patch surface, with the affixed backplane sample being the last and the non-backplane layers in between. Mean errors listed are means of absolute values.

Material layers	f_r **model (GHz)**	f_r **meas. (GHz)**	f_r **HFSS (GHz)**	**Error meas. (%)**	**Error HFSS (%)**
RT/d5870	8.12	8.98	9.24	11	14
RT/d5880	8.25	9.02	9.20	9.3	12
TMM3	9.39	10.05	10.12	7.0	7.8
TMM4	8.65	9.07	9.28	4.9	7.3
TMM6	7.97	8.29	8.53	4.0	7.0
TMM10	6.94	6.95	6.47	0.1	-6.8
TMM10i	6.79	6.98	6.31	2.8	-7.1
TMM10i—RT/d5870	7.68	8.16	8.22	6.3	7.0
TMM10—RT/d5880	7.82	8.17	8.20	4.5	4.9
TMM6—TMM3	9.03	9.39	9.42	4.0	4.3
TMM3—TMM6	8.43	8.04	8.49	-4.6	0.7
RT/d5880—TMM10	9.17	8.65	9.15	-5.7	-0.2
RT/d5870—TMM10i	9.03	8.60	8.99	-4.8	-0.4
TMM10i—TMM6—TMM3	8.20	7.97	8.34	-2.8	1.7
TMM6—TMM10i—TMM3	8.32	8.02	8.40	-3.6	1.0
TMM6—TMM4—TMM10	7.64	8.28	7.27	8.4	-4.8
TMM4—TMM6—TMM10	7.72	8.29	7.29	7.4	-5.6
Mean 1-layer error:				5.5	8.7
Mean 2-layer error:				5.0	2.9
Mean 3-layer error:				5.5	3.3

Table 3.11 Calculated and measured Q-factors for the patch sensor in contact with samples with backplanes behind the layer(s). For multilayer samples, the sample materials are listed in order away from the patch surface, with the affixed backplane sample being the last and the non-backplane layers in between. Mean errors listed are means of absolute values.

Material layers	Q_t **model**	Q_t **meas.**	Q_t **HFSS**	**Error meas. (%)**	**Error HFSS (%)**
RT/d5870	22.66	12.33	20.12	-46	-11
RT/d5880	21.82	11.36	19.47	-48	-11
TMM3	22.87	45.15	25.04	97	9.5
TMM4	27.68	20.56	14.37	-26	-48
TMM6	33.55	25.88	12.16	-23	-64
TMM10	46.77	19.43	15.03	-58	-68
TMM10i	49.54	15.12	14.19	-69	-71
TMM10i—RT/d5870	29.94	12.31	10.25	-59	-66
TMM10—RT/d5880	28.67	11.53	8.53	-60	-70
TMM6—TMM3	25.25	40.02	19.29	58	-24
TMM3—TMM6	29.54	21.10	14.65	-29	-50
RT/d5880—TMM10	24.65	12.95	13.11	-47	-47
RT/d5870—TMM10i	25.88	12.35	13.60	-52	-47
TMM10i—TMM6—TMM3	31.93	22.54	13.43	-29	-58
TMM6—TMM10i—TMM3	30.78	23.12	13.80	-25	-55
TMM6—TMM4—TMM10	37.62	18.49	12.48	-51	-67
TMM4—TMM6—TMM10	36.72	17.85	12.36	-51	-66
Mean 1-layer error:				53	40
Mean 2-layer error:				51	51
Mean 3-layer error:				39	62

Table 3.12 Calculated, measured and simulated resonant frequencies for the patch sensor at 0.75 mm liftoff distance from metal-backed samples. Mean errors listed are means of absolute values.

Material layers	f_r **model (GHz)**	f_r **meas. (GHz)**	f_r **HFSS (GHz)**	**Error meas. (%)**	**Error HFSS (%)**
RT/d5870	9.92	9.76	9.53	-1.6	-3.9
RT/d5880	9.97	9.81	9.58	-1.6	-3.9
TMM3	10.52	10.32	10.54	-1.9	0.2
TMM4	10.20	9.16	9.60	-10	-5.9
TMM6	9.93	8.11	8.70	-18	-12
TMM10	9.57	9.42	9.78	-1.6	2.2
TMM10i	9.52	9.48	9.62	-0.4	1.1
Mean error:				5.1	4.2

Table 3.13 Calculated, measured and simulated Q-factors for the patch sensor at 0.75 mm liftoff distance from backplane samples. Mean errors listed are means of absolute values.

Material layers	Q_t **model**	Q_t **meas.**	Q_t **HFSS**	**Error meas. (%)**	**Error HFSS (%)**
RT/d5870	16.92	10.52	12.91	-38	-24
RT/d5880	16.74	12.11	12.47	-28	-26
TMM3	17.92	21.94	29.78	22	66
TMM4	19.22	15.31	18.12	-20	-5.7
TMM6	20.44	17.63	15.84	-14	-23
TMM10	22.28	7.74	15.74	-65	-29
TMM10i	22.56	10.08	15.30	-55	-32
Mean error:				35	26

Table 3.14 Measured resonant frequencies and Q-factors for the patch sensor in contact with the uncharacterized materials. Data for measurements with and without a backplane are given.

	Without backplane		With backplane	
Material layers	f_r **(GHz)**	Q_t	f_r **(GHz)**	Q_t
Glass-fiber composite	10.58	11.66	8.84	18.53
FR4/G-10	10.54	3.79	7.43	9.00
Nylon	10.69	6.96	7.88	9.73
Glass	9.32	8.71	7.90	24.95

3.4.6 Discussion

The measured resonant frequency data, as presented in the previous section, agree very well with the model, with an overall mean error for contact measurements of 4.4 %. In general, the error tends to increase with more sample layers, and reasons for this are: (1) more layers bring compounded uncertainties, due to permittivity and height variations in each layer, and (2) the layers are only in contact with one another and not bonded, leaving possible slight air gaps between them. Although air is in high dielectric contrast with the materials examined in this work, the gaps are of such low height that their influence should be minimal, and indeed the measured frequencies are not consistently greater than the calculated frequencies, which means that it is not likely to be the dominant source of error. However, the samples without a backplane, which were very thin in comparison to most of those with backplanes, had a slightly curved surface that increased the difficulty in achieving good contact between layers and between the layers and the sensor. It is also observed that the presence of the backplane increases the mean error for all samples (e.g. the 1-layer error for contact non-backplane samples 1.9 %, while that for 1-layer contact backplane samples was 6.4 %), and this may be attributed to several factors. In these experiments, the backplane was not actually grounded—being a very good conductor at a floating electric potential relative to the VNA ground or circuit reference point.

Values for measured Q-factor, on the other hand, were off from the model by a significant percentage error and do not appear to significantly vary between samples with and without a backplane, although the single-layer non-backplane sample had a significantly smaller error than the others (20 %, compared to 39-60 % for the remaining backplane and non-backplane 1-, 2- and 3-layer samples). There are two possible sources of error in this case: (1) the Q-factor model is inaccurate, and/or (2) the data fitting algorithm and Q-factor computation lacks robustness. If the model is the source of error, it is most likely due to the calculation of Q_r, which, being the dominant loss contributor, is the most likely contributor to the error. If the measurement algorithm is the source of error, then it is most likely due either to the chosen method of computing measured Q_t as opposed to the large variety of other methods, or to the size of the data window to fit the parallel RLC impedance curve. This was indeed observed to be an issue, as varying the window size could significantly reduce the error for one sample but increase it for another. As all samples were given the same window size for the sake of comparison, all measured values suffered some error due to the window choice. Finally, both the metal backing and substrate have finite length and width dimensions, which are assumed to be infinite in the model. The finite dimensions of these components are chosen to be much larger than the patch dimensions such that the static fringing fields do not interact with the edges. For generated surface-traveling waves from the patch, the finite dimensions of the metal backing and substrate may lead to reflections that interfere with the infinite-length approximation from which Q_r and Q_{sw} are derived, which may account for some of the differences between modeled and measured values. Ascertaining the value of Q_{sw} by measurement may be prohibitively difficult, but in future work, it would prove beneficial to correlate Q_{sw} with the change in resonant frequency as a function of groundplane/substrate dimensions by HFSS simulation, which would also determine the optimal groundplane dimensions for which the infinite groundplane approximation holds true.

Liftoff resonant frequency measurements showed strong agreement with the model while those for Q-factor showed relatively good agreement with the model when compared to the in-contact measurements. The mean resonant frequency error was 3.4 % while the mean Q-factor error was 28 %. The reason for the relatively low error is most likely the reduction of uncertainties that are involved when the patch is in contact with the sample, as the model assumes a physically infinitesimal sheet as the patch with dimensional corrections for a patch of finite thickness. This means that when a physical patch is in contact with a sample, there is an air gap between the substrate and sample, despite there being no air gap between the patch itself and the sample. When a sample is further away, this gap becomes insignificant compared to the liftoff distance. Yet again, however, the metal backing on some of the samples appears to have introduced significant uncertainty, with the mean metal-backed resonant frequency and Q-factor error being 5.1 % and 35 %, respectively, compared to those for the air-backed samples of 1.6 % and 20 %, respectively.

For the uncharacterized samples, one observation that makes intuitive sense is that the addition of the backplane reduces the resonant frequency and increases the Q-factor (due to more energy storage in the electric field) of all samples. The presence of the backplane greatly increases the Q-factor of glass-fiber composite and solid glass due to these samples being the thinnest (storing even more electric energy due to the capacitive effect of the metal backplane). Another observation is that FR4 and nylon, having the exact same thickness, have similar resonant frequencies, with nylon having a slightly higher resonant frequency in both backplane and non-backplane cases. This suggests, intuitively, that FR4 has a slightly higher real permittivity than nylon. However, the extremely low Q-factor of FR4 suggests that it is significantly more lossy than nylon.

Finally, HFSS simulated results showed similar agreement with the model, with an overall resonant frequency mean error of 4.2 % for in-contact samples, while mean Q-factor errors ranged from 16-62 % for in-contact samples. Again, liftoff simulations were in good agreement with the model, with a resonant frequency mean error of 3.9 % and mean Q-factor error of 30 %. In general, HFSS Q-factor results tended to agree better with the measured results rather than the model results. This observation adds weight to the above deduction that the Q-factor model is the primary source of error rather than the measurement algorithm and curve-fitting.

3.5 Sensitivity analysis

Using the final design presented in Section 3.4.1, a study was conducted to determine the resonant frequency and Q-factor sensitivities of the sensor to changes in sample height, real permittivity and loss tangent. Four types of sample structure were modeled, shown in Figure 3.14. Type I is a simple, one-layer sample with an air background. Type II is also a one-layer dielectric, backed with a backplane background. Type III is a two-layer sample with air background, and Type IV is a two-layer sample backed with a backplane. In the study, Types III and IV have subtypes A and B, corresponding to parametric variations the first or second sample layer only (overall Layer 2 and 3), respectively. For the fixed layers, Layer 2 is assumed to be a thin paint layer while Layer 3 is assumed to be a thick glass-fiber layer, each with parameters listed in Table 3.15. The test-piece parameters were selected based upon one potential practical aerospace application of the sensor. The study is separated into two parts: resonant frequency sensitivity to real permittivity changes and Q-factor sensitivity to loss tangent changes.

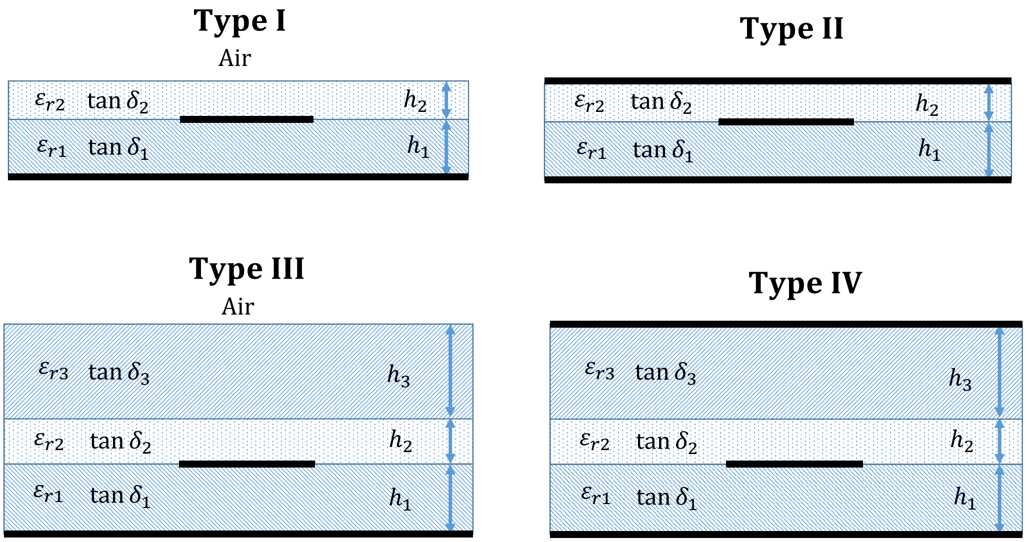

Figure 3.14 Four types of sample layups used in the sensitivity study. Types III and IV have subtypes A and B, where A has a fixed Layer 3 and B has a fixed Layer 2. Fixed layer parameters are given in Table 3.15.

Table 3.15 Fixed layer parameters used in the patch antenna sensor sensitivity study. Sample subtypes A have fixed Layer 3 parameters while sample subtypes B have fixed Layer 2 parameters.

	h (mm)	ϵ_r'	$\tan\delta$
Layer 2	0.127	4.7	0.024
Layer 3	6.35	4.1	0.004

3.5.1 Resonant frequency sensitivity

The resonant frequency variation for Type I in Figure 3.15 shows, for a very thin sample layer, all resonant frequencies starting at the air point value of 11.82 GHz, and separating as the sample increases height, reaching asymptotic values at which the sample appears effectively infinitely thick, at $h_2/h_1 \approx 20$. The resonant frequency is always lower for higher permittivity samples. For Type II, Figure 3.16, very thin samples backed by a backplane cause the resonant frequency to approach zero. The curves separate as the thickness of the dielectric increases, and approach the same thick-sample asymptotes as in Type I, when the sample backplane is sufficiently far away from the sensor. Type III-A samples, Figure 3.17, show a thin-sample convergence for all permittivity values at approximately 9.7 GHz, which is due to Layer 3 dominating the fields for thin Layer 2. As the sample gets thicker, the resonant frequencies for samples with permittivity less than that of Layer 3 while the frequencies for higher permittivity samples decrease, as Layer 2 dominates the near-fields. Type III-B, Figure 3.18 shows another convergence for all permittivity samples at approximately 11.5 GHz, which is the value due solely to the thin Layer 2 backed by air. Type IV-A, Figure 3.19, shows the resonant frequencies converging at 8.8 GHz for thin Layer 2, then separating into thick-layer asymptotes. Of interest is the Layer 2 samples with permittivity higher than that of Layer 3 which briefly decrease before approaching the thick-layer asymptote. This initial decrease is due to the competing influence of the increasing Layer 2 thickness and the increasing distance of the backplane from the patch. Type IV-B, Figure 3.20, shows a similar pattern to Type II, with the exception that the thin Layer 2 forces the backplane to begin at a further distance from the patch, hence beginning at a slightly higher convergent resonant frequency point.

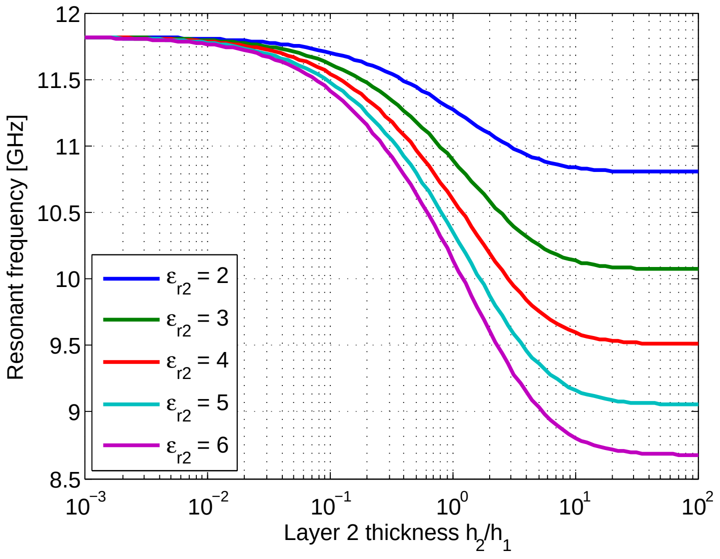

Figure 3.15 Calculated resonant frequency shifts for Type I sample. Fixed layer parameters are given in Table 3.15.

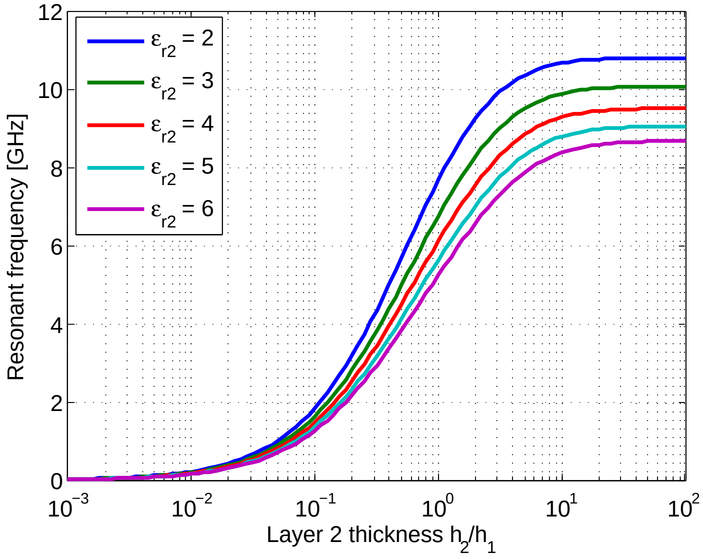

Figure 3.16 Calculated resonant frequency shifts for Type II sample. Fixed layer parameters are given in Table 3.15.

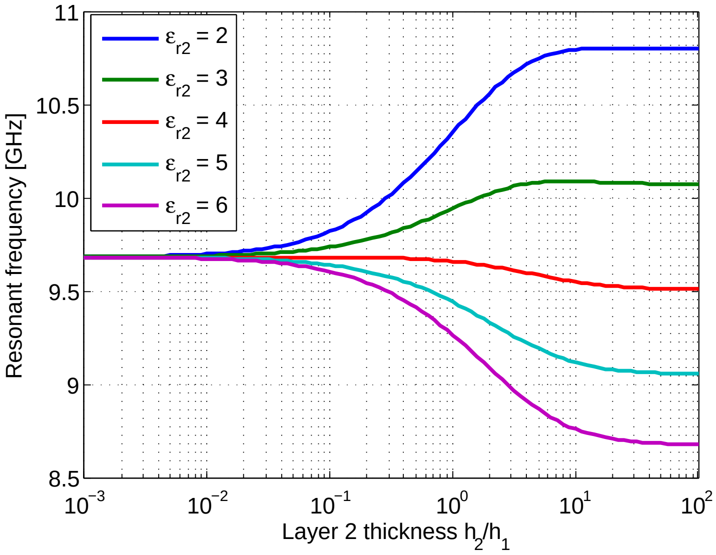

Figure 3.17 Calculated resonant frequency shifts for Type III-A sample. Fixed layer parameters are given in Table 3.15.

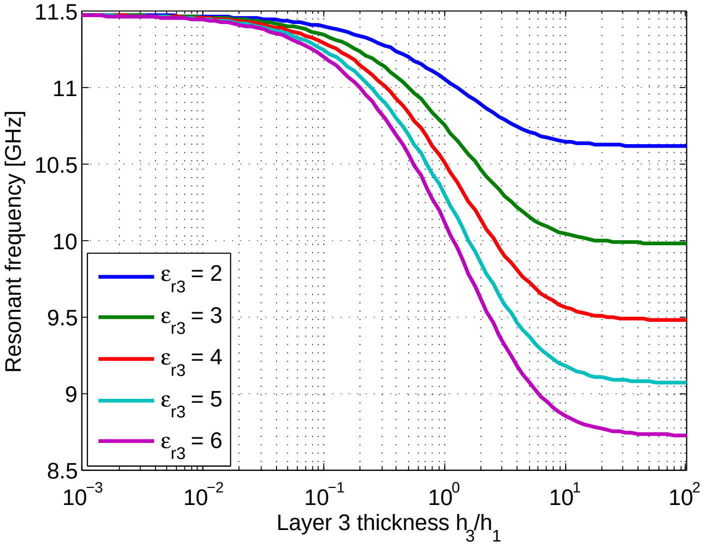

Figure 3.18 Calculated resonant frequency shifts for Type III-B sample. Fixed layer parameters are given in Table 3.15.

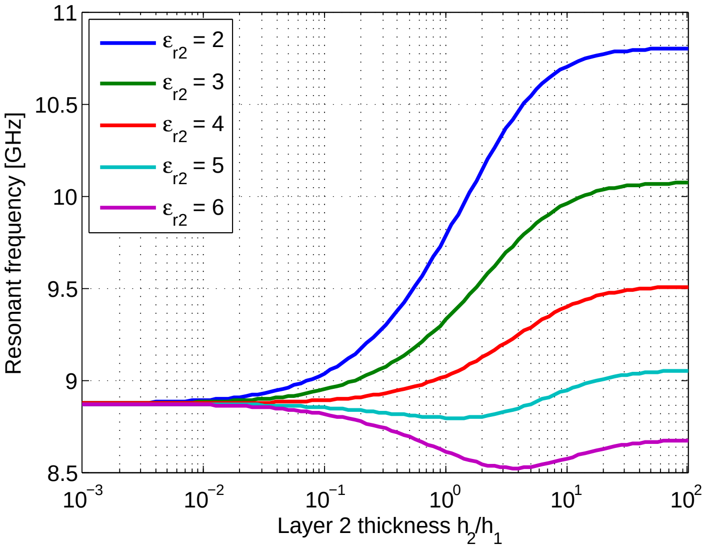

Figure 3.19 Calculated resonant frequency shifts for Type IV-A sample. Fixed layer parameters are given in Table 3.15.

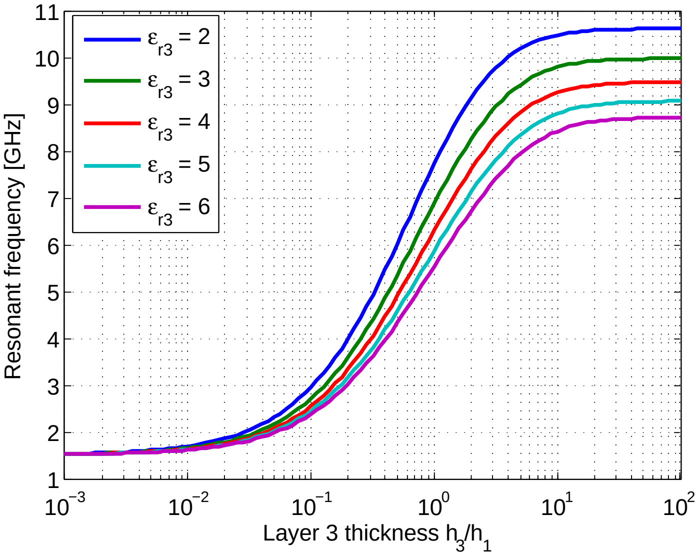

Figure 3.20 Calculated resonant frequency shifts for Type IV-B sample. Fixed layer parameters are given in Table 3.15.

3.5.2 Q-factor sensitivity

The Q-factor shifts due to loss tangent and Layer 2 sample thickness for Type I samples, Figure 3.21, show a thin-sample convergence point that approaches the value for the patch antenna sensor in air. For samples with relatively low loss tangents ($\tan\delta = 0.0001, 0.001, 0.01$), the Q-factor increases with increasing sample thickness, due to more electric energy being stored. For lossier samples, the Q-factor decreases further from the air value for increasing sample thickness, due to more energy being lost. Type II, Figure 3.22, gives rise near-zero Q-factor for thin samples, due to the sample backplane causing the resonant frequency to approach zero. The primary loss in this region is conductor loss, as radiation loss is significantly decreased by the sample backplane being in close proximity. As the Layer 2 thickness approaches a value of $0.2h_1$, the conductor losses decrease and radiation losses begin to increase, before approaching thick-sample asymptotes that are no longer influenced by the backplane. Types III-A and III-B samples, Figures 3.23 and 3.24, again show the common trend of increasing Q for less lossy samples with increasing thickness, while decreasing Q for highly lossy samples. Type IV-A, Figure 3.25 again shows this trend, while Type IV-B, Figure 3.26 shows a similar behavior to Type II, due to the close proximity of the backplane for thin Layer 3 and the thin Layer 2 preventing near-contact of the patch with the backplane.

3.6 Conclusion

In this chapter, the model from Chapter 2 was utilized to develop practical patch antenna sensor for low-conductivity material characterization in the X-band. A new method for resonant frequency and Q-factor determination from measured data was presented with the goal of finding the true values based on impedance data rather than on reflection data. The sensor was tested on a variety of characterized materials, with and without sample backplanes, for model validation, in addition to four uncharacterized materials for analysis of realistically unknown materials. Measured resonant frequencies were found to be in good agreement with the model, while those of measured Q-factor were of moderate agreement, and sources for error in both measurements were discussed.

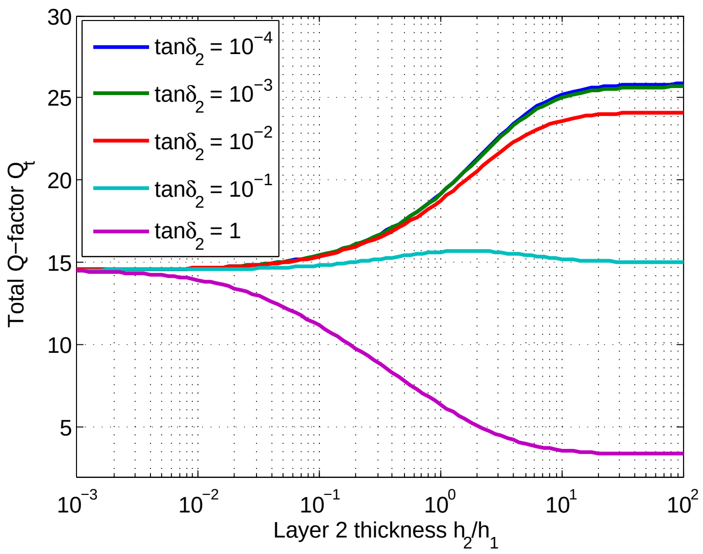

Figure 3.21 Calculated Q-factor shifts for Type I sample. Fixed layer parameters are given in Table 3.15.

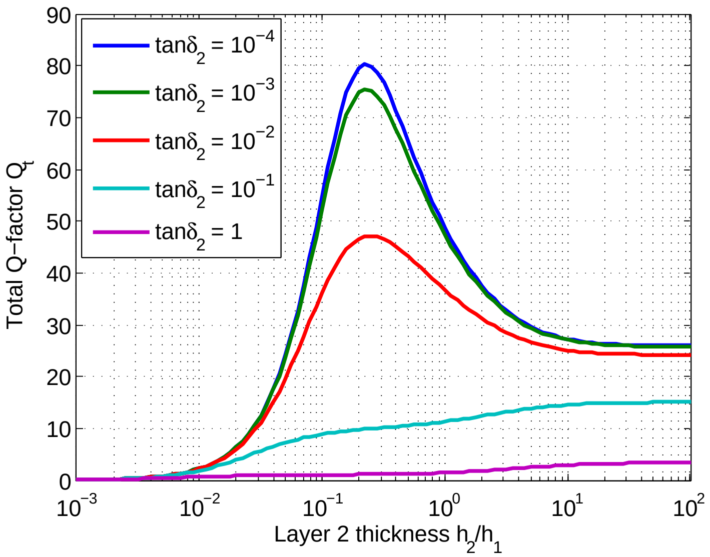

Figure 3.22 Calculated Q-factor shifts for Type II sample. Fixed layer parameters are given in Table 3.15.

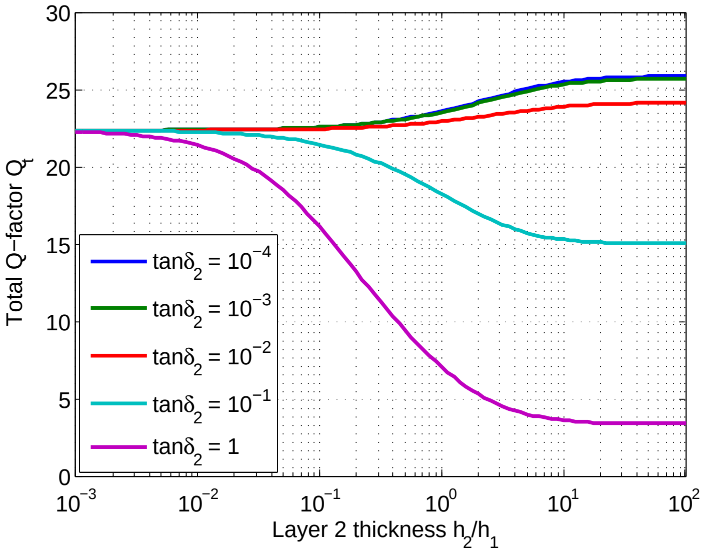

Figure 3.23 Calculated Q-factor shifts for Type III-A sample. Fixed layer parameters are given in Table 3.15.

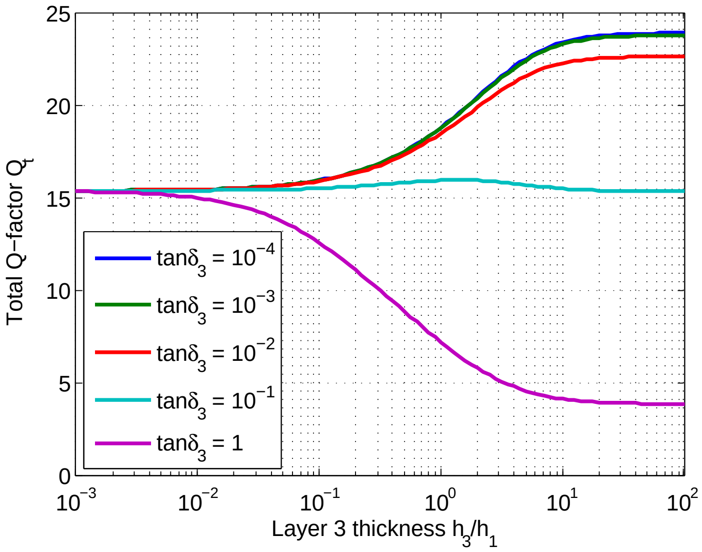

Figure 3.24 Calculated Q-factor shifts for Type III-B sample. Fixed layer parameters are given in Table 3.15.

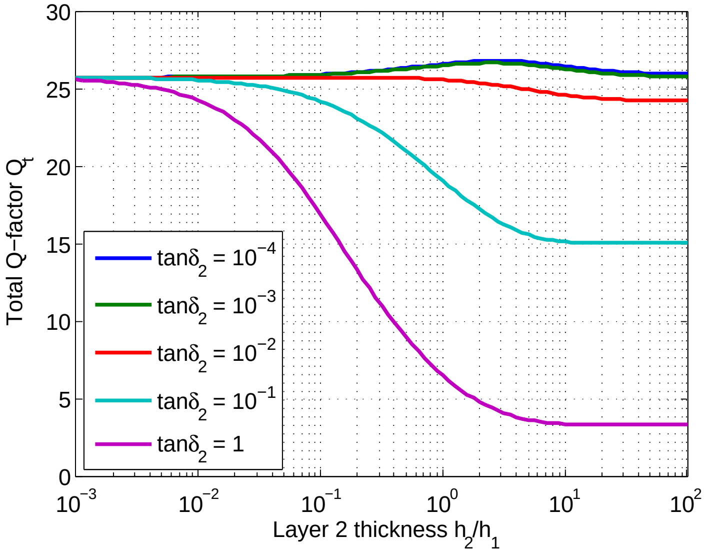

Figure 3.25 Calculated Q-factor shifts for Type IV-A sample. Fixed layer parameters are given in Table 3.15.

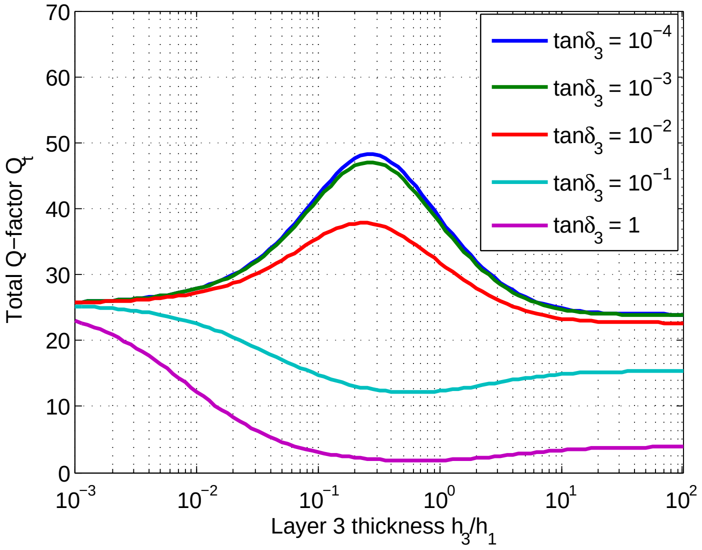

Figure 3.26 Calculated Q-factor shifts for Type IV-B sample. Fixed layer parameters are given in Table 3.15.

3.7 Future work

In future work, the goal is twofold: to develop a robust model that can be used to infer the complex permittivity of an unknown sample layer or the effective permittivity of a multilayer structure as viewed by the patch sensor, and to scan over samples surfaces to create images based on variations in complex permittivity values. Complex permittivity inversion requires knowledge of thickness and permittivity of all sample layers except for the layer of interest. Currently, the observed discrepancy between calculated and measured Q-factor suggests that further work is needed to reduce the discrepancy before reliable inversion can be conducted. One particular challenge with finding the loss tangent of a sample material based upon measurement of the sensor's Q-factor is that the Q-factor is the inverse of a summation of several inverted Q-factor contributions. The uncertainty in all of these contributions must be small in order to calculate an accurate and non-negative value for Q_d, and, hence, an accurate value for the material's loss tangent. In order to obtain accurate Q_d measurements, Q_r must be increased to allow Q_d to at least partially dominate Q_t (i.e. Q_d must be on the same order as Q_r). Samples that would give the lowest Q_r contribution (increasing it) would be those that reduce the radiation conductance G_r and characteristic impedance viewed from the width edge, Z_W, which would be any material that significantly reduces the resonant frequency, by either having a larger thickness or permittivity (or a metal backing). Q_d can only dominate when either the sample loss tangent exceeds $1/Q_r$ or when there is a metal backing to increase Q_r.

The patch antenna sensor may also benefit from a different feeding scheme as well, such as an edge feed rather than a probe feed, because the feeding pin and SMA jack structure add an unwanted resonance that limits the maximum permittivity of a sample that the patch antenna sensor is capable of characterizing. A more robust data measurement algorithm would also provide some relief to this issue.

3.8 Acknowledgments

This work was supported by X-Wave Innovations, Inc. and performed at Iowa State University's Center for Nondestructive Evaluation. Special thanks to Dr. Yi Lu and Mr. Tao Wu, for providing the basis for the model refinement and initial patch designs, and to Mr. Amin Gorji-Bandpy for creating the LabVIEW program that facilitated the measurements.

3.9 References

[1] A. K. Verma, Nasimuddin, V. Tyagi and D. Chakraverty, “Input Impedance of Probe-fed Multilayer Rectangular Microstrip Patch Antenna using the Modified Wolff Model”, *Microw. Opt. Techn. Let.*, Vol. 31, No. 3, Nov. 2001.

[2] A. D. Yaghjian and S. R. Best, “Impedance, Bandwidth, and Q of Antennas”, *IEEE Trans. Antennas Propag.*, Vol. 53, No. 4, pp. 1298-1324, Apr. 2005.

[3] Rogers Corp., “RO3003 Series Circuit Materials”, datasheet 92-130, 2015.

[4] Rogers Corp., “RT/duroid 5870/5880 High Frequency Laminates”, datasheet 92-101, 2015.

[5] Rogers Corp., “TMM Thermoset Microwave Materials”, datasheet 92-108, 2015.

[6] Accurate Plastics, Inc., “Acculam Epoxyglas G10, FR4”, datasheet.

[7] Gilbert Curry Industrial Plastics Co. Ltd., “Ertalon® 6 SA, Extruded Nylon 6”, datasheet, at: <http://www.theplasticshop.co.uk/plastic_technical_data_sheets/extruded_nylon_6_technical_data_sheet.pdf>.

CHAPTER 4. DIELECTROMETRY SENSORS FOR NONDESTRUCTIVE TESTING OF GLASS-FIBER POLYMER MATRIX COMPOSITES

A paper published in *Materials Evaluation*

Robert T. Sheldon and Nicola Bowler

4.1 Introduction

The need to understand the structural integrity of and to nondestructively characterize composite materials has existed for many years, and over that time a multitude of nondestructive testing (NDT) techniques have been developed for this purpose. In the early years, the majority of NDT techniques revolved around the use of qualitative NDT, mainly visual inspection. To characterize materials quantitatively on the surface or within required the use of techniques capable of providing quantitative information such as radiography, ultrasonic testing (UT) and eddy current (eddy current) testing [1]. The wide employment of metals in many structures for energy production (for example, in pipelines), transportation (in ground-based vehicles, water-borne vessels, aircraft and spacecraft) and civil infrastructure (for example, in bridges) means that certain forms of electrical testing are well developed. For example, the time-harmonic eddy current generated by a primary coil is influenced by discontinuities in the conductivity of the test piece, and the primary coil impedance responds accordingly, allowing inspection of surface and subsurface qualities in metals by eddy current NDT [2].

The emergence of polymer-matrix composites (PMCs) in many applications over the past decades, however, presents a need for new inspection techniques. Typical damage such as disbonds, delaminations, porosity and the presence of foreign objects can be well characterized by UT, but monitoring the effects of long-term aging and the prediction of remaining useful life of PMCs is still an open challenge [3][4][5]. Environmental aging, a term used to describe aging due to elevated temperature, humidity, chemical exposure, ionizing and non-ionizing radiation, and so on, generally causes changes in the properties of polymer systemsnot only PMCs but also wire and cable insulation, gaskets, O-rings, sealant, electrical circuit components, and many others. Often, the dielectric properties of these materials change as the material ages, offering the possibility of monitoring the material state by capacitive measurements [6]. Capacitive measurements can be made intermittently using a probing device or may be placed in situ for structural health monitoring [7][8].

In this paper, the ability of certain capacitive sensors to measure thermally-induced changes in a glass-fiber PMC was investigated. In reality, a material is usually exposed to combinations of the aging factors listed in the previous paragraph, but in this paper, thermal aging was selected in order to prove the concept of the sensing technique. Capacitive sensors are ideally suited for characterizing dielectrics such as those listed in the previous paragraph, but since it is often inconvenient or impossible to access both sides of a test piece, the simplest form of capacitor, the parallel-plate capacitor, Figure 4.1(a), is of limited use. For a single-sided inspection, both plates (electrodes) may be coplanar with one another, Figure 4.1(c). A configuration intermediate between these two is shown in Figure 4.1(b). Coplanar capacitive sensors are also termed “fringing electric field” sensors, in that a fringing electric field is projected away, in the out-of-plane direction, from the plane of the gap that exists between two coplanar electrodes of differing potential, as in Figure 4.1(c) [9].

One simple coplanar electrode arrangement is two neighboring rectangular patches [9]. For higher capacitance and sensitivity, rectangular interdigital electrodes may be used [12]. A prior work presented valuable design considerations for concentric coplanar sensors [10]. Samples that are anisotropic, such as fiber-reinforced composites, may benefit from rotationally invariant coplanar sensors, for example, in the form of a simple disc-and-annulus arrangement or as interdigital concentric annuli, shown in Figure 4.2 [7][11]. Interdigital capacitive sensors are advantageous in that interdigitation increases the signal-to-noise ratio. The penetration depth, an arbitrary yet important measure of the strength of the electric field at a subsurface point, can

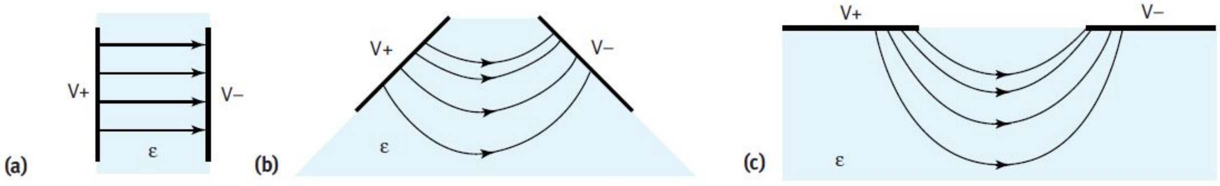

Figure 4.1 Schematic diagram showing transformation: (a) of a parallel plate capacitor; (b) through an intermediate configuration; and (c) to a fringing field capacitor. ϵ denotes the dielectric material and V+/- denotes the electrode voltage and polarity.

be adjusted by manipulating the separation between neighboring electrodes. Increasing spatial periodicity can even be embedded in one sensor to produce a 3D image of the subsurface permittivity, as the sensor is scanned across the surface of the test piece [12].

Glass-fiber PMCs are a good example of low-conductivity, primarily dielectric materials found in structural applications such as aircraft, automobiles, and space and marine vehicles. The environments and conditions to which these structures are subjected require a high degree of performance in terms of specific strength, weight savings, and corrosion resistance [13]. As the name suggests, glass-fiber PMCs are composed of glass fibers, which can be oriented and woven in many different fashions, infused into a polymer matrix that, when cured, bonds to the fibers, leaving the final product with high stiffness and strength [14]. The polymer forming the matrix can be of many types—epoxy, polyimide, and so onbut one that is gaining acceptance in the aerospace industry because of its good retention of dielectric and mechanical properties over a wide range of temperatures, is bismaleimide (BMI). BMI composites can be found in such military applications as F-22 Raptor tactical fighters and are known to provide the highest composite mechanical properties in service in a thermal environment up to 563 K (290 °C) [15].

Dielectric properties of many polymers are known to permanently change when the polymer ages, for example, as noted in prior work, and any such change is capable of yielding a corresponding change in measured capacitance of a capacitive sensor [16]. In this work, concentric interdigital electrodes were chosen as the preferred sensor arrangement so that: first, measured capacitance was independent of the inherent anisotropy in the structure; and second, signal-to-noise ratio was good because of the inherently higher capacitance of the interdigital

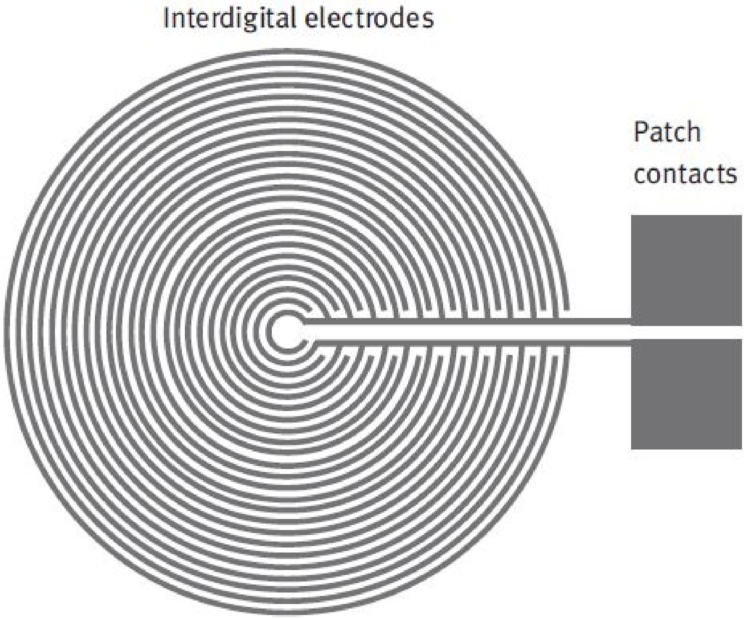

Figure 4.2 Concentric interdigital electrode capacitive sensor. Concentric annuli alternate polarity with adjacent annuli, providing a high signal-to-noise ratio and a capacitance that homogenizes the inherently anisotropic permittivity of glass-fiber polymer–matrix composites.

arrangement, compared with the disc-and-annulus arrangement. Measurements were compared with those of traditional parallel plate electrodes, made on the same samples.

4.2 Technical background

When an electromagnetic field is applied to a medium, there are several possible responses of that medium. In one response, free charges (holes or electrons) within the medium are excited and accelerated in a direction parallel to the electric field, as governed by the Lorentz force law. Such a material, whose response is dominated by free charges, is referred to as a conductor. In another response, bound charges within an atom or molecule are displaced toward the source charges of opposite polarity. The displacement and separation of opposite charges create an electric dipole, and throughout the medium a net dipole moment is formed that is proportional to the polarizability of that medium. The combined response of the applied electric field and the resulting polarization in the medium is represented by its permittivity $\epsilon = \epsilon_r \epsilon_0$, where ϵ_0

is the permittivity of free space and ϵ_r is the relative permittivity, a dimensionless quantity. A material that is generally dominated by dipole formation and has minimal flow of free charges is referred to as a dielectric.

When the electric field applied to a dielectric alternates polarity with time, perhaps oscillating at a particular frequency, the dipole attempts to reorient itself parallel to the field with each cycle. In doing so, the motion of the bound charges is viewed on a macroscopic scale as a displacement current. In a perfect dielectric, the displacement current leads the electric field over time by a phase of 90°; however, real dielectrics are imperfect, as the dipoles may not completely reorient in the time it takes the field to complete a half-cycle. Thus, the phase between the displacement current and electric field is reduced and energy is lost as heat since there is a net positive power, $P = VI$, when integrated over one cycle. The coexistence of out-of-phase and in-phase components of permittivity are described materially and mathematically as a complex permittivity $\epsilon^* = \epsilon' - j\epsilon''$, where ϵ' is the real part of the permittivity, representing energy storage; ϵ'' is the imaginary part of permittivity, representing energy loss; and j is the imaginary unit. Maximum power transfer (that is, energy loss as heat, in this system) occurs at the frequency for which ϵ'' is maximum, known as the relaxation frequency.

Polymer macromolecules consist of long chains of repeating monomers, the composition and structure of which determine the dielectric properties. One significant structural contribution to the dielectric behavior of a polymer is whether the molecules are polar or nonpolar. Polar molecules have a net dipole moment as a result of bound charge asymmetry; therefore, the permittivity of the material as a whole is frequency-dependent since the reorientation of the molecule or polar subgroup is not instantaneous [17]. Another structural influence on the dielectric properties of a polymer is the density of cross-links, which are covalent or ionic bonds that link polymer chains to one another and have the macroscopic effect of making the polymer more rigid. This reduction in the ability of the molecules to reorient themselves along the electric field (to polarize) reduces the permittivity [18].

Polymer resins such as BMI and other imides undergo an irreversible cure known as thermosetting via the cross-linking process, which allows the resin to be molded into a permanent solid form. Reheating to temperatures above the cure temperature does not melt the solidified resin, but instead degrades the polymer by changing the microstructure, phase morphology and chemical composition [19]. Thermal aging in air induces oxygen diffusion into the polymer that also affects the cross-linking between chains. This change in chemical composition and microstructure often also changes the polymer permittivity [6].

The real and imaginary components of complex permittivity directly relate to measurable electrical parameters, capacitance and resistance, which can be readily measured by a device such as an inductance-capacitance-resistance (LCR) meter. If a polymer sample is placed between two electrodes that are connected to an LCR meter, the meter applies an alternating voltage and measures the magnitude and phase difference of the resulting current. The ratio of these two phasor values is a complex value known as impedance, $Z = R - jX_C$, where R is the resistive component and X_C is the capacitive reactance component. Generally, an LCR meter is set up to calculate and display the capacitance, $C = 1/(\omega X_C)$, and the dissipation factor, $D = R/X_C$. In the case of identical parallel plate electrodes:

$$\epsilon^* = (1 - jD)\frac{Cd}{A} \tag{4.1}$$

where d is the thickness of the sample and separation of the electrode plates and A is the area of a single electrode plate. For samples where double-sided inspection is not possible, the fringing electric field of a coplanar capacitor penetrates the sample, thus influencing the measured value of capacitance that depends upon the sample permittivity.

4.3 Experimental technique

The bulk of the experimental work was divided into two phases: BMI composite sample fabrication and thermal aging, and capacitive sensing of the samples using parallel plate and interdigital coplanar electrodes. The following sections describe the experimental work in detail.

4.3.1 Sample fabrication and preparation

BMI pre-impregnated with glass fiber (prepreg) was purchased. The glass fiber was a style 7781 E-type with a 497A finish coating. Style 7781 is an eight-harness satin type popular in

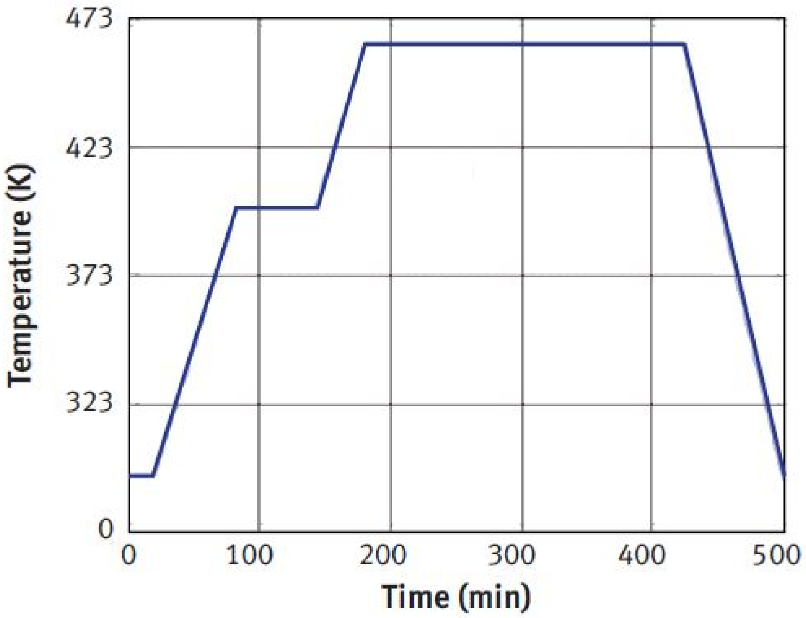

Figure 4.3 Thermal cure cycle for the bismaleimide glass-fiber polymer-matrix composite samples. During the cure, a constant pressure of 586 kPa was applied to the 305 × 305 mm^2 sample.

the aerospace industry, having a fiber count of 57 × 54 ends per 2.54 cm and a mass density of 303 g/m^2. E-type glass is an electrical type glass with 204 filaments of 7.4 µm diameter each, per fiber, and relative permittivity between 6.3 and 6.6 at 1 MHz [20]. Coating finish 497A is a silane finish that is designed to undergo addition or condensation reactions with polymeric resins such as epoxy, phenolic, polyimide, and polyester for better binding to the matrix. The prepreg was stacked in eight 305 × 305 mm^2 plies, vacuum-bagged and inserted into a hot press for the pressure and thermal cure recipe, shown in Figure 4.3. Breather and bleeder cloths, typically used in composite fabrication, were not included in this study for the purpose of creating finished samples with a smoother surface, to reduce uncertainties in capacitive testing. Finally, the samples underwent a 6 h post-cure at 519 K (246 °C) under atmospheric pressure as prescribed by the manufacturer. The purpose of this post-cure was to maximize the strength retention of the PMC at elevated temperatures [15].

A number of 38 × 38 mm^2 samples were cut from the central area of the cured 305 × 305 mm^2 laminate, avoiding edge variations. All samples were dried at 393 K (120 °C) for 4 h and stored in a desiccator prior to both thermal aging and dielectric measurements. One group of three samples acted as a control, undergoing only the drying procedure. Other groups of three samples were isothermally aged at 548, 598 and 648 K (275, 325 and 375 °C). Each of these was aged for 4 h and allowed to cool in the furnace overnight. Sample mass and thickness, measured as an average of five points using a digital micrometer, were recorded before and after thermal aging.

4.3.2 Parallel plate electrode dielectrometry

A dielectric test fixture in conjunction with an LCR meter was used for parallel plate dielectrometry in this work. The test fixture incorporated a fixed unguarded electrode and a movable guard electrode, their separation being controlled by a micrometer, Figure 4.4. The guard electrodes, provided with the test fixture, came in four sizes of two types: one 5 mm and one 38 mm diameter rigid metal electrode, and one 56 mm and one 20 mm diameter electrode with a center spring-loaded ball bearing for contacting a secondary electrode in direct contact with the sample. To reduce possible edge effects in the measurements, a secondary electrode with 31.75 mm diameter (a 3.175 mm thickness, C26000 brass alloy disc) was used in conjunction with the 56 mm diameter guard electrode with ball bearing guarded electrode, as shown in Figure 4.4. The guard electrode was held at the same electric potential as the guarded secondary electrode, thus virtually eliminating fringing capacitance between the secondary and unguarded electrodes, ensuring that the field in the material under test was essentially uniform and parallel as assumed by (4.1). Further, the samples were made as smooth and flat as possible, by the technique described in the previous section, in order to ensure that the gap between the parallel plate electrodes was filled by the sample as assumed by (4.1) and contained no significant pockets of air.

Upon test fixture calibration (performed each time after power-up of the LCR meter), the samples were placed between the unguarded electrode and the brass disc, and the guarded ball bearing was brought into contact with the disc and tightened to minimize any air gap between the sample and the disc electrodes. The capacitance and dissipation factor were measured at 44 frequencies between 100 Hz and 2 MHz. Using the sample thickness and diameter of

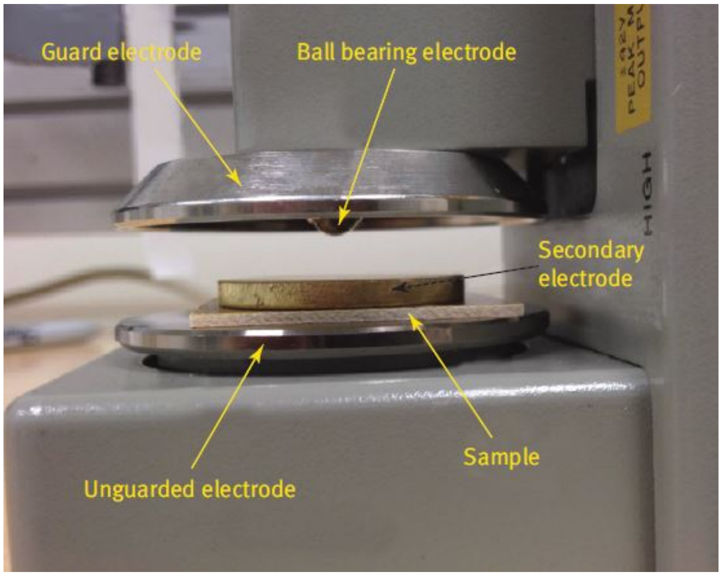

Figure 4.4 Dielectric test fixture. The sample is sandwiched between the secondary electrode and the unguarded electrode. The ball bearing electrode makes electrical contact with the secondary electrode when pressed together and the guard electrode reduces fringing effects.

the secondary electrode, the permittivity of each sample was calculated from the capacitance measurements using (4.1).

4.3.3 Interdigital electrode dielectrometry

The 24.4 mm diameter sensor employed here and shown schematically in Figure 4.2 consisted of 30 concentric copper annuli interdigitated with 31 annuli of the opposite polarity. Each annulus was 100 µm wide with 100 µm separation from its neighbor. Two parallel signal buses, routed radially through the digits, connected all like-polarity digits. The signal buses terminated at two 1 mm^2 pads for making electrical contact with the LCR meter. All conductive traces were composed of 18 µm thick bare copper deposited on a 310 µm thick glass-fiber hydrocarbon/ceramic substrate. The relative permittivity of the substrate was measured independently using a dielectric spectrometer at 1 MHz to be 3.34 ± 0.05 [7].

To achieve repeatable measurements, the sample and sensor were pressed together by means of a plastic spring-loaded clamp with rotatable jaws. A lab bench surface provided rigid support, as shown in Figure 4.5. After calibration of the LCR meter probe, the probe tip was pressed

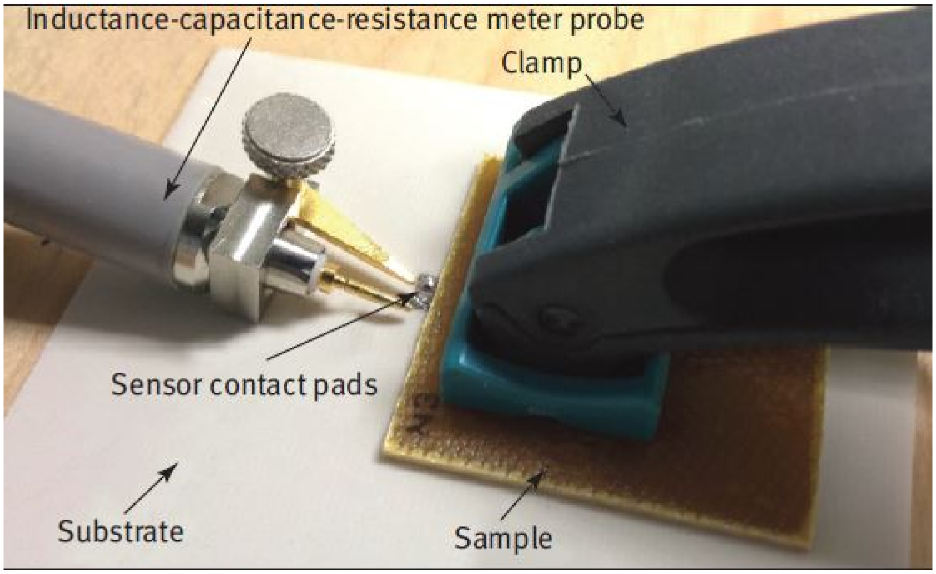

Figure 4.5 Concentric interdigital dielectrometry setup. The sensor is sandwiched between the substrate and the bismaleimide glass-fiber polymer-matrix composite sample. A clamp minimizes possible air gaps and enhances repeatability.

into contact with the sensor contact pads, which were the only parts of the sensor exposed to the open air after the sample had been pressed to the sensing digits, as shown in Figure 4.5. A manual trigger on the LCR meter initiated a preset frequency sweep, and the sensor capacitance and dissipation factor were recorded at each frequency point.

4.3.4 Measurement uncertainties

Measurement accuracy is generally contingent on factors particular to the measurement device, such as frequency, and upon external factors, such as sample dimensions. In this system, high frequency measurements beyond 10 MHz suffered from dominating inductive reactance in the probe cables, while the uncertainty of measurements, in particular for the LCR meter used in this work, increased with decreasing frequency for a given measured capacitance. In general, samples with a high area-to-thickness ratio were desirable, both reducing fringing field uncertainty if unguarded electrodes were used and increasing $|Z|$. As mentioned previously, air gaps between the electrodes and sample were reduced or eliminated by means of applied pressure. In the case of PMCs, however, surface roughness existed in the form of a permanent and regular pattern of air voids on the sample surface. The uncertainty in inferred was low

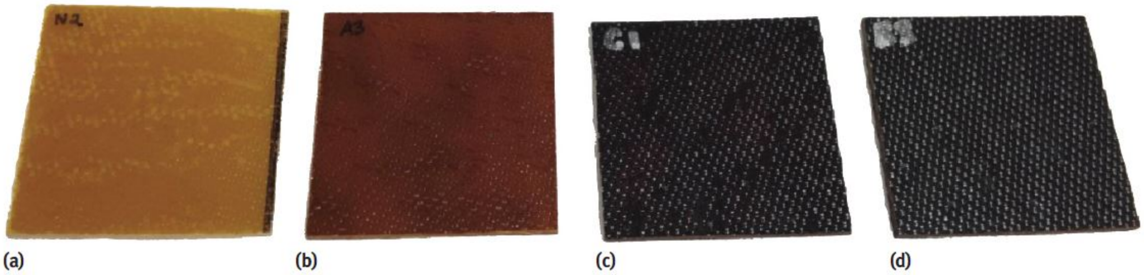

Figure 4.6 Bismaleimide glass-fiber polymer-matrix composite samples used in parallel plate and interdigital capacitive sensing experiments. Each sample is 38 × 38 mm^2. The sample set contains: (a) a pristine sample and samples aged at: (b) 548 K (275 °C); (c) 648 K (325 °C); and (d) 698 K (375 °C).

Table 4.1 Mean percentage mass loss for isothermally-aged bismaleimide glass-fiber polymer–matrix composite samples. Uncertainties listed are one standard deviation from mass measurements on three different samples. The mean mass of the samples prior to aging was 4.12 ± 0.03 g.

Aging temperature	**Mass loss (%)**
548 K (275 °C)	0.203 ± 0.004
598 K (325 °C)	0.54 ± 0.03
648 K (375 °C)	3.3 ± 0.6

because of this effect in the case of parallel plate electrodes, since the volume occupied by the air voids was on the order of 0.5 % of the sample volume but was more significant in the case of measurements using coplanar interdigital electrodes for which the spacing between the electrodes was on the same order as the surface roughness. For this reason, C was reported for the interdigital measurements rather than ϵ'_r (real relative permittivity), where $\epsilon'_r = \epsilon'/\epsilon_0$ and ϵ_0 is the permittivity of free space.

4.4 Results

Several changes to the BMI glass-fiber PMC samples were observed due to isothermal aging, the appearance of which is shown in Figure 4.6. Table 4.1 shows a clear trend in the increase of sample mass loss with aging temperature, up to 3.3% mass loss for samples aged at 648 K (375 °C), which is due to oxidation of the BMI polymer.

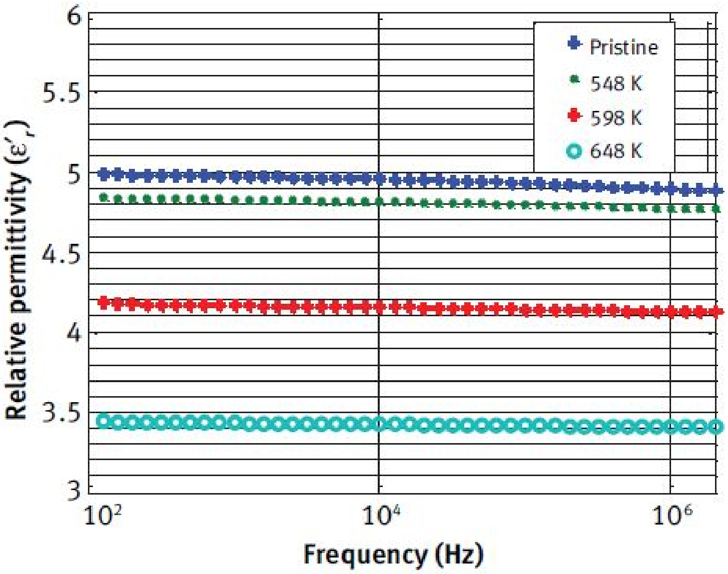

Figure 4.7 Relative permittivity of isothermally-aged bismaleimide glass-fiber polymer-matrix composite samples measured using parallel plate electrodes. Each data point is the mean of three measurements on different samples. Estimated uncertainties are listed in Table 4.2.

4.4.1 Parallel plate electrode dielectrometry

A reduction in real permittivity with increasing aging temperature was observed, when ϵ_r' was measured using parallel plate electrodes, shown in Figure 4.7, with a mean reduction of 31 % for samples aged at 648 K (375 °C). The dissipation factor shown in Figure 4.8 increased at low frequencies, below 1 kHz, indicating the likely presence of impurities in the BMI. It also increased toward a possible maximum just beyond 1 MHz, which is indicative of a dielectric relaxation characteristic to the BMI polymeric chain. Generally speaking, Figure 4.8 shows a clear reduction in dissipation factor with increasing aging temperature over the frequency range measured, suggesting a relaxation shift to higher frequency with increasing aging temperature. Uncertainties in the measured data are tabulated in Table 4.2.

4.4.2 Interdigital electrode dielectrometry

Capacitance measured using coplanar interdigital electrodes shows a similar trend, Figure 4.9 to measured ϵ_r', Figure 4.7, with an average reduction of 17 % comparing measurements on

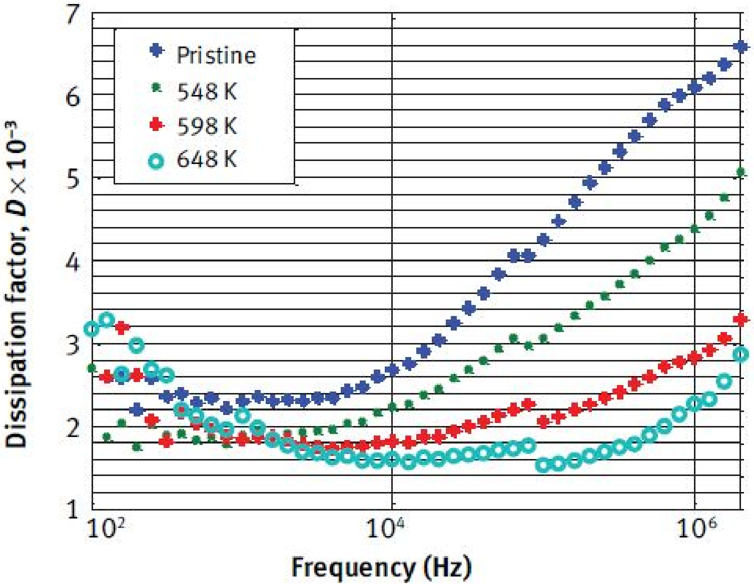

Figure 4.8 Dissipation factor of the isothermally-aged bismaleimide glass-fiber polymer-matrix composite samples measured using parallel plate electrodes. Each data point is the mean of three measurements on different samples. Estimated uncertainties are listed in Table 4.2. Note that the discontinuity in all measurements near 100 kHz is due to internal switching of LCR meter circuits.

pristine samples with those on samples aged at 648 K (375 °C). Measured C for the isolated sensor (in air) is included in this figure to show the minimum possible capacitance for this particular sensor. Permittivity extraction from measured capacitance of the interdigital sensor is not trivial and is very dependent upon surface roughness of the sample, and so was not attempted in this work. Because of the linear relation between capacitance and permittivity, however, the relative differences between the variable plots and between Figures 4.7 and 4.9 are comparable. The dissipation factor measured using the interdigital electrodes, Figure 4.10 appears to present a direct current or low-frequency conductivity contribution that resulted in a linear response in the lower frequencies when plotted on a log-log scale. In dielectric spectroscopy, such a contribution is typically regarded as a conductivity term $\sigma/\omega\epsilon_0$, where σ is the conductivity, which is appended to the function describing the imaginary permittivity and, when plotted, results in a linear slope [21][22]. Applying a linear regression for the lower frequencies, this term was subtracted from the dissipation factor 4.11 to reveal the presence of any dielectric relaxations. Comparing the data of Figure 4.11 with those of Figure 4.8, a

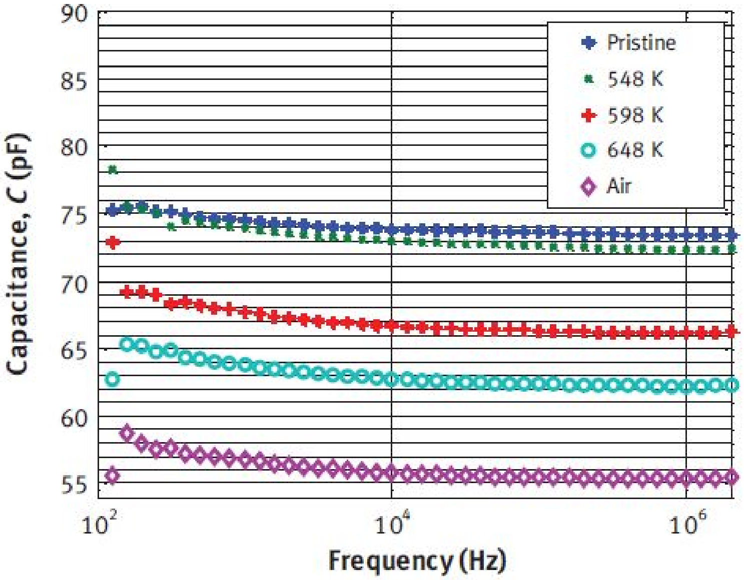

Figure 4.9 Measured capacitance of the concentric interdigital electrode sensor when placed on the surface of isothermally-aged bismaleimide glassfiber polymer-matrix composite samples. Each data point is the mean of three measurements on different samples. Estimated uncertainties are listed in Table 4.2.

similar trend is observed, that the magnitude of the peak in D reduces as aging temperature increases. The significant scatter in data presented below 1 kHz in Figure 4.11 is likely due to low impedance causing loss of accuracy in the LCR meter measurements in this frequency range. This is a typical problem for impedance measurement devices and the frequency threshold below which loss of accuracy is observed also depends on sample properties and electrode geometry.

4.4.3 Measured uncertainties

Uncertainties associated with the data presented in in Figures 4.9, 4.10, and 4.11 are given in Table 4.2 at 1 kHz and 1 MHz for the parallel plate and interdigital electrode sensors. Generally speaking, an increase in uncertainty is observed as thermal aging temperature increases, indicating more variability in the samples as the severity of aging increases. With increasing frequency, on the other hand, uncertainties in ϵ_r' and C are very similar for both parallel plate and interdigital sensors. Measurement uncertainties in D, however, show no identifiable trend as a function of frequency.

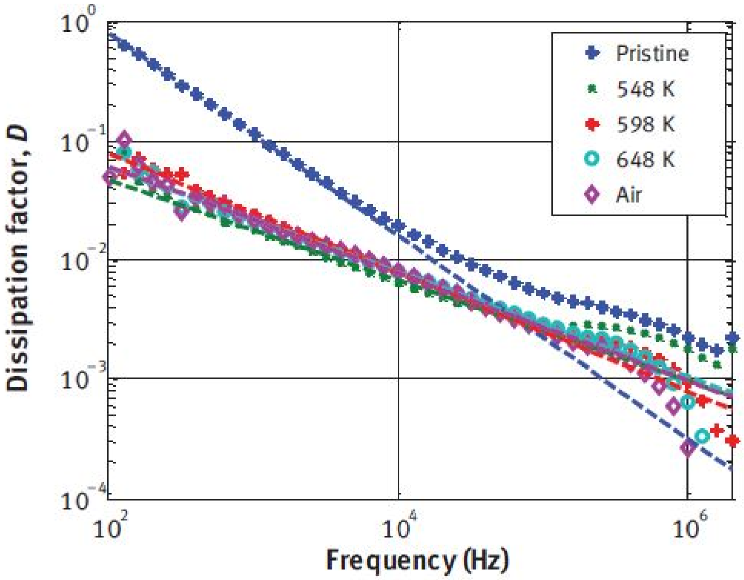

Figure 4.10 Measured dissipation factor of the concentric interdigital sensor when placed on the surface of the isothermally-aged bismaleimide glass-fiber polymer-matrix composite samples. Each data point is the mean of three measurements on different samples. The linear asymptotes represent a direct current conductivity effect, which is subtracted to yield Figure 4.11. Estimated uncertainties are listed in Table 4.2.

4.5 Discussion

The results presented in this work demonstrate the ability of a single-sided concentric interdigital electrode sensor to detect changes in the complex permittivity of BMI glass-fiber PMC as a result of isothermal aging, shown in Figures 4.9 and 4.11. The single-sided sensor could potentially be used in a handheld probe, such as that presented in prior work, or for structural health monitoring as a component of an in-situ sensor array [11]. The capacitance and dissipation factor measured using the interdigital sensor are consistent with the permittivity and dissipation factor measured using an extant parallel plate electrode technique on the same samples. Uncertainties in the measured capacitance of the interdigital sensor grew rapidly with increasing aging temperature, indicating possible growing sample variability as a function of age. The difference in shape of the dissipation factor response between Figure 4.8 and Figures 4.10 or 4.11 is most likely due to the different paths that the electric flux took for each sensor. Whereas the flux permeated the bulk of the sample in a parallel plate arrangement, the

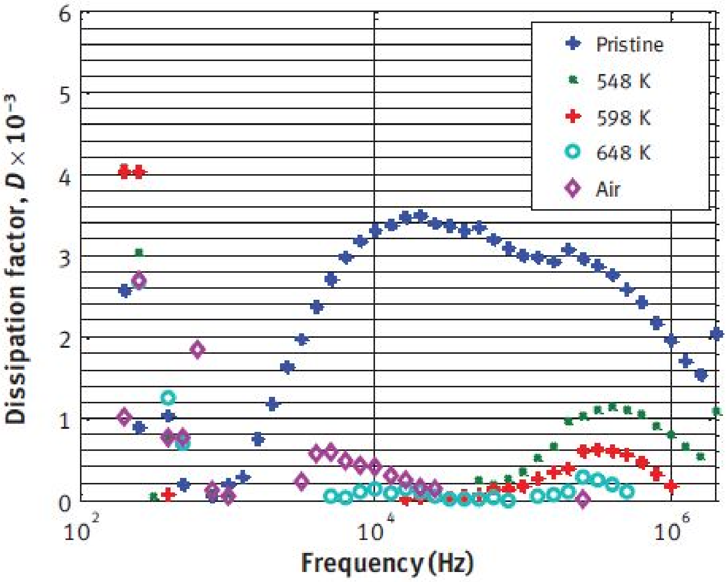

Figure 4.11 Measured dissipation factor, from Figure 4.10, with direct current conductivity contribution subtracted.

interdigital electrode flux was confined nearer to the sample surface, which was prone to collect various impurities. These impurities may have had a different microstructure and, therefore, a different dielectric response with frequency.

4.6 Conclusion

With a clear relationship between BMI glass-fiber PMC thermal aging and complex dielectric permittivity established in this work, the next major step is to compare these results with those of mechanical tests on similar samples, seeking a correlation between dielectric measurements and interlaminar shear strength (ILSS). The establishment of such a link is necessary to move towards capacitive NDT for inference of ILSS of critical structural composites in the field. Microstructure analysis may provide useful information toward improving the understanding of the surface roughness effect on the interdigital measurements of capacitance and insight into the origins of the low-frequency conductivity contributions observed in Figure 4.10. Further, the effect of aging regimes that more closely mimic the exposure of in-service material will be studied in future work.

Table 4.2 Uncertainties of measurements performed using parallel plate and interdigital electrodes on thermally-aged bismaleimide glass-fiber polymer-matrix composite samples. Each uncertainty is one standard deviation of the mean values plotted in Figures 4.9, 4.10, and 4.11, expressed as a percentage (%). Each mean value was the mean value of measurements on three different samples.

	1 kHz			
	Parallel plate		**Interdigital**	
Temperature	ϵ_r'	D	C	D
Pristine	2	7	0.3	10
548 K (275 °C)	2	2	2	40
598 K (325 °C)	4	5	4	30
648 K (375 °C)	5	5	4	40
	1 MHz			
Pristine	2	2	0.3	70
548 K (275 °C)	2	4	1	20
598 K (325 °C)	4	7	4	30
648 K (375 °C)	5	20	4	30

4.7 Acknowledgments

This work was supported by an American Society for Nondestructive Testing Fellowship Award and by the Iowa Space Grant Consortium. The authors thank Dr. Connor Daily for preparing the samples and individuals of The Boeing Company for useful conversations.

4.8 References

[1] D. M. Forney and D. E. Chimenti, "Nondestructive Evaluation Coming of Age", *Encyclopedia Britannica: 1986 Yearbook of Science and the Future*, pp. 87-90, 1986.

[2] S. K. Burke and L. R. F. Rose, "Eddy-current NDI of cracks in thin plates", *J. Phys. D: Appl. Phys.*, Vol. 20, pp. 797-800, 1987.

[3] D. K. Hsu, "Nondestructive testing using air-borne ultrasound", *Ultrasonics*, Vol. 44, pp. e1019-e1024, 2006.

[4] D. K. Hsu and D. J. Barnard, "Inspecting Composites with Airborne Ultrasound: Through Thick and Thin", *Review of Progress in QNDE*, AIP Conf. Proc., Vol. 820, pp. 991-998, 2006.

[5] A. Makeev and Y. Nikishkov, "Fatigue Life Assessment for Composite Structure", *Proc. 26th ICAF Symposium*, Montreal, Quebec, Canada, 1-3 Jun. 2011.

[6] S. Diaham, M. L. Locattelli and T. Lebey, "Improvement of polyimide electrical properties during short-term of thermal aging", *Conference on Electrical Insulation and Dielectric Phenomena*, pp. 79-82, 2008.

[7] T. Chen, "Capacitive sensors for measuring complex permittivity of planar and cylindrical structures", *Graduate Theses and Dissertations*, Paper 12294, Iowa State University, 2012.

[8] S. Laflamme, M. Kollosche, J. J. Connor and G. Kofod, "Soft capacitive sensor for structural health monitoring of large-scale systems", *Struct. Control Health Monit.*, Vol. 19, pp. 70-81, 2012.

[9] B. A. Auld, J. Kenney and T. Lookabaugh, "Electromagnetic sensor arrays—theoretical studies", *Review of Progress in QNDE*, edited by D. O. Thompson and D. E. Chimenti, Vol. 5A, pp. 681-690, 1986.

[10] X. B. Li, S. D. Larson, A. S. Zyuzin and A. V. Mamishev, "Design Principles for Multichannel Fringing Electric Field Sensors", *IEEE Sensors J.*, Vol. 6, No. 2, pp. 434-440, 2006.

[11] T. Chen and N. Bowler, "Analysis of a Concentric Coplanar Capacitive Sensor for Nondestructive Evaluation of Multi-layered Dielectric Structures", *IEEE Trans. Diel. Electr. Insul.*, Vol. 17, No. 4, pp. 1307-1318, Aug. 2010.

[12] A. V. Mamishev, K. Sundara-Rajan, F. Yang, Y. Du, and M. Zahn, "Interdigitated Sensors and Transducers", *Proc. IEEE*, Vol. 92, No. 5, pp. 808-845, 2004.

[13] G. Liang, Z. Zhang, J. Yang and X. Wang, "BMI Based Composites With Low Dielectric Loss", *Polymer Bulletin*, Vol. 59, pp. 269-278, 2007.

[14] C. L. Holloway, M. S. Sarto and M. Johansson, "Analyzing Carbon-Fiber Composite Materials With Equivalent-Layer Models", *IEEE Trans. Electromagn. Compat.*, Vol. 47, No. 4, pp. 833-844, 2005.

[15] H. Stenzenberger, "Bismaleimide Resins", *ASM Handbook*, Vol. 21, Composites, ASM International Inc., pp. 97-100, 2001.

[16] L. Li, N. Bowler, P. R. Hondred, and M. R. Kessler, "Dielectric Response of Polyimide to Thermal and Saline Degradation", *2010 Annual Report Conference on Electrical Insulation and Dielectric Phenomena*, West Lafayette, Indiana, USA, 17-20 Oct. 2010.

[17] Z. Ahmad, "Polymeric Dielectric Materials", *Dielectric Material*, edited by M. A. Silaghi, InTech, 2012.

[18] X. Chen, J. Ye, L. Yuan, G. Liang and A. Gu, "Multi-functional ladderlike polysiloxane: synthesis, characterization, and its high performance flame retarding bismaleimide resins with simultaneously improved thermal resistance, dimensional stability and dielectric properties", *J. Mater. Chem. A*, Vol. 2, pp. 7491-7501, 2014.

[19] L. Li, "Dielectric properties of aged polymers and nanocomposites", *Graduate Theses and Dissertations*, Paper 12128, Iowa State University, 2011.

[20] *JPS Composite Materials Data Book*, JPS Industries Inc., Anderson, South Carolina, USA.

[21] J. Liu, Z. Zhang, D. E. Bowen, E. A. Eastwood and N. Bowler, "Plasticization and reinforcement in a boron cage compound polyurethane nanocomposite: A dielectric study", *J. Non-Cryst. Solids*, 371-372, pp. 6-13, 2013.

[22] J. D. Menczel and R. B. Prime, eds., *Thermal Analysis of Polymers, Fundamentals and Applications*, John Wiley & Sons, Hoboken, New Jersey, USA, 2009.

CHAPTER 5. AN INTERDIGITAL CAPACITIVE CLAMP SENSOR FOR NONDESTRUCTIVE EVALUATION OF WIRE INSULATION

Featuring excerpts from papers published in
IEEE Sensors Journal
Robert T. Sheldon and Nicola Bowler,
The 2014 Annual Report Conference on Electrical Insulation and Dielectric Phenomena
Emily M. Arvia, Robert T. Sheldon and Nicola Bowler,
&
The 9th International Topical Meeting on Nuclear Plant Instrumentation, Control & Human-Machine Interface Technologies
Nicola Bowler, Robert T. Sheldon and Emily M. Arvia

5.1 Introduction

During normal service, all insulated wires are exposed to number of degradation mechanisms, such as moisture absorption, extreme temperatures, and mechanical stress. In critical systems such as aircraft and nuclear reactors, failure of the wire insulation can be potentially hazardous as these wires often transmit power, navigation and control signals. Although many wire testing devices and other NDE techniques are commercially available, few are designed to directly and easily characterize the insulation itself.

One type of commercially-available wire test equipment is a time-domain reflectometer, which is designed to transmit signals along a wire and measure the time-of-flight of any reflected pulses, which can be used to locate breaks into conductor continuity [1]. This technique, however, does not work well at locating insulation breaks, much less characterize the permittivity of the insulation. In [1], a technique called *partial discharge* is developed whereby a high voltage pulse is transmitted down and insulated wire and degraded insulation regions cause the signal to partially discharge its energy into the degraded region, which is detectable as a reflected pulse. This technique requires high voltages and partial discharge currents that may damage the wire sample. Another commercially-available insulation tester is a resistance tester, which applies a high voltage between the conductor and an exterior point, and the resulting current magnitude is proportional to the conductivity of the insulation [2]. Again, high voltages run the risk of damaging the wire, whereas a measurement of the wire insulation permittivity can be made at lower voltage and, as shall be shown here, can be used to infer the integrity of the insulation.

As mentioned in Chapter 1, capacitive sensors are ideal for characterizing low-conductivity media due to the linear relationship between the measurable quantity of capacitance and the material property of permittivity. For an insulated wire, the useful geometry of the dual curved patch electrode sensor presented in [3] was improved upon in [4], by increasing the magnitude of the measured capacitance thus improving signal-to-noise ratio, with the introduction of a cylindrical interdigital electrode structure, a schematic diagram of which is shown in Figure 5.2. In this chapter is presented a practical clamp sensor design, Figure 5.1 to apply the interdigital electrodes to the surface of wires for inspection. Two different sets of wires were aged in different controlled environments and the relative change in measured capacitance between aging conditions was analyzed. Sections 5.2 and 5.3 discuss the clamp design and measured results on chemically-aged aircraft wire. In Section 5.4, measurements taken using the same clamp sensor on nuclear power plant wires irradiated with controlled doses of ionizing radiation are described.

5.2 Clamp sensor design

A practical sensor applicator design, in the form of a plastic spring-loaded clamp, Fig. 5.1, was developed in order to apply and remove the electrodes, the modeled design shown in Figure 5.2, now attached to two jaw faces, to the surface of a wire-under-test. Each jaw surface possesses a groove covered with a layer of foam that allows the jaws to cradle the wire and

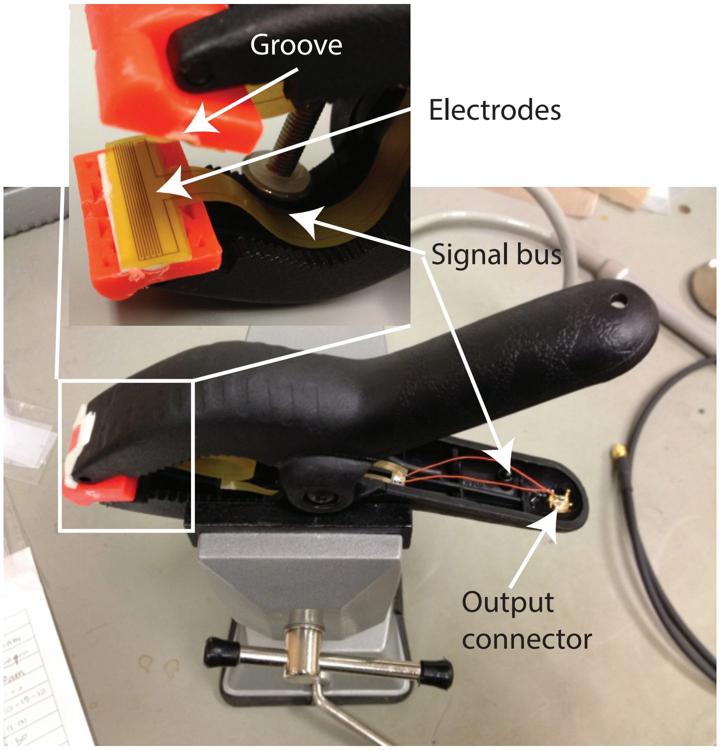

Figure 5.1 Plastic spring-loaded clamp sensor with inset showing detail of the jaws and interdigital electrodes attached to both orange jaws.

press the electrodes onto the wire surface. The signal bus strip passes back along the clamp handle to an SMA output connector for easy connection to the LCR meter.

The electrode configuration is shown in Figure 5.3. The two patches of seven digits are connected by a 100-mm-long bus strip, and were also fabricated by American Standard Circuits, Inc., utilizing 17.8-µm-thick bare copper cladding deposited on a 25.4 µm thick Kapton® polyimide film substrate. This substrate was then adhered to the foam in the grooves of each jaw of the spring-loaded clamp.

This clamp design caters for modest variation in wire sample diameter via its dual-sided application of interdigital electrodes mounted on compressible foam. In this way, measurements can be performed using the same sensor on wires of different gauge but it is difficult to measure parameters such as g accurately. For this reason, it is impractical to attempt to extract permittivity of the wire insulation with the present probe design, although this has been done for simpler electrode configurations [7][8][3]. In the experiment that follows, a pristine refer-

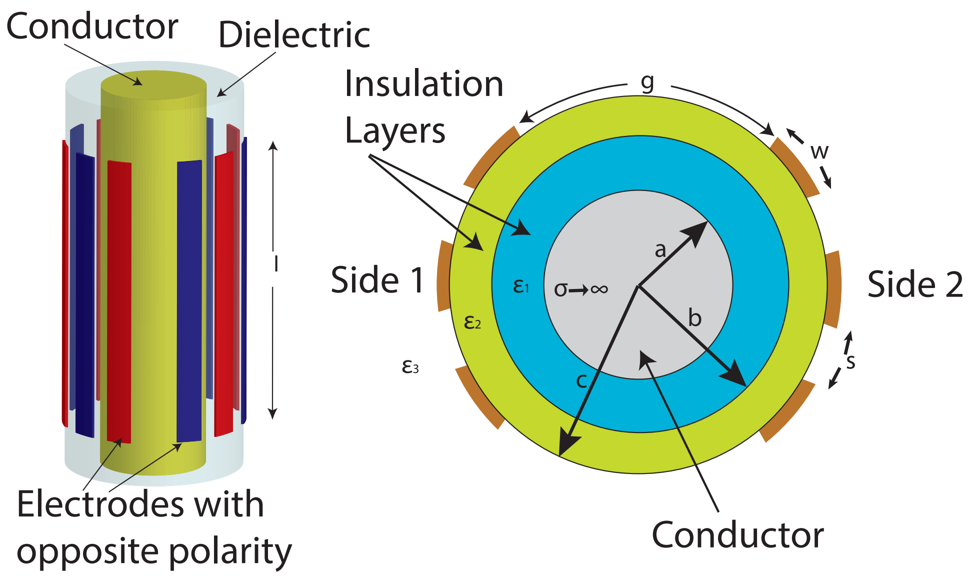

Figure 5.2 Cylindrical interdigital capacitive sensor. The radii of the central conductor, cylinder insulation, and sensor substrate are denoted a, b and c, respectively. The electrodes have width w, spacing s, gap g between the two interdigital electrode sides and length l [4].

Table 5.1 Composition and dimensions of the layers comprising a 20 AWG M5086 wire.

Layer	**Size (mm)**
Tin-coated stranded copper conductor diameter	1.0 ±0.1
PVC thickness (inner layer)	0.22 ±0.03
Glass fiber thickness (middle layer)	0.22 ±0.03
Nylon 6 thickness (outer layer)	0.15 ±0.03
Total diameter	**2.2 ± 0.1**

ence wire is used for comparison of capacitance values that directly relate to the permittivity changes that resulted from degradation.

5.3 Measurements on chemically-aged wire

A controlled aging experiment was conducted on M5086/2 wire (Allied Wire & Cable, Inc.) in order to assess the effectiveness of the interdigital capacitive clamp sensor. The composition and dimensions of 20 AWG M5086/2 wire are given in Table 5.1.

Six segments of M5086/2 wire, each approximately 10 cm long, were immersed in different fluids that are commonly found onboard an aircraft, with a seventh pristine segment acting

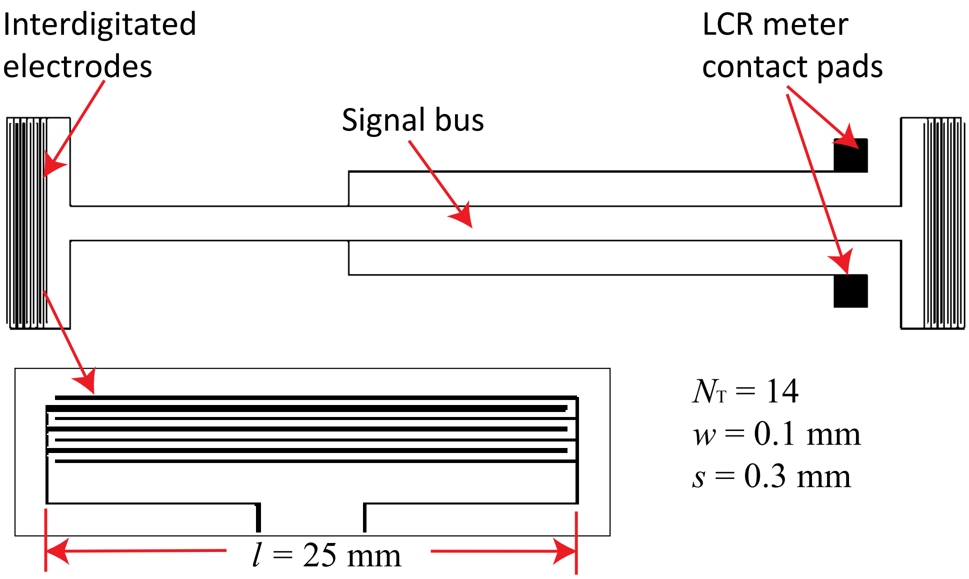

Figure 5.3 Planar schematic of the interdigital capacitive sensor used in the plastic spring clamp. The bus strip is 100 mm long.

as the control wire. The ends of the segments were sealed with paraffin wax to protect the conductor and the samples were then completely immersed in separate closed glass containers filled with aircraft cleaner, deicer 50/50, distilled water, hydraulic fluid, 70 % isopropanol and Jet A fuel for 10 days. Then, each immersed wire segment was removed from the fluid, thoroughly dried using Kimwipes, and immediately stored in plastic storage bags. The time from immersion removal to capacitive measurement for each sample was less than one hour.

The capacitance of the sensor was measured at 20 points along the axis of each of the wire segments and the mean value calculated. Since capacitance is proportional to permittivity, and because the insulation layers of the wire (especially the outer layer of Nylon 6) may absorb or react with these chemicals to cause changes to the permittivity, one would expect to observe a consequent change in the capacitance when compared with a pristine, or non-immersed, wire. Data from the immersed and pristine samples are shown in Fig. 5.4(a) and are compared with data taken independently on chemically exposed thin sheets of Nylon 6 (between 0.5 and 0.6 mm in thickness), which forms the outer layer of M5086/2 wire, using parallel plate electrodes [9].

It is immediately clear from the data shown in Fig. 5.4 that hydraulic fluid and Jet A fuel (non-polar fluids) had very little impact on the capacitance measured on M5086 wires while the other (polar) fluids gave rise to a significant change in measured capacitance, most likely due to significantly changed dielectric properties of the wire insulation. Hydraulic fluid and jet fuel effected only a 1.8 % and 2.1 % increase in capacitance, respectively, from that of the pristine wire. On the other hand, the wire immersed in 70 % isopropanol exhibited the largest change in capacitance; an 18.6 % increase. Wires immersed in cleaner, deicer and distilled water showed more moderate increases of 7.8 %, 6.1 % and 4.5 %, but these are still significant changes compared with the pristine wire capacitance. For comparison, experiments were performed on sheets of pure Nylon 6, which constitutes the outer insulation layer on M5086/2 wire, Table 5.1. Capacitance measured on chemically-aged Nylon 6 after an 8-day submersion using parallel plate electrodes is shown in Fig. 5.4(b). These results correlate well with the basic pattern of experimental results obtained from pure Nylon 6 samples, indicating the feasibility of using the clamp sensor presented here for evaluation of wire insulation degradation. The measurements performed on samples immersed in cleaning fluid showed the largest standard deviation in the experiments, partially explaining the largest discrepancy seen, for this case, between the interdigital and parallel plate measurements of capacitance, and also indicating that the chemical absorption was highly dependent on position along both test pieces in the case of immersion in cleaner.

5.4 Measurements on irradiated wires

The integrity of nuclear power plant cables has been identified as a major concern that may limit the goal of extending the life of light-water reactor power plants [10]. Over extended periods of service, the polymeric insulation and jacket materials of a typical low- or medium-voltage power cable, or of a control cable, degrade due to exposure to heat, ionizing radiation and moisture, etc. It is desirable to monitor these changes nondestructively and to predict the remaining-useful-life of the cable if possible. In an oxygenated environment, exposure to heat and ionizing radiation tends to cause oxidative aging in polymer systems. Depending on the polymer, oxidation usually leads to changes in dielectric constant and loss (real and imaginary parts of permittivity) of the material which, in principle, can be monitored by capacitive sensing [11][12][13].

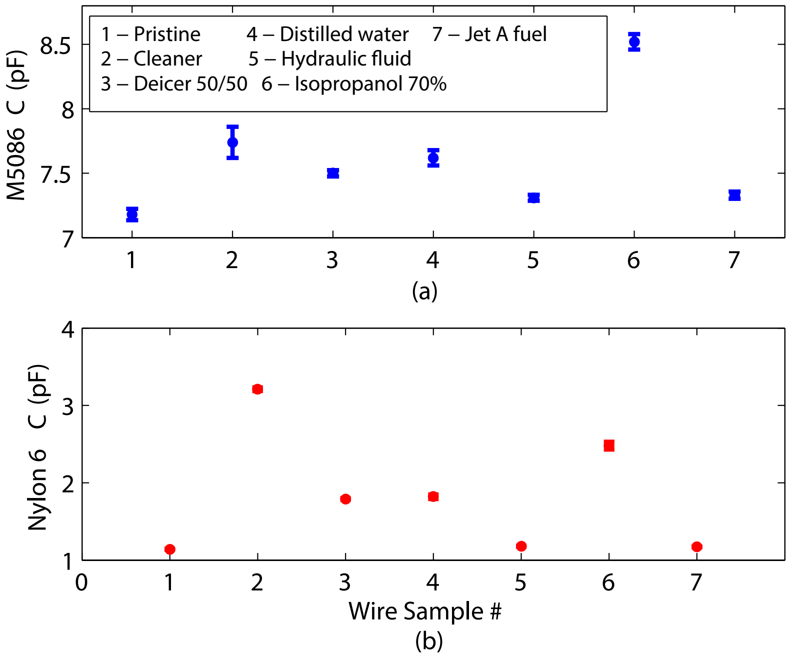

Figure 5.4 Comparison of the interdigital and parallel plate electrode capacitance measurements when applied to (a) M5086 aircraft wire and (b) pure Nylon 6 sheet samples after a 10-day and 8-day submersion in the given fluids, respectively. The error bars for M5086 wire are ± 1 standard deviation of 20 measurements while those for the Nylon 6 represent ± 1 standard deviation of 3 measurements [9]. Both experiments utilized the same Agilent E4980A Precision LCR Meter at 1 MHz.

In this work, the clamp sensor design in Section 5.2 is used to measure the capacitance (C) and dissipation factor (D) changes of the sensor due to controlled amounts of ionizing radiation to which two types of insulating materials commonly found in nuclear power plants: flame-retardant ethylene-propylene rubber (FR-EPR) and silicone rubber (SIR). Measured results are compared with the industry standard test of elongation-at-break (EAB), which is destructive, and indenter modulus (IM), which is a relatively new mechanical non-destructive test.

Elongation-at-break, indenter modulus and capacitance measurements were performed as follows:

- **EAB**—Tubular insulation specimens approximately 150-mm-long were prepared by removing the central conductor. The specifications of the tensile test are provided in [14].

Each specimen was gripped firmly in the chuck of a tensile tester and a tension rate of 500 mm/min was applied until failure of the sample, at which moment the EAB was recorded. Three nominally-identical samples were tested per aging condition and the mean value of EAB reported [15].

- **IM**—An indenter may be used to make nondestructive measurements of mechanical properties of wire insulation material. The Indenter Polymer Aging Monitor (IPAM) used in this study was provided by Analysis and Measurement Services Corporation. A small indentation is made in the insulation material by the rounded pyramidal tip of the device and "indenter modulus" (IM) is recorded. IM has unit Nm^{-1} rather than Nm^{-2} as in the case of elastic modulus. Full detail is provided in [16]. Nine measurements were taken at different points along the length of an 8-cm-long section of insulated wire, with central conductor intact.

- **C/D**—The capacitive sensor used in these tests consisted of a plastic spring-loaded clamp with interdigital electrodes attached to each jaw. The clamp sensor is applied to the sample wire and C and D are influenced by the dielectric properties of the wire insulation. The sensor is connected to an LCR meter by which C and D may be measured, after system calibration, at frequencies specified by the user. In this study, C and D were recorded at 1 kHz and 1 MHz. Each wire was inserted between the orange jaws of the clamp and C and D recorded at 10 different locations along each wire. All samples were tested on the same day in order to minimize uncertainties arising from possible variations in temperature and humidity, etc.

The FR-EPR and SIR insulated samples studied here were both supplied by the same company. The FR-EPR samples were of three colors whereas the SIR samples were all white. All samples were aged by exposure at radiation level 100 Gy/h for various times, and at temperatures 80, 90 or 100 °C (FR-EPR) and 100 or 135 °C (SIR) as indicated in Tables 5.2 and 5.3, respectively. Forty-seven FR-EPR samples and fifty-one SIR samples were studied.

Table 5.2 Exposure duration of FR-EPR coated wire samples at radiation level 100 Gy/h and temperatures 80, 90 or 100 °C.

Wire insulation color and designator number			**Exposure conditions**	
Black	**White**	**Red**	**T (°C)**	**time (h)**
-	-	151	80	2,360
-	-	152	80	2,644
111	131	-	80	2,881
112	132	-	80	3,545
111	131	-	80	2,881
113	133	153	80	3,948
114	134	154	80	4,619
-	-	155	90	1,877
-	-	156	90	2,123
115	135	157	90	2,383
116	136	158	90	2,714
117	137	159	90	3,047
118	138	160	90	3,784
119	139	161	90	4,619
120	140	162	90	5,781
-	-	163	100	1,177
-	-	164	100	1,390
-	-	165	100	1,554
-	-	166	100	1,791
121	141	167	100	1,981
122	142	168	100	2,360
123	143	-	100	2,995
124	144	169	100	5,280

Table 5.3 Exposure duration of SIR coated wire samples at radiation level 100 Gy/h and temperatures 100 or 135 °C.

Wire insulation color and designator number			**Exposure conditions**	
White 1	**White 2**	**White 3**	**T (°C)**	**time (h)**
411	431	451	100	282
412	432	452	100	425
413	433	453	100	595
414	434	454	100	828
413	433	453	100	595
415	435	455	100	1,139
416	436	456	100	1,497
417	437	457	100	1,970
418	438	458	100	3,046
419	439	459	100	3,856
420	440	460	135	162
421	441	461	135	282
422	442	462	135	425
423	443	463	135	595
424	444	464	135	948
425	445	465	135	1,497
426	446	466	135	2,164
427	447	467	135	3,569

5.4.1 FR-EPR measured results

Measured EAB data are plotted in Figure 5.5. It is clear that EAB declines steeply with increasing aging time, ranging from over 200 % for pristine samples to almost zero for those most severely aged. Measured IM data are plotted in Figure 5.6. It is clear that IM increases with increasing aging time. The uncertainty in IM, here a measure of the insulation variability along each sample, also increases with increasing aging time. Measured C and D data are plotted in Figures 5.7 and 5.8, for frequencies 1 kHz and 1 MHz, respectively. Both C and D increase as a function of increasing aging time.

5.4.2 SIR measured results

Measured EAB data for SIR insulation are plotted in Figure 5.9. The mean value of measurements on three nominally-identical samples is reported. EAB declines quickly with increasing aging time, from approximately 320 % for pristine SIR to around 30 % for those samples aged for 3,569 hours. Similar trends have been observed for FR-EPR insulation although EAB for pristine samples in that case was found to be lower than for SIR; between approximately 220 and 270 %, depending on the color.

Measured IM data for SIR insulation are plotted in Figure 5.10. The mean value of measurements on nine nominally-identical samples is reported. IM increases with increasing aging time from approximately 8 N/mm for pristine samples to more than 20 N/mm for the most severely aged samples. In the case of FR-EPR, IM increases from around 16 N/mm for pristine samples to more than 30 N/mm for the most severely aged samples.

Capacitance and dissipation factor data for SIR insulation, measured at frequencies 1 kHz and 1 MHz, are plotted in Figures 5.11 and 5.12, respectively. The mean value of measurements on 10 nominally-identical samples is reported. C and D data obtained for samples 411 through 427 are noticeably smaller in magnitude than those obtained for samples 431 through 467. This behavior did not change after repeating the measurements. C measured on samples 431 through 467 shows a reduction of approximately 0.7 % for severely aged samples compared with pristine samples whereas there is no obvious trend in D as a function of aging time. These

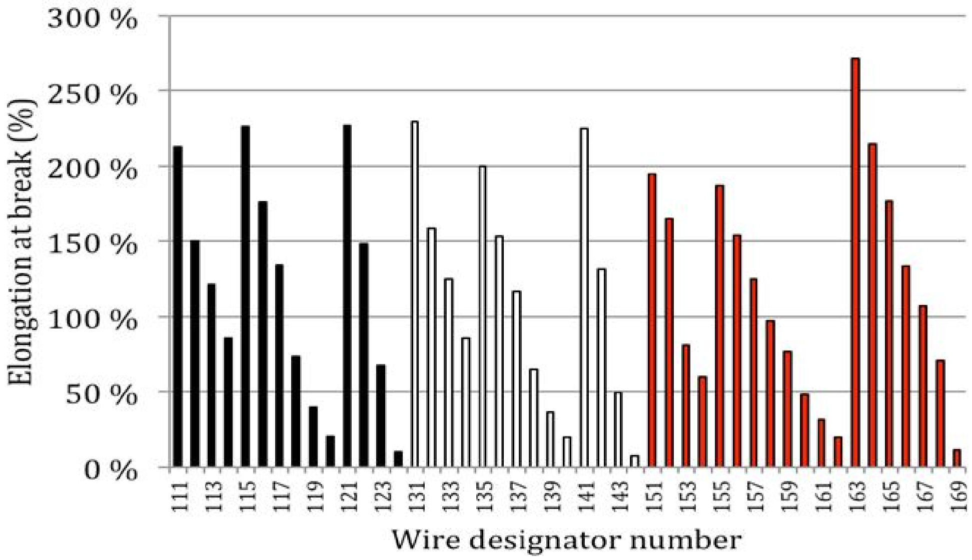

Figure 5.5 Measured elongation-at-break of FR-EPR wire samples listed in Table 5.2. The mean of 3 measurements per aging condition is plotted.

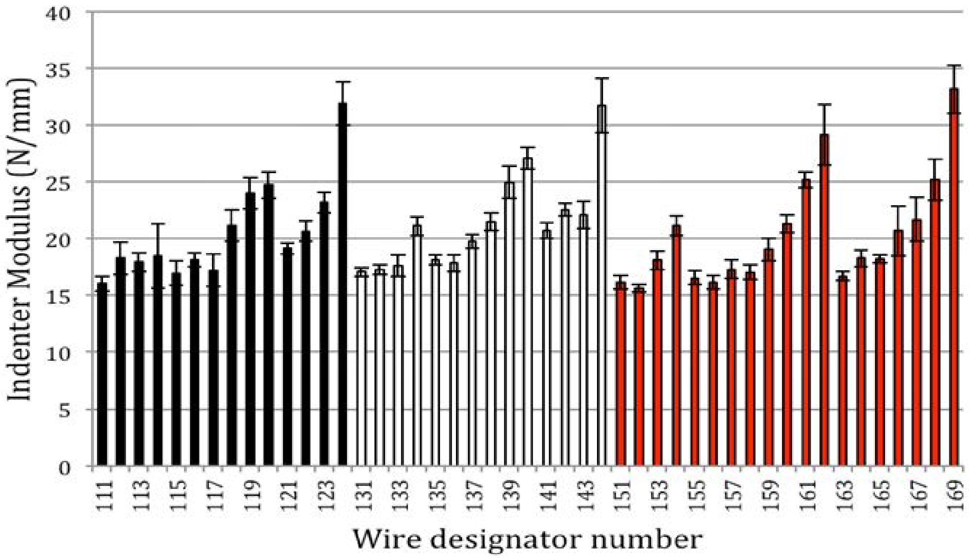

Figure 5.6 Measured indenter modulus of FR-EPR wire samples listed in Table 5.2. The mean and standard deviation of 9 measurements per aging condition is plotted.

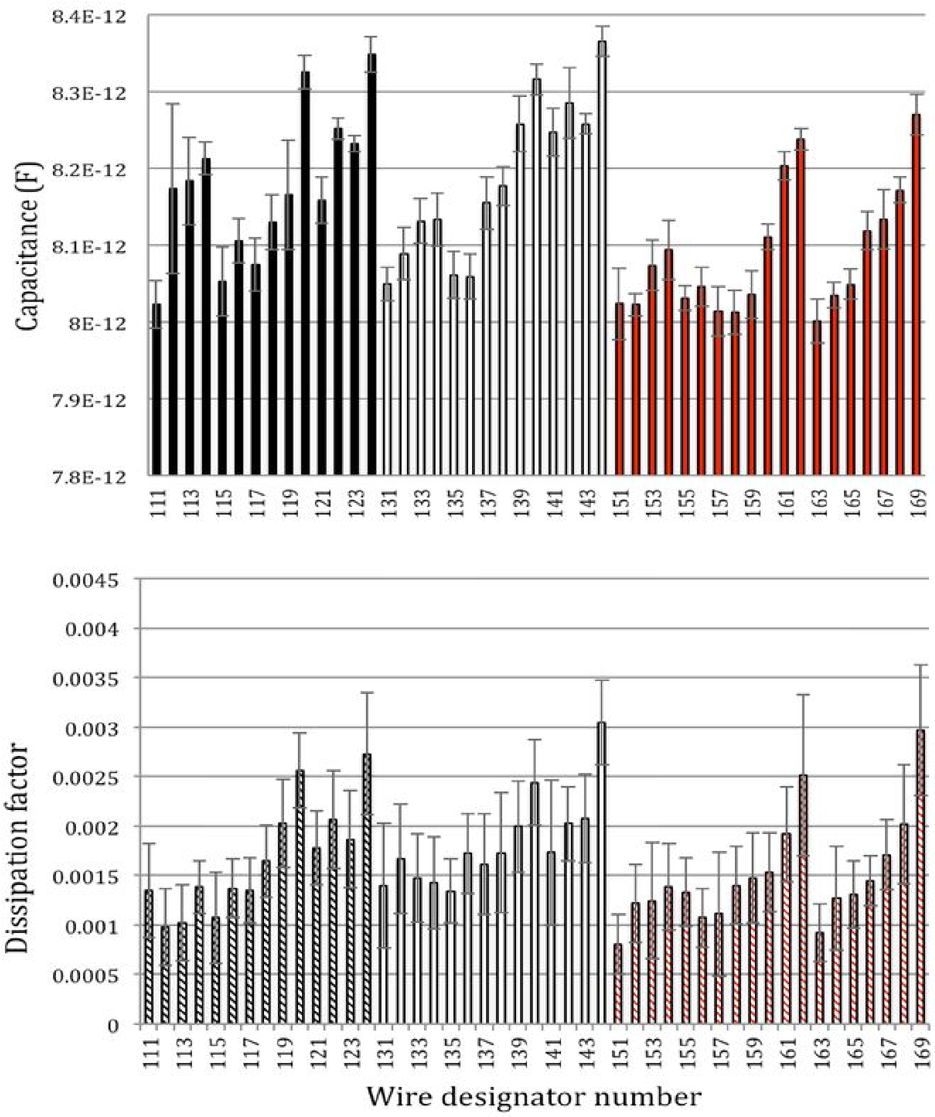

Figure 5.7 Measured capacitance and dissipation factor of FR-EPR wire samples listed in Table 5.2, at 1 kHz. The mean and standard deviation of 10 measurements per aging condition is plotted.

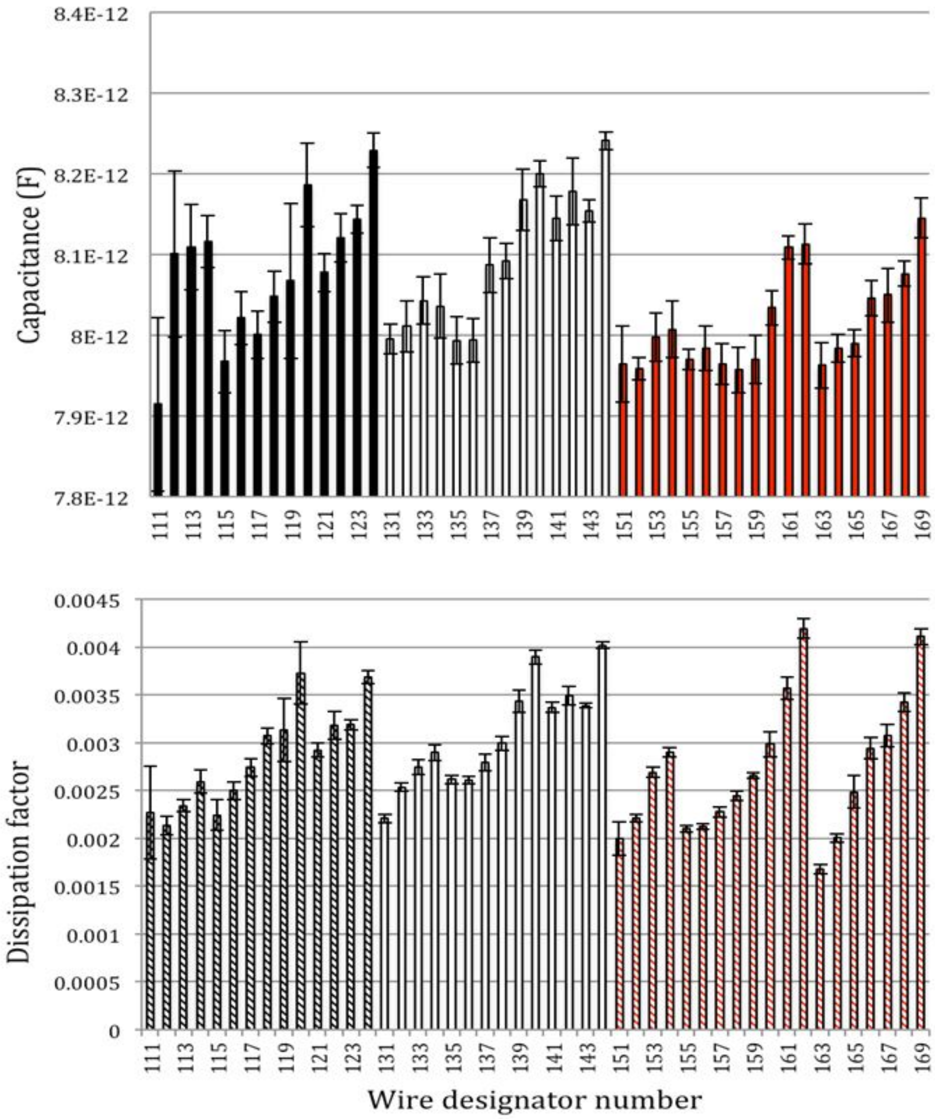

Figure 5.8 Measured capacitance and dissipation factor of FR-EPR wire samples listed in Table 5.2, at 1 MHz. The mean and standard deviation of 10 measurements per aging condition is plotted.

observations are very different than those on aged FR-EPR, in which increases in capacitance and dissipation factor of up to approximately 2.5 % and 150 %, respectively, were observed comparing severely-aged with pristine samples.

5.4.3 Correlation of C and D with EAB and IM

Correlation values between C and D and EAB and IM at 1 kHz and 1 MHz are listed in Table 5.4, where correlation values of 0.85 or greater are highlighted in bold. From Table 5.4 it can be seen that the pattern of stronger correlations between the measured quantities is different for FR-EPR and SIR. In the case of FR-EPR, it can be seen that the higher correlation values are between IM and D, for all sample colors. Additionally, for red insulation, very high (> 0.94) correlation values are obtained between IM and C, and D. For black insulation, correlation values are lower overall, whereas those observed for white insulation fall between those for black and red samples. It is also concluded, therefore, that the colorant added to FR-EPR has a significant impact on the relationship between mechanical and dielectric properties of those samples. This is supported by the fact that most polymers are colored using pigments—dry powders dispersed in the polymer—which are dispersed to achieve different colors using different chemicals. Polymer electrical resistivity is also influenced by the use of different ionic or polar pigments, as well as soluble salts used during manufacturing [17], which has a direct relationship with D.

In the case of SIR the strongest correlation exists between IM and EAB. These results in turn reflect the strength of the response (sensitivity) of the individual indicators to the aging of each polymer. For example, FR-EPR exhibits ∼150 % change in D comparing most strongly aged with pristine samples, whereas there is no obvious trend in D as a function of aging in SIR. Taken together, these results confirm that polymers aged under similar conditions display responses that are particular to the individual polymer. One implication for nondestructive evaluation or monitoring of aging polymers is that the most sensitive indicator of aging whether it be electrical or mechanical is not the same for all polymers.

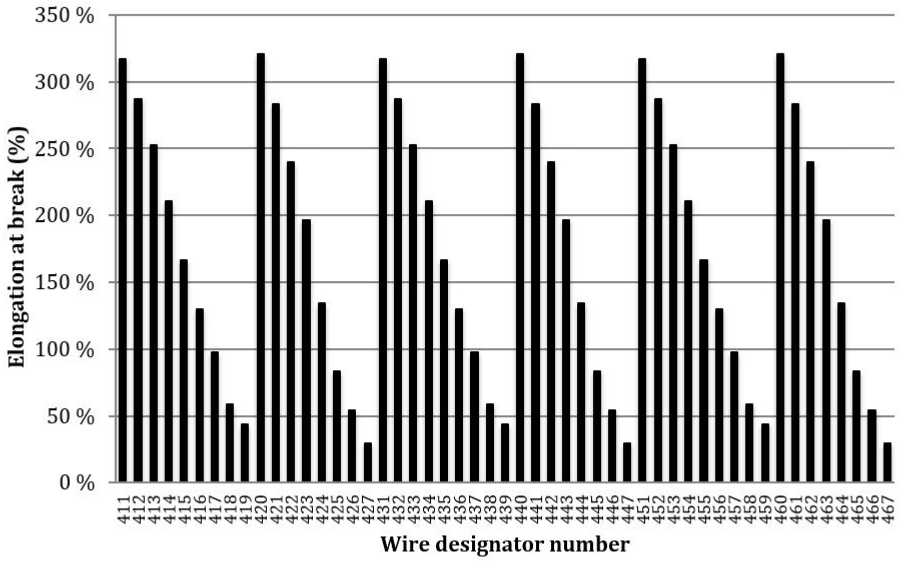

Figure 5.9 Measured elongation-at-break of SIR wire samples listed in Table 5.3. The mean of 3 measurements per aging condition is plotted.

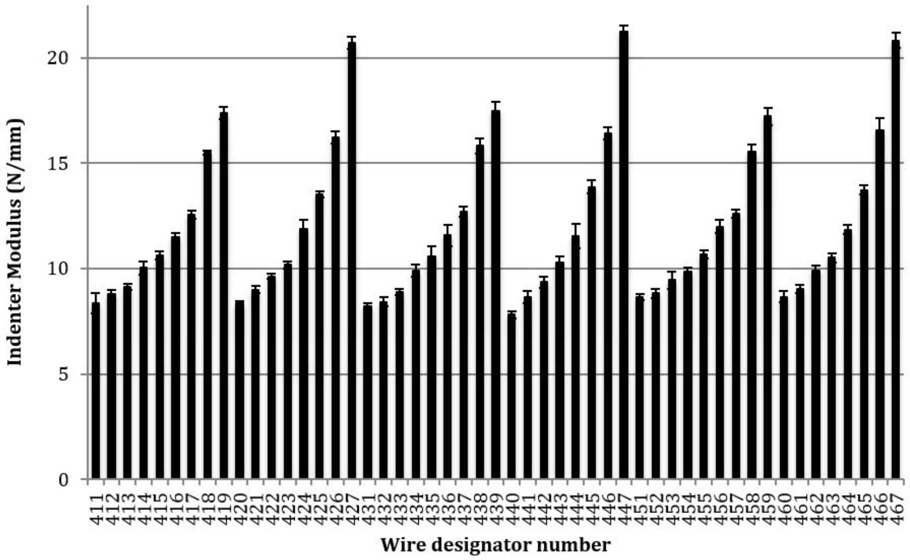

Figure 5.10 Measured indenter modulus of SIR wire samples listed in Table 5.3. The mean and standard deviation of 9 measurements per aging condition is plotted.

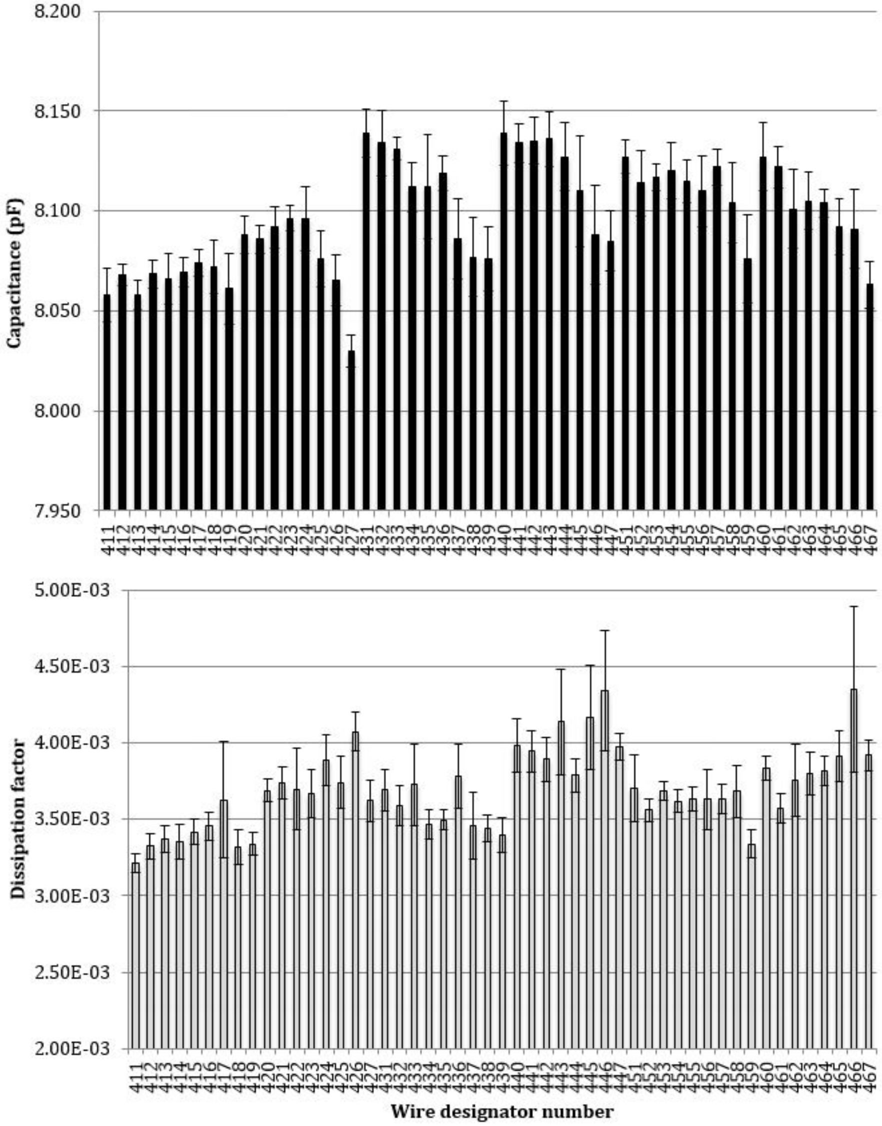

Figure 5.11 Measured capacitance and dissipation factor of SIR wire samples listed in Table 5.3, at 1 kHz. The mean and standard deviation of 10 measurements per aging condition is plotted.

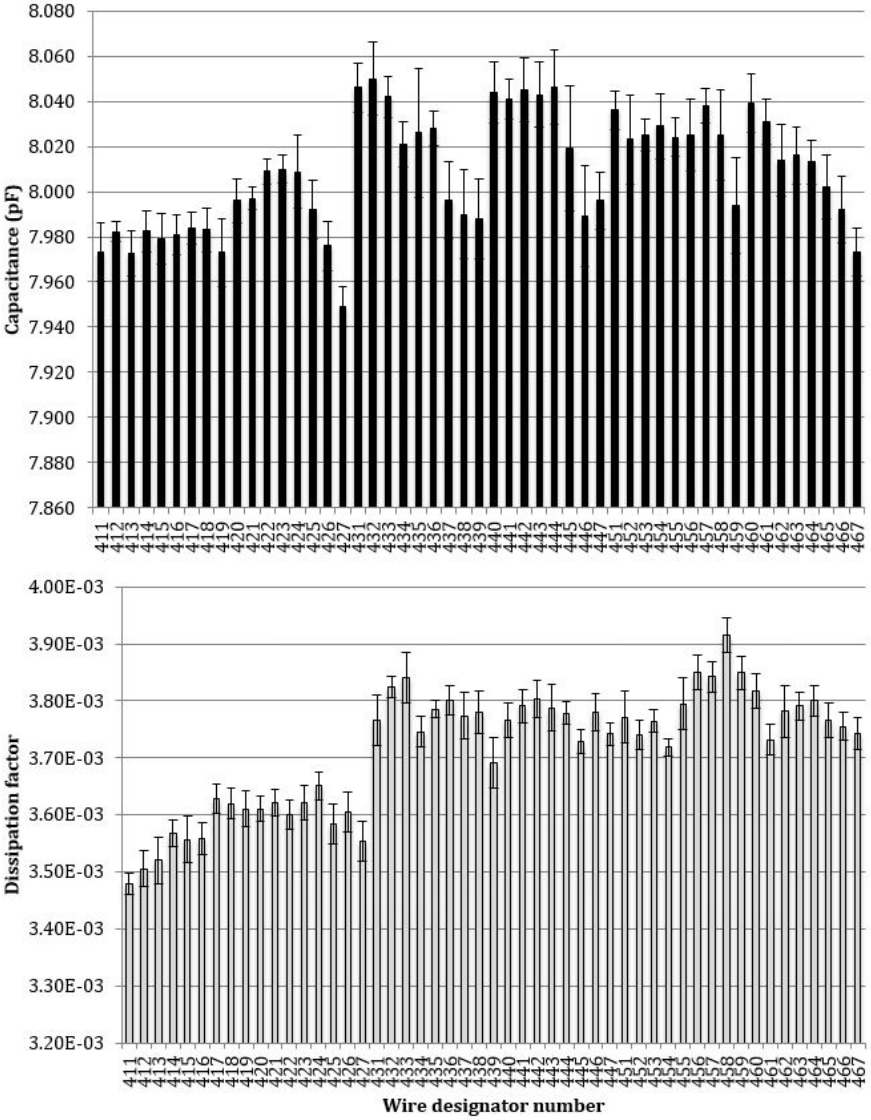

Figure 5.12 Measured capacitance and dissipation factor of SIR wire samples listed in Table 5.3, at 1 MHz. The mean and standard deviation of 10 measurements per aging condition is plotted.

5.5 Conclusion

Correlations evaluated on measurements of elongation-at-break, indenter modulus, capacitance and dissipation factor, taken on aged flame-resistant ethylene-propylene rubber and silicone rubber, are strongest between indenter modulus and dissipation factor for FR-EPR and between indenter modulus and elongation-at-break for SIR. This suggests that the best nondestructive evaluation technique for monitoring aging wire and cable insulation is dependent on the polymer material. In future, therefore, a wider range of polymer insulation materials will be studied in order to inform choice of the best NDE method for monitoring aging of insulation polymers. Further, breakdown voltage will be measured on aged samples in order to evaluate the merit of developing a new acceptance criterion for cable insulation based on breakdown voltage rather than EAB.

5.6 Acknowledgments

The development of the capacitive clamp sensor was supported by The Boeing Company at Iowa State University's Center for Nondestructive Evaluation. Special thanks to Dr. Tianming Chen, for assisting in early development of the cylindrical electrode model that lead to the interdigital design, and to Mr. Rui Ding for preparing the fluid immersion experiment. Irradiated wire samples and elongation-at-break data were provided by the Japan Nuclear Safety (JNES) Organization. The Indenter Polymer Aging Monitor was generously loaned by Analysis and Measurement Services (AMS) Corporation. Special thanks to Ms. Emily Arvia for her time in taking indenter modulus and capacitive data on the FR-EPR wires.

Table 5.4 Magnitude of correlation values between measured elongation-at-break (EAB), indenter modulus (IM), capacitance (C) and dissipation factor (D) at two frequencies. Cross-correlation values with magnitude equal to or greater than 0.85 are written in bold font.

	FR-EPR							
	Black		**White**		**Red**		**Average**	
	EAB	**IM**	**EAB**	**IM**	**EAB**	**IM**	**EAB**	**IM**
IM	0.79	1	0.78	1	0.75	1	0.77	1
C (1 kHz)	0.74	0.81	0.68	**0.90**	0.76	**0.97**	0.64	0.82
C (1 MHz)	0.73	0.77	0.67	**0.89**	0.72	**0.96**	0.62	0.79
D (1 kHz)	0.66	**0.88**	0.71	**0.92**	0.76	**0.96**	0.69	**0.92**
D (1 MHz)	0.73	**0.86**	0.71	**0.92**	**0.88**	**0.94**	0.77	**0.91**
	SIR							
IM	**0.91**	1	**0.92**	1	**0.91**	1	**0.91**	1
C (1 kHz)	0.34	0.54	**0.89**	**0.87**	0.76	**0.89**	0.49	0.56
C (1 MHz)	0.35	0.54	**0.85**	**0.86**	0.69	0.82	0.48	0.56
D (1 kHz)	0.24	0.20	0.00	0.07	0.23	0.29	0.38	0.16
D (1 MHz)	0.39	0.25	0.50	0.57	0.38	0.24	0.32	0.02

5.7 References

[1] C. Desai, K. Brown, M. Desmulliez and A. Sutherland, "Selection of Wavelet for De-noising PD waveforms for Prognostics and Diagnostics of Aircraft Wiring", *2008 Annual Report Conference on Electrical Insulation and Dielectric Phenomena*, Quebec City, Quebec, Canada, 26-29 Oct. 2008, pp. 17-20.

[2] *A Stitch in Time: The Complete Guide to Electrical Insulation Testing*. Dallas: Megger, 2006.

[3] T. Chen and N. Bowler, "Analysis of a capacitve sensor for the evaluation of circular cylinders with a conductive core", *Meas. Sci. Technol.*, Vol. 23, 045102(10pp), 2012.

[4] R. T. Sheldon and N. Bowler, "An Interdigital Capacitive Sensor for Nondestructive Evaluation of Wire Insulation", *IEEE Sensors J.*, Vol. 14, No. 4, pp. 961-970, Apr. 2014.

[5] E. M. Arvia, R. T. Sheldon and N. Bowler, "A Capacitive Test Method for Cable Insulation Degradation Assessment", *2014 Annual Report Conference on Electrical Insulation and Dielectric Phenomena*, Des Moines, Iowa, USA, 19-22 Oct. 2014, pp. 514-517.

[6] N. Bowler, R. T. Sheldon and E. M. Arvia, "A New Test Method for Cable Insulation Degradation Assessment: Capacitive Sensing", *9th International Topical Meeting on Nuclear Plant Instrumentation, Control & Human-Machine Interface Technologies*, Charlotte, North Carolina, USA, 23-26 Feb. 2015, Pages: 8.

[7] T. Chen, N. Bowler and J. R. Bowler, "Analysis of Arc-Electrode Capacitive Sensors for Characterization of Dielectric Cylindrical Rods", *IEEE Trans. Instr. Meas.*, Vol. 61, No. 1, pp. 233-240, 2012.

[8] T. Chen and N. Bowler, "A Rotationally-Invariant Capacitive Probe for Materials Evaluation", *Mater. Eval.*, Vol. 70, No. 2, pp. 161-172, 2012.

[9] R. Ding and N. Bowler, "Influence of Accelerated Aging on Dielectric Properties of Extruded Nylon 6 Film", *2013 Annual Report Conference on Electrical Insulation and Dielectric Phenomena*, Shenzhen, Guangdong, China, 20-23 Oct. 2013, pp. 152-155.

[10] K. L. Simmons et al., "LWRS Program-NDE R&D Roadmap for Determining Remaining Useful Life of Aging Cables in Nuclear Power Plants", PNNL-21731, Sep. 2012.

[11] Y. T. Hsu, K. S. Chang-Liao, T. K. Wang, and C. T. Kuo, "Correlation between mechanical and electrical properties for assessing the degradation of ethylene propylene rubber cables used in nuclear power plants", *Polymer Degradation and Stability*, Vol. 92, pp. 1297-1303, 2007.

[12] N. Bowler, M. R. Kessler, L. Li, P. R. Hondred and T. Chen, "Electromagnetic Nondestructive Evaluation of Wire Insulation and Models of Insulation Material Properties", Report Number: NASA/CR-2012-217330, NF1676L-14135, at: <http://www.sti.nasa.gov/>.

[13] N. Bowler, R. T. Sheldon, R. Ding and N. Goodwill, "Development of Nondestructive Evaluation for Aging Wire Insulation", final report to The Boeing Company, Dec. 2012.

[14] "Test methods for rubber and plastic insulated wires and cables", Japanese Standards Association, JIS C 3005:2000, section 4.16.

[15] T. Yamamoto and T. Minakawa, "Assessment of Cable Aging for Nuclear Power Plants", final report, Japan Nuclear Energy Safety Organization, Report number: JNES-SS-0903, Apr. 2009.

[16] Analysis and Measurement Services Corporation, "Indenter for cable condition monitoring, accessed online 11 Jul. 2014 at: <http://www.ams-corp.com/wp-content/uploads/2012/07/Indenter.pdf>.

[17] M. M. Gerson and J. R. Graff, "Colorants", in *Polymer Modifiers and Additives*, J. T. Lutz and R. F. Grossman, Eds. New York: Marcel Dekker, 2001, pp. 35-93.

CHAPTER 6. GENERAL CONCLUSION

6.1 Discussion

The research presented in this dissertation is motivated by a need for new nondestructive evaluation techniques in both the aerospace and nuclear power industries for the purposes of characterizing important and critical low-conductivity materials, such as outer surfaces of aeronautical structures and wire insulation. Presentation of this research fell into two broad categories: radio frequency sensors and capacitive sensors, with each category further divided into two chapters.

In Chapter 1, a literature survey discussed the many types of RF and capacitive sensors that have been developed for theoretical or practical use. Patch antenna sensors were introduced in Chapter 2, along with a full existing model for calculation of the resonant frequency and quality factor of the sensor due to various low-conductivity materials placed in its near-field sensing region. Each component of the model was discussed in detail, as each has significant influence on the final outputs. In Chapter 3, an input impedance model was discussed in detail that described each contribution from resonant frequency, quality factor and feeding point to the quantity of complex impedance, which can be calculated from the measurable S-parameter outputs of a vector network analyzer. A new method of resonant frequency and Q-factor determination from measured values that focuses on measured impedance rather than S-parameters, as is conventional, was presented. A variety of well-characterized microwave dielectric samples were tested experimentally using a realized patch sensor, designed using the model of Chapter 2 for X-band operation. Excellent agreement with the modeled results for resonant frequency was obtained, while the results for quality factor demonstrate a level of uncertainty that is dependent upon both the model and the measurement method.

Chapter 4 presents a concentric, coplanar interdigital capacitive sensor designed for characterization of glass-fiber polymer-matrix composites. The specific polymer of interest was bismaleimide, which has good mechanical functionality at high temperatures. Glass-fiber bismaleimide-matrix samples were isothermally aged at temperatures around and above the polymer functional limit known in literature and capacitance and dissipation factor measurements were obtained for each sample. Significant changes in the permittivity of the samples with temperature were observed, demonstrating the potential usefulness of such a nondestructive technique to detect degraded regions of critical low-conductivity structures, such as aircraft and pipelines.

Finally, Chapter 5 discussed a cylindrical interdigital capacitive sensor mounted on a handheld spring-loaded clamp for simple and practical measurements on wiring insulation in the field. In the first work presented, aircraft wire samples were immersed in liquid chemicals commonly found in aircraft environments, such as water, jet fuel, and cleaning fluid. Significant changes in measured capacitance of the sensor were observed for wires immersed in polar fluids, while little change was observed for non-polar immersion. The results visually correlate with separate experiments performed using parallel plate capacitors on pure sheets of Nylon 6, the same material as that forming outer layer of the aircraft wires. The last section discusses a set of experiments using the same sensor on a large set of wires irradiated for various durations with ionizing radiation. Measured capacitance and dissipation factor were compared with measured elongation-at-break, an accepted destructive industry testing standard, and indenter modulus, a more recent mechanical nondestructive test. The capacitive sensor results correlated well with indenter modulus for flame-retardant ethylene-propylene rubber-insulated wires, while silicone rubber-insulated wires showed better correlation between indenter modulus and elongation-at-break, indicating that mechanical and electrical testing of wire insulation each have different a different sensitivity to the insulation polymer.

6.2 Recommendations for future research

Numerous paths for design and measurement interpretation improvements are recommended for future work. Regarding the patch antenna sensor, the next step is to develop a robust inversion model that can determine the permittivity and loss tangent of an unknown layer within a multilayer sample, provided that all other layer parameters are known. If no information is known about the layers, then the entire stack can be assumed to be a single effective layer with effective dielectric parameters, which is particularly useful to model the behavior of the entire dielectric stack due to an incident radar pulse, for the calculation of radar cross-section for example. Once a robust inversion model has been developed, the sensor can be scanned over a surface to produce two images: one for relative permittivity and one for loss tangent, either of the single unknown layer or the total effective layer. The single patch antenna sensor may also be expanded to a linear array to eliminate the need to scan in one dimension. This would benefit from reductions in the patch dimensions to improve spatial resolution.

For both the capacitive sensors presented here, an inversion model is also suggested that can provide the actual dielectric properties of an unknown layer or effective layer of either glass-fiber composites or wire insulation. Also, measurements currently require connection to a bulky, heavy and expensive piece of external test equipment via a coaxial cable that alters the measurement if it is moved. A new method of built-in measurement circuit and wireless data transmission is suggested to minimize this uncertainty in actual field measurements.

ACKNOWLEDGMENTS

I would like to express my deepest gratitude to my major professor, Dr. Nicola Bowler, who has been the greatest of mentors for the past five years. Her guidance, support, confidence in my work, attention to detail, and kindness have made a better and more confident student, teacher, speaker, writer, researcher and engineer. I am truly honored to have completed both my master's and doctorate degrees under her tutelage and I look forward to the future thanks to the strong foundation she helped set.

I must also give my deep thanks to Dr. Peter Schubert, who encouraged me to pursue my doctorate many years ago. I would not be here if it were not his encouragement and confidence that I could succeed. My humble thanks goes to all my helpful colleagues and officemates here at Iowa State University, past and present, who have become my good friends over the years: Dr. Tianming Chen, Dr. Yang Li, Dr. Hui Xie, Dr. Chih-Wei Chen, Dr. Connor Daily, Dr. Weixing Sun, Yuan Ji, Xiaohan Kang, Rui Ding, Shuaishuai Liu, Amin Gorji-Bandpy, Jafar Al-Kofahi, and many more.

Last but not least, I would like to thank my family. To my grandparents Robert and Lois Sheldon, and Thomas and Beverly Skoniecke, I will forever be grateful for the memories we have shared together and for the wisdom they have imparted to me. To my parents, Kevin and Victoria, and sister Laura, I am extremely thankful for their love and support throughout my time at graduate school.

I look forward to the next chapter!